Distribution Agreement

In presenting this dissertation as a partial fulfillment of the requirements for an advanced degree from Emory University, I hereby grant to Emory University and its agents the non-exclusive license to archive, make accessible, and display my dissertation in whole or in part in all forms of media, now or hereafter known, including display on the world wide web. I understand that I may select some access restrictions as part of the online submission of this dissertation. I retain all ownership rights to the copyright of the dissertation. I also retain the right to use in future works (such as articles or books) all or part of this dissertation.

Signature:

_____ _____

Benjamen Nforneh Date

Toward Connecting Solvent and Surface Dynamics to Protein Function: An EPR Approach

by

Benjamen Nforneh
Doctor of Philosophy
Physics

Kurt Warncke, Ph.D
Advisor

Connie Roth, Ph.D.
Committee Member

Daniel Weissman, Ph.D.
Committee Member

Emily Weinert, Ph.D.
Committee Member

Laura Finzi, Ph.D.
Committee Member

Accepted:

Lisa A. Tedesco, Ph.D.
Dean of the James T. Laney School of Graduate Studies

Date

Toward Connecting Solvent and Surface Dynamics to Protein Function: An EPR Approach

by
Benjamen Nforneh
M.S., African University of Science and Technology, Abuja, Nigeria 2013
B.S., University of Buea, Cameroon, 2010

Advisor: Kurt Warncke, Ph.D.

An abstract of
A dissertation submitted to the Faculty of the
James T. Laney School Of Graduate Studies of Emory University
in partial fulfillment of the requirements for the degree of
Doctor of Philosophy
in Physics

June 2018

Abstract

Toward Connecting Solvent and Surface Dynamics to Protein Function: An EPR Approach

by Benjamen Nforneh

The B_{12} (adenosylcobalamin)-dependent ethanolamine ammonia-lyase (EAL) is a product of the ethanolamine utilisation (eut) gene cluster, that is involved in human gut microbiome homeostasis and in disease conditions caused by pathogenic strains of $Salmonella$ and $Escherichia\ coli$. Electron paramagnetic resonance (EPR) spectroscopy of the spin probe, TEMPOL, is used to resolve two distinct concentric solvent phases around EAL: protein-associated domain (PAD) and mesodomain. By using a continuum model, we estimate the solvent shell thicknesses around EAL (mesodomain $\approx$ 10-40 Å and PAD $\approx$ 6 Å) and propose a model for the system. Systematic tuning of solvent dynamics and glass transitions by using dimethylsulfoxide (DMSO) variation in the low-T mesodomain system reveals features of the mesodomain/PAD and PAD/protein surface coupling that inform the understanding of solvent and coupled protein dynamics to chemical catalysis in EAL. Toward understanding the function of the EutC N-terminal, signal sequence associated domain of wild type EAL, and the interplay between protein stability and the EAL targeting and trafficking to the Eut biomicrocompartment (BMC), spin label 4-maleimido-TEMPO (4MT) attached at the C37 of EutC and EPR spectroscopy is used. A two-state model is propose based on a single 4MT labelling site, in which fast and slow motional populations represent EAL-bound and free conformations of the EutC N-terminal domain. We propose that the two states present a balance between EutC function and EAL protein stability and efficient targeting to the BMC. The observed fluidizing effect of the added % v/v DMSO on the dynamics in the mesodomain, and the coupled increase in PAD dynamics, is manifested in the lowering of the fluid-solid transitions in each phase. This provides a method to precisely control the solvent and surface dynamics around EAL as a tunable parameter in quantifying and investigating the mechanism of coupling between solvent and surface dynamics, and chemical reaction steps in EAL.

Toward Connecting Solvent and Surface Dynamics to Protein Function: An EPR Approach

by:
Benjamen Nforneh
M.S., African University of Science and Technology, Abuja, Nigeria 2013
B.S., University of Buea, Cameroon, 2010

Advisor: Kurt Warncke, Ph.D.

A dissertation submitted to the Faculty of the
James T. Laney School of Graduate Studies of Emory University
in partial fulfillment of the requirements for the degree of
Doctor of Philosophy
in Physics

June 2018

Acknowledgments

I would like to thank my advisor Dr. Kurt Warncke for his guidance and support during my graduate study at Emory. He was always open to my ideas and provided insightful criticisms and constant support which led to the work presented herein. His guidance helped me to develop scientific and research skills, which are germane to my future career. I am also greatful to my committee members, Dr. Laura Finzi, Dr. Connie Roth, Dr. Daniel Weissman, and Dr. Emily Weinert for their thoughtful criticisms and time during the course of my PhD research. I also owe thanks to all the Warncke lab members for useful discussions and time spent on/off the lab.

I am indebted to my father, Victor and my mother, Christina, God bless their souls, for making me the man that I am today. Your unconditional love and support paved the way for my success today. Of course, I also owe gratitude to the rest of the Ndankwa's family and Larodia for standing by me even in tough times.

To all the friends I made enroute to my PhD, both home and here, I would like to say a big thank you for the time spent together and for being a part of my life.

Contents

List of Figures

List of Tables

Abbreviations

EAL : **E**thanolamine **A**mmonia-lyase
DMSO : **D**imethylsulfoxide
TEMPOL : **4**-hydroxy-TEMPO (Spin probe)
4MT : **4**-maleimido-TEMPO
EPR : **E**lectron **P**aramagnetic **R**esonance
ATP : **A**denosine **T**riphosphate
h: **P**lanck's Constant
ν: **f**requency
PSD : **P**hase **S**ensitive **D**etection
PAD : **P**rotein **A**ssociated **D**omain
MFC : **M**aximum **F**reeze **C**oncentration
BMC : **B**iomicocompactment
DNA : **D**eoxyribonucleic **A**cid
Eut : **E**thanolamine **ut**tilization
wt : **w**ild **t**ype
Cys : **C**ystein
RSA : **R**elative **S**olvent **A**ccessibility
PCR : **P**olymerase **C**hain **R**eaction
SDSL : **S**ite-directed **s**pin-labeling
AmEtoH : **Am**inoethanol
τ_c : **c**orrelation **t**ime, $\tau_{c,f}$: **F**ast component **c**orrelation **t**ime, $\tau_{c,s}$: **S**low component **c**orrelation **t**ime
W : Normalized **W**eight, W_f: Normalized **F**ast component of **W**eight, W_s : Normalized **S**low component of **W**eight

Chapter 1

Introduction and Background, Technique, and Overview

1.1 INTRODUCTION AND BACKGROUND

The B_{12} (adenosylcobalamin; AdoCbl)-dependent ethanolamine ammonia-lyase (EAL; EC 4.3.1.7), [3] is a bacterial enzyme that is involved in gut microbiome homeostasis, [4–6] and in disease conditions caused by pathogenic strains of $Salmonella$ and $Escherichia\ coli$, in humans. [7, 8] The EAL oligomer is composed of the $EutB$ (49.4 kDa, $S.\ typhimurium$; α-subunit) and EutC (32.0 kDa, $S.\ typhimurium$; β-subunit) proteins (one active site per $EutBEutC$) in a $[(EutBEutC)_2]_3$ stoichiometry. [1, 9–12] Figure 1.1 shows the X-ray structure of EAL from protein data bank (PDB) entry 3ABO. [1] It is characterized by eight β-strands surrounded by eight α-helices connected by loops. The C-terminal end of the barrel contains the ethanolamine binding site. There is a 5'-deoxyadenosine binding pocket in the EutB subunit providing orientation for cofactor binding. [11] The EutC subunit covers the AdoCbl and the C-terminal end of the barrel of the EutB subunit in the complete enzyme. Together with AdoCbl, the EAL enzyme promotes the radical rearrangement which is initiated by the cleavage of the cobalt-carbon bond of the coenzyme. [13] Of significant importance is the 10^{12} rate increase achieved upon hemolytic cleavage of the cobalt-carbon bond at the center of the AdoCbl upon substrate binding when compared to the free cofactor in solution. [13–17] This enzyme reaction chemistry has been studied extensively for over five decades, most especially, in the $S.\ typhimurium$, and related enzyme systems. [18–21]

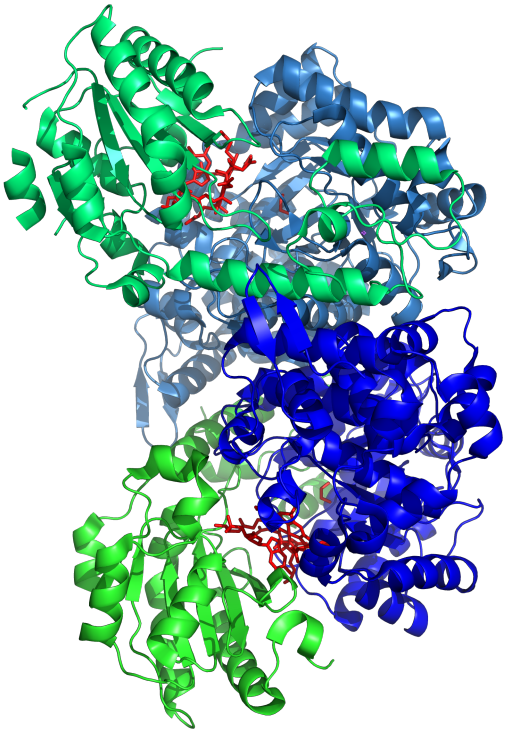

Figure 1.1: X-ray crystal structure of the *E. coli* EAL $(\alpha\beta)_2$ dimer. PyMol representation of EAL $(\alpha\beta)_2$ dimer (EAL from PDB entry 3ABO [1]) shown with EutB subunits in blue and skyblue cartoon representation, EutC subunits in green and lime green cartoon representation, cyanocobalamin and ethanolamine in red sticks representation

The extensive work on this B_{12} dependent enzyme, and other B_{12} dependent enzymes, is motivated by the 10^{12} rate enhancement and the desire to understand such chemistry. The hope is that understanding the chemistry and biology of the system will lead to the creation of novel protein-catalyst systems. [22, 23] In ad-

dition, the EAL is thought to function under pathogenic conditions with other proteins of the ethanolamine utilization pathway (products of the eut operon), in the Eut biomicrocompartment (BMC), a sub-cellular organelle. [24, 25] Elucidation of the molecular basis of EAL catalysis, and the intracellular trafficking and targeting of EAL to the BMC, is a direction for development of therapeutics. Furthermore, the EAL together with AdoCbl catalyzes the conversion of the substrate ethanolamine (also called 2-aminoethanol or monoethanolamine) to acetaldehyde and ammonia. Both mammalian and cell membranes are rich in phosphatidylethanolamine, which is readily broken down by phosphodiesterases to give ethanolamine. [6, 26] Thus, cell membrane composition and diet make the intestine an ethanolamine rich environment. The ability to use ethanolamine as the sole source of energy (carbon and nitrogen) confers an advantage for bacterial colonization of the gut. Several pathogenic bacteria, including $Salmonella$, use the ability to metabolize ethanolamine to survive in ethanolamine rich environments such as in foods, and within their hosts. [4–8,27–31] As a result of this, a strong correlation has been found between food poisoning bacteria and the presence of eut genes. [32] A holistic understanding the of eut pathway can lead to drug development that suppress such bacterial proliferation.

Protein function has always been associated with its 3-dimensional structure which is determined by its primary sequence [33] and studies have shown that dynamics plays a huge role in protein function. [34–38] Even with intrinsically disordered proteins (IDP) [39–43], the role of dynamics is closely related to their function. Frauenfelder and many others [44–55], have looked at the effect the sol-

vent environment and surface fluctuations around a protein has on its function. In line with using the information gained from such studies to engineer synthetic catalysts and potential targets for therapeutics (by using the protein configurations and configurational fluctuations), understanding the role of the solvent and surface fluctuations on enzyme functions become vital in designing effective enzyme systems.

1.1.1 Structure of B_{12} coenzyme adenosylcobalamin (AdoCbl)

The enzymes that use B_{12} as a cofactor fall into three broad categories namely the $isomerases$, the $methyltransferases$, and the reductive $dehalogenases$. [56] The EAL belong to the $isomerases$ class. $Isomerases$ catalyze 1,2 rearrangement reactions. [56] In such reactions, a hydrogen on one carbon is exchanged with a substituent (for EAL, the substituent is an amine) on the adjacent carbon. The second step after the rearrangement is the release of the product ammonia. It is from here that EAL draws its name, deaminase as commonly used in the old literature. [18–21] The $isomerases$ are found in bacteria, with the exception of methylmalonyl-CoA mutase which is present in mammals. [56–60] The only other B_{12}-dependent enzyme in humans is methionine synthase, a $methyltransferase$ that requires methylcobalamin. [60, 61]

Figure 1.2 shows the structure of AdoCbl. The AdoCbl precursor is derived from the same porphyrin precursor as heme and chlorophyll. It is however the

most complex structure of any biological cofactor. It requires more than 20 genes for its biosynthesis and it cannot be synthesized by humans. [62] The B_{12} is found in both archaebacteria and eubacteria, as well as in eukaryotes. Both methylcobalamin and AdoCbl play essential roles in the metabolism of higher eukaryotes. [63] The B_{12} is essential for humans and the lack of it in the diet, or an inability to absorb it, is the cause of pernicious anaemia. Only plants do not appear to use B_{12}.

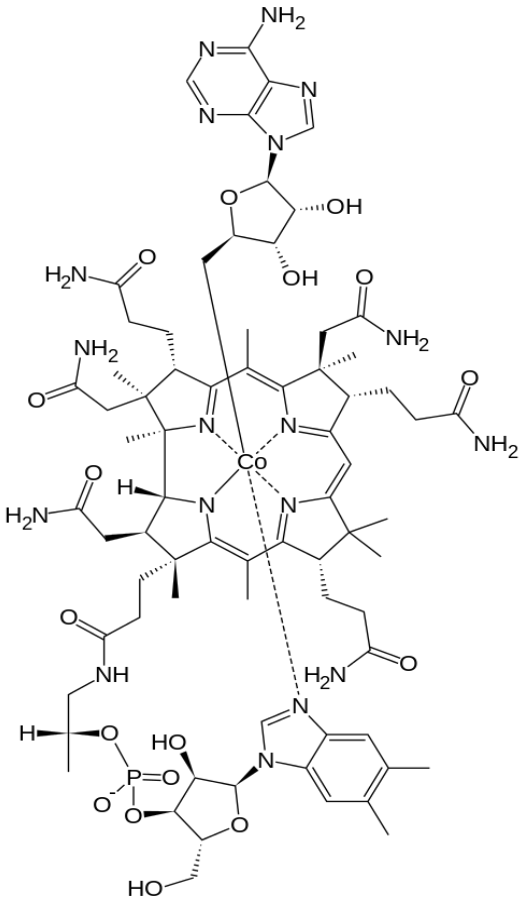

Figure 1.2: Structure of adenosylcobalamin.

Figure 1.2 can be divided into three planes; the central plane and the plane above and below the central plane. At the heart of the coenzyme (the central plane) is the cobalt atom that is surrounded by the heterocyclic ring called a corrin. The corrin ring is smaller than a porphyrin ring of heme compounds due to the loss of one carbon that is used to link two of the pyrrole rings in its structure. It is believed that this is an adaptation for binding cobalt which has a smaller atomic radius than iron, the metal bound by heme. [56] The cobalt is held in place by four corrin nitrogens in the equatorial plane. There is a heterocyclic base that coordinates the cobalt from below the corrin ring referred to as the tail. This base is always a 5,6-dimethylbenzimidazole group in animals and for bacteria, a variety of bases are available. In the plane above the corrin ring, the 5'-deoxyadenosyl group from adenosine triphosphate (ATP) binds axially to the cobalt. This forms a very weak covalent bond between the cobalt and carbon having a dissociation energy of about 30 kcal/mol. [13] This relatively low cobalt-carbon bond dissociation energy is exploited to catalyze a variety of chemical reactions. It is important to note that the upper axial ligand can be substituted from the 5'-deoxyadenosyl group in AdoCbl to create different forms of B_{12}. [3]

1.1.2 The ethanolamine ammonia-lyase enzyme: Reaction and mechanism of action

The EAL was identified in bacterial extracts by Clive Bradbeer over 5 decades ago. [20,21] The enzyme has two substrates, ethanolamine and 2-aminopropanol

[64], and requires a cofactor AdoCbl to catalyze the deamination of ethanolamine into two products; acetaldehyde and ammonia. The acetaldehyde is further metabolized within the cell to acetate and ethanol. [65, 66] The formation of acetate from intermediary acetyl phosphate is coupled to the phosphorylation of ATP. Figure 1.3 shows a schematic depiction of the native reaction catalyzed by EAL. The EAL catalyzes the exchange of the amine group on the second carbon with a hydrogen atom on the adjacent carbon. The substrate then rearranges to release ammonia, and form the corresponding aldehyde. The minimal mechanism of EAL catalysis is shown in Figure 1.4.

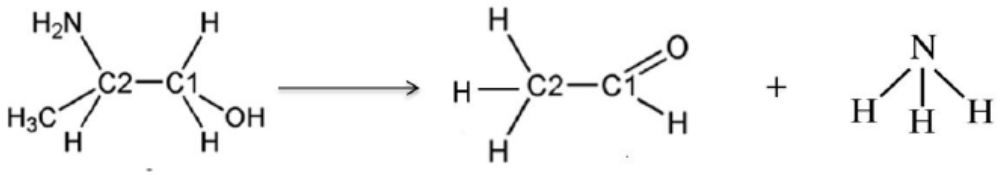

Figure 1.3: The native reaction catalyzed by EAL

The mechanism of the EAL catalyzed reaction proceeds as follows. Upon substrate binding, the weak covalent cobalt-carbon bond at the center of the AdoCbl (Fig: 1.2) is broken homolytically, yielding a singlet born 5'-deoxyadenosyl group and a low spin $(S = 1/2)$ cob(II)alamin, Cbl(II), radical pair. The deoxyadenosyl radical migrates to the substrate where it abstracts a hydrogen from the C1 carbon of the substrate (HT1), in order to complete the radical pair separation process and forming a Co(II)-substrate radical pair. [38, 67–69] This is followed

by a radical rearrangement step whereby the substrate radical migrates to the adjacent carbon (C2) with the concomitant migration of the amine to C1 to form the product radical species. [70, 71] This step is followed by the quenching of the product radical by a second hydrogen atom transfer (HT2) process from the 5'-deoxyadenosine, to form diamagnetic products in parallel with reformation of the intact cofactor, and the released of the acetaldehyde and ammonia. The change in substrate over the steps of the mechanism is shown in Figure 1.5 .

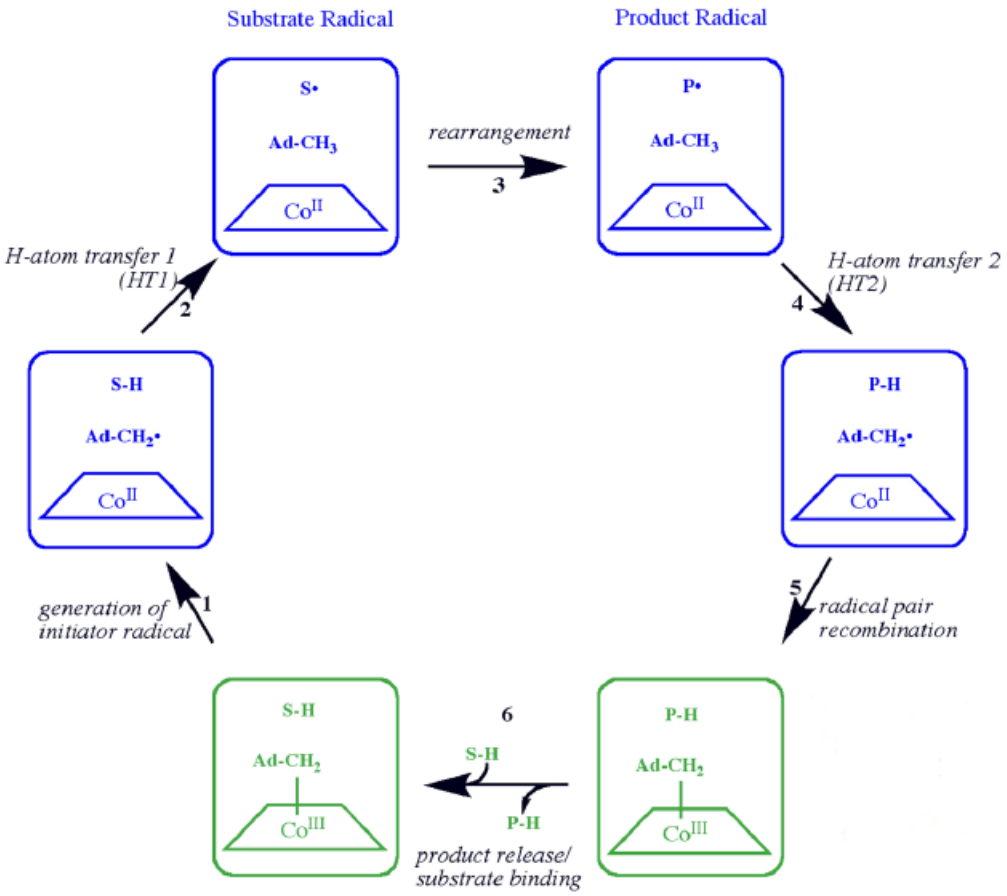

Figure 1.4: The minimal mechanism of the B_{12}-dependent EAL catalysis. The steps correspond to: (1) Substrate binds to the holoenzyme and cause a hemolytic cleavage of the cobalt-carbon which results in radical pair separation. (2) The 5′-deoxyadenosyl radical migrate to the substrate and abstracts hydrogen atom to form the substrate radicals in a first hydrogen atom transfer step. (3) The amine group migrate from the C1 to the C2, with a concomitant migration of substrate from C1 to C2, to create the product radical. This is the radical rearrangement step. (4) Hydrogen is abstracted from the 5′-deoxyadenosine forming a diamagnetic product and recreating the 5′-deoxyadenosyl radical. This is the second hydrogen atom transfer step. (5) The 5′-deoxyadenosyl radical migrates back to the $Co(II)$ and the radical pair recombines.

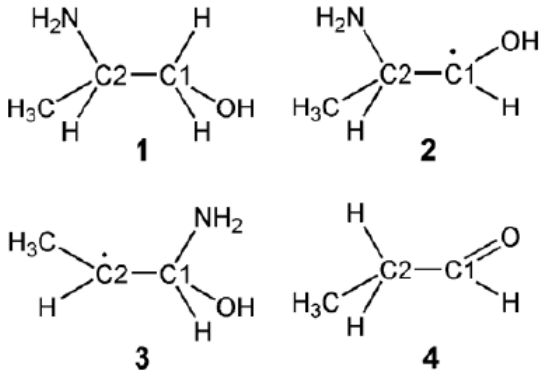

Figure 1.5: The change in substrate over the steps of the mechanism in Fig: 1.4 .

1.1.3 The ethanolamine utilization bacterial microcompactment and the role of ethanolamine ammonia-lyase

Eukaryotic organisms are species with well characterized organelles ranging from the nucleus to membrane-bound organelles such as the chloroplasts. In some prokaryotes, there exist polyhedral organelles that have a shell of protein, and that contain a collection of enzymes associated with a specific metabolic process. These polyhedral organelles are generally referred to as metabolosomes, or bacterial microcompartments (BMCs). [25,72–84] BMCs vary in size with most having a diameter in the range 100-200 nm. The advantage of BMCs is that by encapsulating enzymes and pathway intermediates within a selectively permeable shell, they may increase reaction rates, retain volatile intermediates, protect the cytoplasm from toxic intermediates, and enable recycling of enzyme cofactors. [25,72–75,77–79,81–84]

The BMCs have been the subject of research in recent years due to their enormous potential in drug design and engineering. [85] BMCs have potential applications in therapeutics where they can be used as drug delivery vehicles. Bacteria such as $cyanobacteria$, $S.\ enterica$, and $E.\ coli$ are capable of synthesizing a few types of BMCs with each differing by the key enzyme it encapsulates. However, of all the possible BMCs up to date, the most studied is the carboxysome which is a polyhedral bacterial microcompartment that enhances carbon fixation by encapsulating the two enzymes ribulose-1,5 bisphosphate carboxylase-oxygenase ($RuBisCo$) and carbonic anhydrase. [24, 86] $S.\ enterica$ and $E.\ coli$ have the ability to make related carboxysome-like structures but with different metabolic activities. These are the microcompartments associated with ethanolamine utilization (Eut) and 1,2-propanediol utilization (Pdu). Both of these metabolic activities depend on enzymes that require AdoCbl as a coenzyme. Organelles involved in coenzyme B_{12}-dependent ethanolamine degradation have as key function to metabolize ethanolamine without allowing the release of acetaldehyde into the cytosol. This alleviates the potentially toxic effects of excess aldehyde in the bacterial cytosol and also prevent volatile acetaldehyde from diffusing across the cell membrane and leading to a loss of carbon. [87]

The Eut operon is composed of 17 genes. [87, 88] In $Salmonella$ and $E.\ coli$, the 17-gene operon of the Eut metabolosome codes for five homologous BMC proteins (EutM, EutS, EutK, EutL and EutN) that form the BMC wall and are necessary to synthesize the Eut BMC. [89] Since EAL is thought to function under pathogenic conditions with other proteins of the Eut pathway in the Eut BMC,

[24, 25] elucidation of the molecular basis of EAL catalysis, and the intracellular trafficking and targeting of EAL to the biomicrocompartment, is a direction for development of therapeutics.

1.2 EXPERIMENTAL TECHNIQUE

1.2.1 Electron paramagnetic resonance spectroscopy

Electron Paramagnetic Resonance (EPR) is resonance absorption of electromagnetic radiation by a paramagnet species. [90] The phenomenon of EPR was discovered in the 1945 when former Soviet Union physicist Yevgeny Zavoisky published a report in a Soviet physics journal on the first successful observation of EPR absorption. [91] The frequency of the electromagnetic waves utilized was around 100 MHz and the resonance magnetic field was about 4.76 T. [91] This frequency is much lower than those that are being used today, see Table 1.1. Over the period from 1945 to 1955, the academic discipline of EPR was established. The EPR technique is a probe for unpaired electrons that provides a way to investigate and characterize the physical, microstructures, and kinetics of biological systems and materials. [40, 68, 92–107] The central equation of EPR is given in equation 1.2.1.

$$h\nu = g\beta H \tag{1.2.1}$$

where h is Planck's constant, ν is the frequency of electromagnetic radiation, β is the Bohr magneton, and H is the external magnetic field. g is the g-value, and

for a free electron, it is equal to 2.0023. [90] For a spin $S = 1/2$ system with no nuclear spin, the electron spins can align themselves parallel or anti-parallel to an external magnetic field corresponding to low and high energy states, respectively, and the Hamiltonian $\widehat{H}$ for the system can be written as;

$$\widehat{H} = g_e \beta H \widehat{S}_z \tag{1.2.2}$$

Where $\widehat{S}_z$ is the spin operator. Equation 1.2.2 represents the electron Zeeman interaction. The eigenvalues m_s of $\widehat{S}_z$ are $\pm\frac{1}{2}$. The energy **E** of the two possible spin states is given by;

$$\begin{aligned} E_{+\frac{1}{2}} &= < +\frac{1}{2} \mid g_e \beta H \widehat{S}_z \mid +\frac{1}{2} > \\ &= +\frac{1}{2} g_e \beta H \end{aligned} \tag{1.2.3a}$$

$$\begin{aligned} E_{m-\frac{1}{2}} &= < -\frac{1}{2} \mid g_e \beta H \widehat{S}_z \mid -\frac{1}{2} > \\ &= -\frac{1}{2} g_e \beta H \end{aligned} \tag{1.2.3b}$$

Transitions between the Zeeman energy levels can occur if an appropriate electromagnetic field with the frequency ν having energy $h\nu$ matches the energy separation $\triangle E$ of the two states. In such a scenario, resonance occurs and the resonance condition is; $\triangle E = h\nu = g_e \beta H$

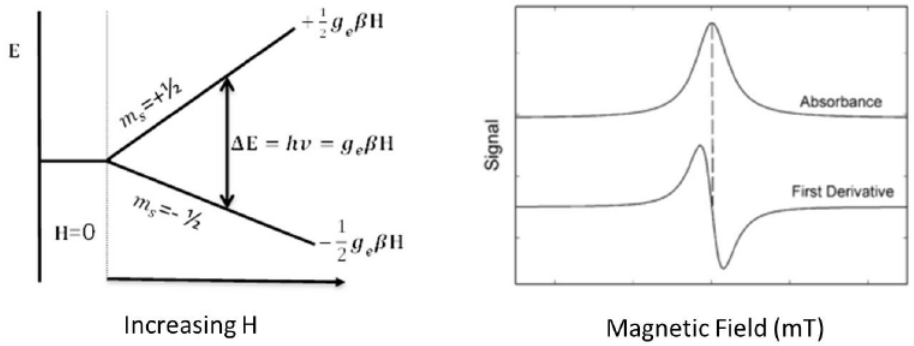

Figure 1.6: Energy level diagram (left) and EPR spectra presentations (right).

Table 1.1: Resonance Fields for a g=2 radical at various microwave frequencies.*

Microwave band	**Frequency (GHz)**	**H_{reso} (G)**
L	1.0	357
S	2.0	715
X	9.0	3360
K	24.0	8577
Q	34.0	12151
W	94.0	33595

* For β =9.27E-24J/T, h=6.626E-34J/s and using equation 1.2.1

Figure 1.6 shows the energy level diagram for the system and the EPR signal recorded.

Nitroxides are stable radicals, that have been used to address the T-dependence of solvent mobility, including phase transitions and glass formation in aqueous

phases as well as in determining structures, conformational changes and distances measurements. [40, 98–102, 107–113]

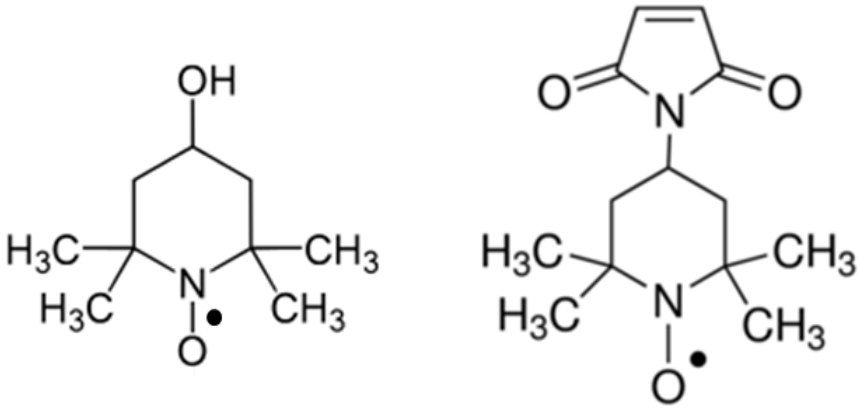

Figure 1.7: Structure of spin probe TEMPOL (left) and the spin label 4-maleimido TEMPO (right).

Here we used 4-hydroxyl TEMPO (TEMPOL; Figure 1.7) and 4-maleimido TEMPO (4MT; Figure 1.7) each with an unpaired electron $(S = \frac{1}{2})$ on the oxygen $(I = 0)$ that is shared with the adjacent nitrogen $(I = 1)$. The electron possesses some spin density in the s-orbital, which has a nonzero probability density at the nucleus and thus interacts with the nuclear spin of the nitrogen. The nuclei spin has multiplicity of $2(I) + 1 \rightarrow 2(1) + 1 = 3$. In a system like this, the interaction of the electron and nuclear dipole shown in, Figure 1.8, results in a hyperfine coupling. The Hamiltonian for the system is given in equation 1.2.4.

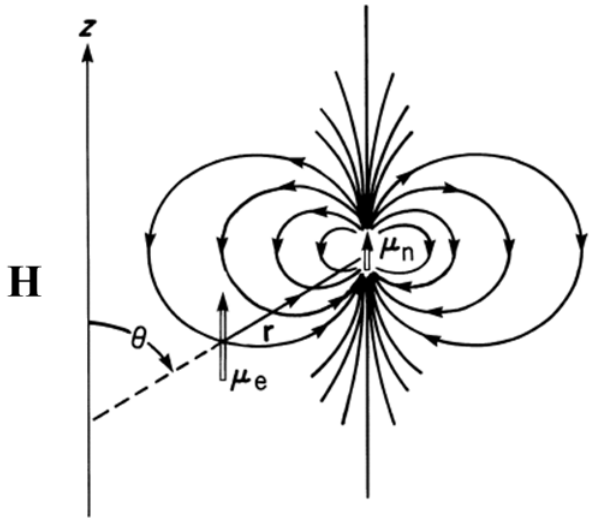

Figure 1.8: Schematic showing interaction of the electron and nuclei dipole. θ is the angle between the vector **r** and the applied field [90]

$$\widehat{H} = g_e \beta H \widehat{S}_z + g_n \beta H \widehat{I}_z + hA\widehat{S}_z\widehat{I}_z \tag{1.2.4}$$

Where the first two terms are the electron and nuclear Zeeman interactions, respectively, and the third is the hyperfine interaction arising from the interaction of the electron and nuclear dipoles. A is the hyperfine coupling constant. The A can depend on the orientation between the vector **r** and the magnetic field vector **H** (Figure 1.8), in which case it is called anisotropic hyperfine coupling, A_{dip}. When it does not depend on orientation it is called isotropic hyperfine coupling, A_o. For an isotropic system, $A_o = \frac{A_x + A_y + A_z}{3}$ and for an anisotropic system,A_{dip} is giving in equation 1.2.5. [90]

$$A_{dip} = \frac{g_e g_n \beta_s \beta_n}{r^3}[(3cos^2\theta - 1)]m_s m_I \tag{1.2.5}$$

Considering the isotropic case, omitting the nuclear Zeeman term in Eq. 1.2.4 as it does not affect the transition energies, the energy eigenvalues for the system are given by;

$$\begin{aligned}
E_{+\frac{1}{2},1} &=< \frac{1}{2}, 1 \mid g_e\beta H\widehat{S}_z + hA_o\widehat{S}_z\widehat{I}_z \mid \frac{1}{2}, 1 > \\
&= \frac{1}{2}g_e\beta H + \frac{hA_o}{2} && \text{(1.2.6a)} \\
E_{+\frac{1}{2},0} &=< \frac{1}{2}, 0 \mid g_e\beta H\widehat{S}_z + hA_o\widehat{S}_z\widehat{I}_z \mid \frac{1}{2}, 0 > \\
&= \frac{1}{2}g_e\beta H && \text{(1.2.6b)} \\
E_{+\frac{1}{2},-1} &=< \frac{1}{2}, -1 \mid g_e\beta H\widehat{S}_z + hA_o\widehat{S}_z\widehat{I}_z \mid \frac{1}{2}, -1 > \\
&= \frac{1}{2}g_e\beta H - \frac{hA_o}{2} && \text{(1.2.6c)} \\
E_{-\frac{1}{2},-1} &=< -\frac{1}{2}, -1 \mid g_e\beta H\widehat{S}_z + hA_o\widehat{S}_z\widehat{I}_z \mid -\frac{1}{2}, -1 > \\
&= -\frac{1}{2}g_e\beta H + \frac{hA_o}{2} && \text{(1.2.6d)} \\
E_{-\frac{1}{2},0} &=< -\frac{1}{2}, 0 \mid g_e\beta H\widehat{S}_z + hA_o\widehat{S}_z\widehat{I}_z \mid -\frac{1}{2}, 0 > \\
&= -\frac{1}{2}g_e\beta H && \text{(1.2.6e)} \\
E_{-\frac{1}{2},1} &=< -\frac{1}{2}, 1 \mid g_e\beta H\widehat{S}_z + hA_o\widehat{S}_z\widehat{I}_z \mid -\frac{1}{2}, 1 > \\
&= -\frac{1}{2}g_e\beta H - \frac{hA_o}{2} && \text{(1.2.6f)}
\end{aligned}$$

Keeping in mind that not all transitions are allowed, selection rules: $\triangle m_s = \pm 1$ and $\triangle m_I = 0$, and applying these rules on equations 1.2.6, only three transitions are allowed as depicted in Figure 1.9.

For the anisotropic system, A_{dip} replaces A_o in equation 1.2.6. Two extreme cases are enough to obtain insight into the effect of the dipolar coupling on the EPR spectrum. The cases are those for which $\theta = 0°$ and $\theta = 90°$ with the help of Figure 1.8. For $\theta = 0°$, $A_{dip} \propto 2A_{dip}$ and for $\theta = 90°$, $A_{dip} \propto -A_{dip}$. Applying the same technique as in the isotropic case lead to the following set of equations with the energy digram shown in Figure 1.9.

Case 1: $\theta = 0°$

$$E_{+\frac{1}{2},1} =< \frac{1}{2}, 1 \mid g_e\beta H\widehat{S}_z + 2hA_{dip}\widehat{S}_z\widehat{I}_z \mid \frac{1}{2}, 1 >$$
$$= \frac{1}{2}g_e\beta H + hA_{dip} \tag{1.2.7a}$$
$$E_{+\frac{1}{2},0} =< \frac{1}{2}, 0 \mid g_e\beta H\widehat{S}_z + 2hA_{dip}\widehat{S}_z\widehat{I}_z \mid \frac{1}{2}, 0 >$$
$$= \frac{1}{2}g_e\beta H \tag{1.2.7b}$$
$$E_{+\frac{1}{2},-1} =< \frac{1}{2}, -1 \mid g_e\beta H\widehat{S}_z + 2hA_{dip}\widehat{S}_z\widehat{I}_z \mid \frac{1}{2}, -1 >$$
$$= \frac{1}{2}g_e\beta H - hA_{dip} \tag{1.2.7c}$$
$$E_{-\frac{1}{2},-1} =< -\frac{1}{2}, -1 \mid g_e\beta H\widehat{S}_z + 2hA_{dip}\widehat{S}_z\widehat{I}_z \mid -\frac{1}{2}, -1 >$$
$$= -\frac{1}{2}g_e\beta H + hA_{dip} \tag{1.2.7d}$$
$$E_{-\frac{1}{2},0} =< -\frac{1}{2}, 0 \mid g_e\beta H\widehat{S}_z + 2hA_{dip}\widehat{S}_z\widehat{I}_z \mid -\frac{1}{2}, 0 >$$
$$= -\frac{1}{2}g_e\beta H \tag{1.2.7e}$$
$$E_{-\frac{1}{2},1} =< -\frac{1}{2}, 1 \mid g_e\beta H\widehat{S}_z + 2hA_{dip}\widehat{S}_z\widehat{I}_z \mid -\frac{1}{2}, 1 >$$
$$= -\frac{1}{2}g_e\beta H - hA_{dip} \tag{1.2.7f}$$

Case 1: $\theta = 90°$

$$E_{+\frac{1}{2},1} =< \frac{1}{2}, 1 \mid g_e\beta H\widehat{S}_z - hA_{dip}\widehat{S}_z\widehat{I}_z \mid \frac{1}{2}, 1 >$$
$$= \frac{1}{2}g_e\beta H - \frac{hA_{dip}}{2} \tag{1.2.8a}$$
$$E_{+\frac{1}{2},0} =< \frac{1}{2}, 0 \mid g_e\beta H\widehat{S}_z - hA_{dip}\widehat{S}_z\widehat{I}_z \mid \frac{1}{2}, 0 >$$
$$= \frac{1}{2}g_e\beta H \tag{1.2.8b}$$
$$E_{+\frac{1}{2},-1} =< \frac{1}{2}, -1 \mid g_e\beta H\widehat{S}_z - hA_{dip}\widehat{S}_z\widehat{I}_z \mid \frac{1}{2}, -1 >$$
$$= \frac{1}{2}g_e\beta H + \frac{hA_{dip}}{2} \tag{1.2.8c}$$
$$E_{-\frac{1}{2},-1} =< -\frac{1}{2}, -1 \mid g_e\beta H\widehat{S}_z - hA_{dip}\widehat{S}_z\widehat{I}_z \mid -\frac{1}{2}, -1 >$$
$$= -\frac{1}{2}g_e\beta H - \frac{hA_{dip}}{2} \tag{1.2.8d}$$
$$E_{-\frac{1}{2},0} =< -\frac{1}{2}, 0 \mid g_e\beta H\widehat{S}_z - hA_{dip}\widehat{S}_z\widehat{I}_z \mid -\frac{1}{2}, 0 >$$
$$= -\frac{1}{2}g_e\beta H \tag{1.2.8e}$$
$$E_{-\frac{1}{2},1} =< -\frac{1}{2}, 1 \mid g_e\beta H\widehat{S}_z - hA_{dip}\widehat{S}_z\widehat{I}_z \mid -\frac{1}{2}, 1 >$$
$$= -\frac{1}{2}g_e\beta H + \frac{hA_{dip}}{2} \tag{1.2.8f}$$

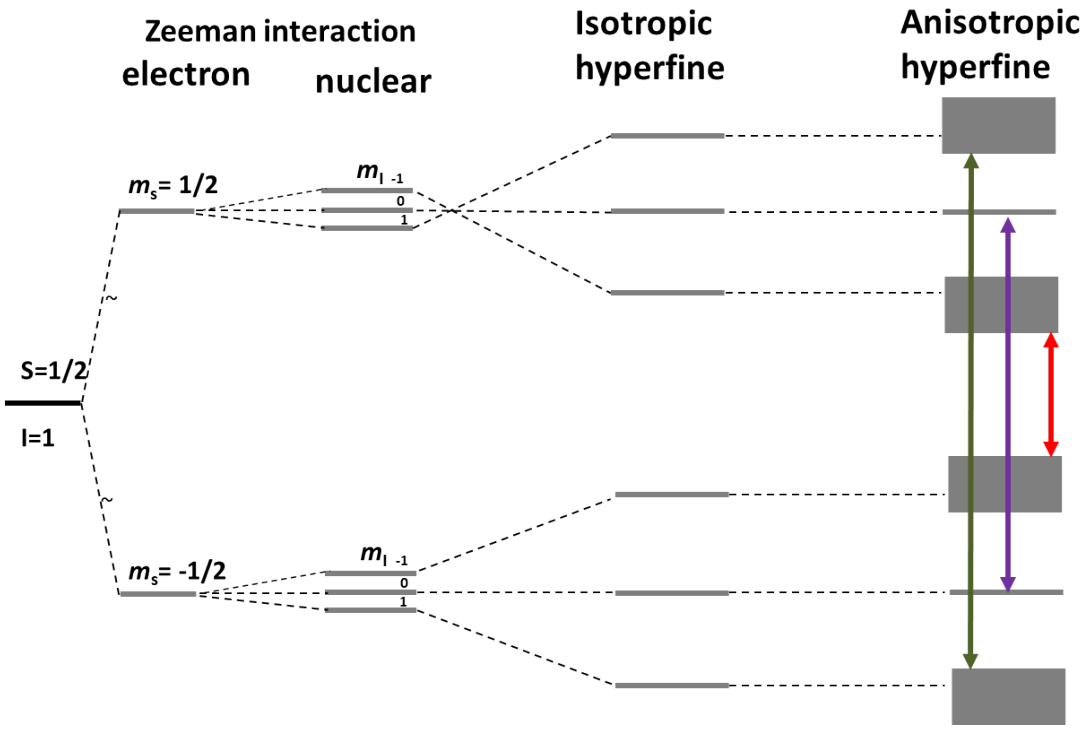

Figure 1.9: Energy level diagram of EPR allowed transitions (green, purple and red) in a nitroxide radical.

1.2.2 Generation of an electron paramagnetic resonance spectrum

As shown in Figure 1.6, the EPR spectrum obtained is the first derivation of the absorption spectrum. In EPR spectroscopy, the spectrum is acquired by a technique known as phase sensitive detection (PSD). [90] Before briefly describing PSD, the most basic requirements for an EPR spectrometer are: (1) A magnetic field **H** to split the Zeeman levels; (2) A microwave source to deliver the energy to drive the the EPR transitions; (3) A microwave detector in order to detect the

absorption of power in the sample; and (4) A means to sweep the magnetic field and record microwave absorption at the same time in the form of a data acquisition unit. Figure 1.10 shows the basic features of a continuous wave EPR spectrometer adapted from [90].

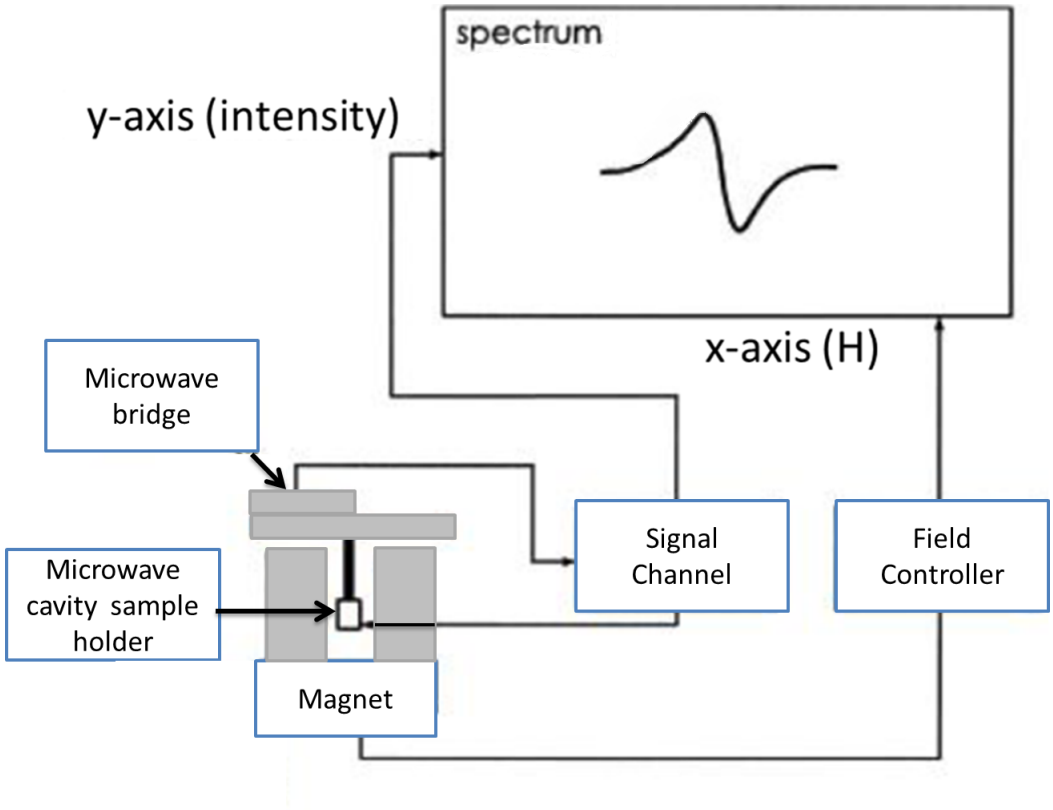

Figure 1.10: The basic features of an EPR spectrometer showing the magnet, cavity, the microwave bridge, and the detection unit.

Briefly, the sample is placed in the microwave cavity between the two magnets. The microwave cavity introdces the magnetic field into the sample and helps to enhances signals from a weak sample. The electromagnetic radiation

and the detection unit are in the bridge. The magnet helps to tune the electronic energy levels and the field controller provides a means to sweep the magnetic field in a controlled and precise manner for an EPR measurement. The latter does this by regulating the magnetic field strength and the sweep parameters.

The signal channel is the component responsible for the PSD. The PSD is a technique that EPR employs to enhance the sensitivity of the spectrometer. This technique ensures that baseline instabilities and noise from detector diodes are minimized while at the same time encodes the EPR signal to make it distinguishable from other sources of interference. Briefly, the signal channel compares a modulated signal with a reference signal having the same frequency as the field modulation and it is only sensitive to signals which have the same phase and frequency as the field modulation. [90] Any signals which do not fulfill these requirements are suppressed. To achieve this, the magnetic field on the sample is modulated sinusoidally at the modulation frequency. If there is an EPR signal, the field modulation quickly sweeps through part of the signal and the microwaves reflected from the cavity are amplitude modulated at the same frequency. For an EPR signal which is approximately linear over an interval as wide as the modulation amplitude, it is transferred into a sine wave with an amplitude proportional to the slope of the signal, hence the observed "derivative" shape of the EPR spectrum, acquired by the EPR spectrometer that uses PSD.

1.3 OVERVIEW

The work described herein characterizes the solvent environment around EAL in order to establish the role of solvent and surface dynamics to the enzyme function. This is achieved through systematic "tuning" of solvent dynamics and glass transitions around the enzyme by using dimethylsulfoxide (DMSO) and T variation. In addition, a mechanism of EAL trafficking and targeting to the Eut BMC is described with the N-terminal domain of the EutC subunit in EAL dictating the motional freedom of that state. This dissertation concludes with work that serves as a verification of the model proposed for the characterization of the solvent environment around EAL, in addition to being a platform to allow for tuning of the steps in EAL catalysis. This is achieved through direct correlation of the solvent dynamics around EAL with the addition of the substrate 2-aminoethanol to the system, albeit without B_{12}, to avoid turnover of enzyme. Overall, the work presented herein is pioneering toward the precise characterization of the solvent phases around EAL and control of solvent and protein surface dynamics as a tunable parameter for quantifying the coupling between solvent and protein fluctuations and catalysis in EAL, and other enzymes.

Chapter 2

Mesodomain and Protein-Associated Solvent Phases with Temperature-Tunable (200-265 K) Dynamics Surround Ethanolamine Ammonia-Lyase in Globally Polycrystalline Aqueous Solution Containing Dimethylsulfoxide

---

The work presented in this chapter is available at

B. Nforneh and K. Warncke, J. Phys. Chem. B 2017, 121, 11109-11118

2.1 INTRODUCTION

Proteins require a minimal level of mobile hydration water, in order to execute native function. [44] The required >1 g water/g protein, corresponding to a hydration shell of thickness approximately two water molecules, arises from a dependence of the functionally-necessary protein fluctuations on solvent motions. [44–46] Reciprocally, water dynamics influenced by protein have been distinguished from bulk water at distances of up to 20 Å from the protein surface, [47] and computational studies suggest mechanistic features of distinct, protein-influenced water dynamics extending to 10 Å. [48, 49] When water is removed by drying, protein fluctuations are lowered in frequency and suppressed in amplitude. [50, 51] Restriction of solvent water motions, by lowering temperature to solidify the solvent, also suppresses protein fluctuations and eliminates function not associated with diffusive exchange of substrates/products. [44, 46, 52] We have shown that the protein, ethanolamine ammonia-lyase (EAL; EC 4.3.1.7), [3] a bacterial enzyme that is involved in gut microbiome homeostasis, [4–6] and in disease conditions wrought by pathogenic strains of $Salmonella$ and $E.\ coli$ in humans, [7,8] maintains the central chemical step of radical rearrangement, deep into the cryogenic temperature regime $(T \geq 190)$, in frozen, polycrystalline aqueous solution. [92, 93, 95] How is the enzyme able to conduct the elaborate rearrangement, and subsequent hydrogen transfer and cobalamin cofactor bond reformation reaction steps, when the bulk aqueous solvent is rigid? Insight comes from studies of the mechanism of cryopreservation, which show that frozen aqueous so-

lutions containing relatively low concentrations of cosolvents or solutes (lower than required to form a global glass) form an interstitial "mesodomain" phase at the ice-crystallite grain boundaries. [53–55] The mesodomain arises during freezing, as cosolvents and other solutes are excluded from the growing multiple, independently-nucleated ice-crystallite regions. The elevated cosolvent concentration lowers the melting temperature of the cosolvent/water mesodomain, and with decreasing temperature, this leads to formation of a high-viscosity fluid, and eventually, an interstitial glassy phase. [114] We hypothesize that, in the presence of cosolvent, a mesodomain phase maintains fluidity and solvent fluctuations sufficient for the observed function of EAL at low temperatures. Here, we support this proposal by quantitatively describing the T-dependence, over 200-265 K, of the mobility of solvent phases that surround EAL in frozen 1% v/v dimethylsulfoxide (DMSO) solution, by using the nitroxide (aminoxyl) electron spin probe, TEMPOL, and continuous-wave electron paramagnetic resonance (EPR) spectroscopy. [90] The TEMPOL mobility in frozen aqueous EAL solution without cosolvent (0% DMSO) is also determined, for comparison.

Nitroxides are stable radicals, that have been used to address the T-dependence of solvent mobility, including phase transitions and glass formation in aqueous phases. [108–110] The rotational motion (tumbling) of the nitroxide is dependent on the medium viscosity, and is thus a proxy for solvent mobility. Tumbling leads to rotational averaging of the unpaired electron g-anisotropy and the electron-^{14}N dipolar hyperfine interaction, and a consequent narrowing of the EPR lineshape, [90] which is quantified by the rotational correlation time (τ_c) obtained

from spectral simulations. The X-band, continuous wave EPR spin probe approach is sensitive to TEMPOL tumbling motion in the τ_c range of 10^{-11} (rapid limit) to 10^{-7} s (defined as the rigid limit). [109] The spin probe approach has been used to characterize the mesodomain in frozen aqueous–sucrose [115] and aqueous-glycerol [110] solutions, in the absence of protein.

Here, we describe a systematic experimental and analytical strategy that leads to identification of solvent components (phases) around the protein and characterization of their T-dependent motional properties in frozen pure aqueous and 1% v/v DMSO aqueous solutions in the presence of EAL (2–20 μM) and trace TEMPOL (0.00034% w/v, 0.2 mM). The pure aqueous system is selected, to address the EAL protein effect on the surrounding solvent, in the absence of cryosolvent, through hydrogen-bonding and possible influences of surface polar amino acid side chains, which have chemical attributes of cryoprotectant molecules. DMSO is selected because it is a common cosolvent component of cryoprotectant mixtures, [116] with well-characterized phase behavior. [117, 118] The phase diagram of aqueous-DMSO solutions, shows water freezing point depression at <82 % v/v, with eutectic points (53 % v/v; 210 K) and (64 % v/v; 203 K), that correspond to the presence of different DMSO hydrates. [117] In fluid, bulk 41% v/v DMSO/water solution at 234-248 K, EAL maintains native reactivity. [94, 96, 119] In the present studies, DMSO is added at concentration of 1% v/v, relative to the total liquid sample volume, which leads to a polycrystalline sample upon freezing (>30% v/v DMSO is required to produce a global glass, at the mean cooling rate of 10 K/s employed here [96]). The results identify two TEMPOL mobility

components, with distinct T-dependences, in both 0 and 1% v/v DMSO solutions with EAL. In the 1% v/v DMSO solution, the components are assigned to a "bulk" mesodomain and a protein-associated domain (PAD), with estimated volume ratio of 1.3, and which correspond to 0.6% of the total sample volume. The results provide an unprecedented microscopic characterization of solvent structure and behavior around a protein in frozen solution, and an advance toward the precise control of solvent dynamics as a tunable parameter for quantifying the coupling between solvent and protein fluctuations and catalysis in EAL, [95, 96] and other enzymes.

2.2 EXPERIMENTAL METHODS

2.2.1 Sample preparation

All chemicals were purchased from commercial sources, including DMSO (purity, $\geq$99.9%; EMD Chemical), and deionized water was used (resistivity, 18.2 MΩ.cm; Nanopure system, Siemens). The EAL protein from $S.\ typhimurium$ overexpressed in $E.\ coli$ overexpression system and purified as described, [10,120] with modifications. [96] The specific activity of purified EAL with aminoethanol as substrate was 20 μmol/min/mg (T=298 K, P=1 atm), as determined by using the coupled assay with alcohol dehydrogenase and NADH. [18] Protein samples included 10 mM potassium phosphate buffer (pH 7.5), 2-20 μM EAL protein (20 μM was the standard concentration), and 0.2 mM TEMPOL spin probe (4-hydroxy-

TEMPO, Sigma-Aldrich) in a final volume of 0.3 ml. When present, DMSO was added to 1% v/v in the final volume of 0.3 ml. Protein and 0% DMSO solution samples were prepared aerobically, on ice in small vials, mixed, and loaded into 4 mm outer diameter EPR tubes (Wilmad-LabGlass). The samples were frozen by immersion in T=140 K isopentane solution. This method has a characteristic cooling rate of 10 K/s. [96] Samples were transferred to liquid nitrogen for storage. Solution (no protein) samples containing 1% v/v DMSO were placed in 2 mm outer diameter EPR tubes, because of their lossiness at T>210 K.

2.2.2 Continuous-wave EPR spectroscopy

CW-EPR experiments were performed by using a Bruker E500 ElexSys EPR spectrometer and ER4123SHQE X-band cavity resonator. A Bruker ER4131VT temperature controller and cooling system, based on nitrogen gas flow through a coil immersed in liquid nitrogen, was used to establish T values of 200-265 K. The Bruker ER4131VT temperature readout was calibrated by using a 19180 4-wire RTD probe and Oxford Instruments ITC503 unit, as described. [96] The uncertainty in T values was $\pm$0.5 K. [96] In the general measurement protocol, an initial EPR spectrum was obtained at T=200 K. The controller was then set to the next higher T-value, and the system was allowed to equilibrate for 5 min at the new T-value. At the end of the 5 min period, the cavity was retuned, and the spectrum was acquired at the new T-value. This procedure was repeated for the entire T range. A baseline sample (all components, but without TEMPOL) was subjected to the same measurement protocol. Accessory, control experiments were

carried out in the direction of decreasing T, starting from 265 K. No hysteresis in correlation times or component amplitudes was observed. No hysteresis was observed for samples subjected to an additional cycle of storage and measurement. Therefore, equilibrium conditions at each T prevail. EPR acquisition parameters: Microwave frequency, 9.45 GHz; microwave power, 0.2 mW; magnetic field modulation, 0.2 mT; modulation frequency, 100 kHz; acquisition number, 4-8 spectra were averaged at each T value.

2.2.3 EPR Simulations

Simulations of the cw-EPR spectra were performed by using the Chili algorithm in the program, EasySpin. [121] Convergence of simulations was defined by the default, local least-squares fitting criteria. Random rotational motion of the spin probe was assumed. The following established [115] set of parameters was used: principal values of the g tensor, g_x = 2.0092, g_y= 2.0102, g_z = 2.0045 (magnetic field-corrected); principal values of the ^{14}N hyperfine tensor, A_x = 20.9, A_y = 19.82, A_z = 103.2 MHz. The τ_c, intrinsic spectral linewidth, and, for two-component simulations, the weights, W, were varied in the simulations. Spectra were corrected by subtraction of the temperature-matched baseline sample spectrum, prior to simulation. The detailed procedure for the simulations is described below.

The τ_c, intrinsic spectral linewidth, and, for two-component simulations, W, were varied in the simulations. Spectra were corrected by subtraction of the temperature-matched baseline sample spectrum, prior to simulation. All derivative-form spectra were initially simulated by using a single tumbling component. If

the single-component fit was unsatisfactory, a two component simulation was performed, in which the contribution of each component was represented by adjustable slow- and fast-tumbling components, with normalized weights, denoted as W_s and W_f, respectively. The two-component simulation was required for all conditions, with the exception of the 1% v/v DMSO solution system. Three-component simulations did not significantly improve the match with experiment.

The two-component simulation procedure was initiated by using the best-fit parameters from the one-component simulation, followed by three iterations of fixing τ_c, the weight and the intrinsic linewidth ("lw" parameter, in EasySpin) of one component, while the other component's parameters were varied, and a fifth iteration with variation of τ_c, weight and intrinsic linewidth of both components. The following final steps in the two-component simulations were performed to assure that the slower-tumbling, broader-line component was correctly represented, and in particular, for T-values at which the slow component was present in small proportion, relative to the faster-tumbling component. This is necessary, because, although the derivative-mode simulation procedure provides rapid convergence to the correct region of the parameter space, the relatively large amplitude of narrow-line, fast-tumbling species overemphasizes the fast-component contribution. Thus, the best-fit parameters from the two-component, derivative-mode simulations were used as the starting parameters for an absorption-mode EPR simulation of the integrated experimental derivative EPR spectrum. In the first iteration, the slow component correlation time, $\tau_{c,s}$, was fixed, and all other adjustable parameters were varied. A scan of $\tau_{c,s}$ about the above fixed value was

performed at up to six increments of ± 0.1 log($\tau_{c,s}$), and the $\tau_{c,s}$ value that gave the best match to the slow component was identified, visually. This final $\tau_{c,s}$ value was then fixed, and log($\tau_{c,f}$) was varied over a range of log($\tau_{c,f}$) ± 0.1, to obtain the final $\tau_{c,f}$ value.

2.3 RESULTS

2.3.1 Temperature dependence of the TEMPOL EPR line shape in frozen aqueous solution with EAL: 0% DMSO

The effect of temperature on the EPR line shape of the TEMPOL spin probe at different representative temperatures from the complete addressed range of 200-265 K is shown in Figure 2.1A, for the EAL, 0% DMSO sample. The characteristic TEMPOL spectrum arises from interaction of the unpaired electron spin ($S = \frac{1}{2}$) with the nitroxide ^{14}N nuclear spin ($I = 1$), which produces three dominant spectral features, that correspond to electron spin-spin transitions ($\triangle m_s = \pm\frac{1}{2}$) among m_I=0, ± 1 energy levels created by the electron-nuclear hyperfine interaction. [90] From 200-240 K, the spectra show the rigid-limit, powder pattern line shape, characterized qualitatively by an overall spectral width of $2A_{zz}$= 7.4 mT = 207 MHz, where A_{zz} is the z-component of the anisotropic hyperfine tensor. At T = 245 K, narrowing of the overall spectral width and widths of individual features indicates the commencement of TEMPOL tumbling motion, which results in further line-narrowing at T>245 K.

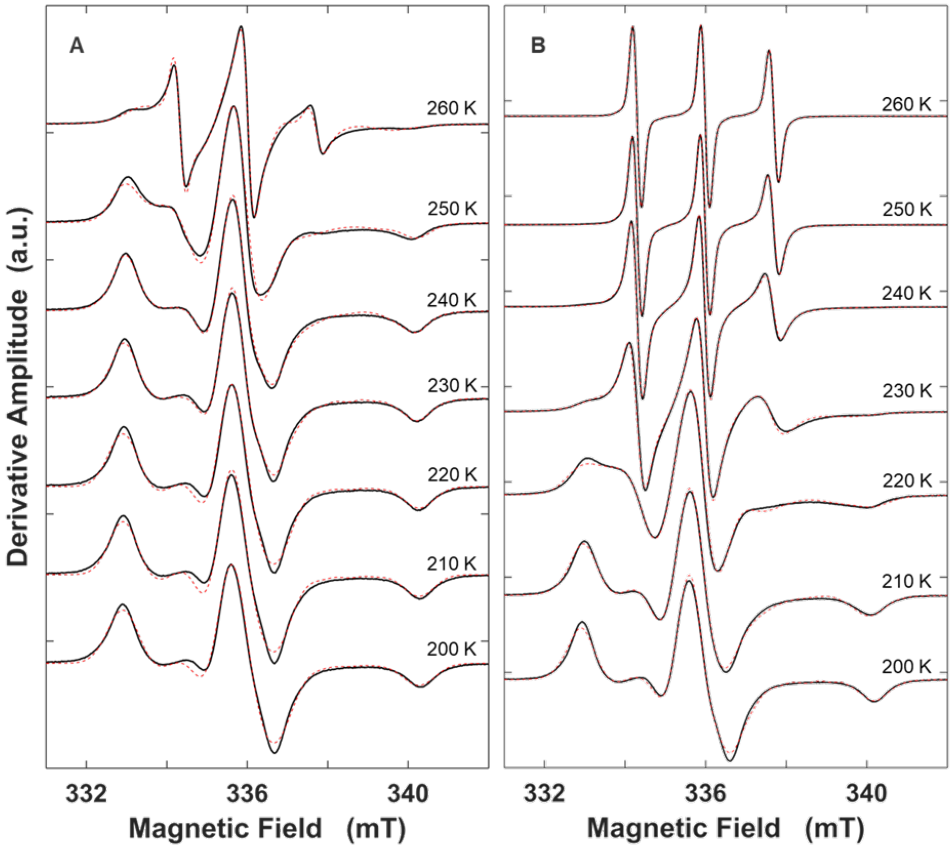

Figure 2.1: Temperature dependence of the TEMPOL EPR spectrum (black) and overlaid two-component EPR simulations (dashed red lines). (A) EAL in aqueous solution, 0% DMSO. (B) EAL in 1% v/v DMSO. EAL concentration was 20 μM. The spectra are normalized to the central peak-to-trough amplitude. Alignment along the magnetic field axis corresponds to the microwave frequency at 200 K.

2.3.2 Temperature dependence of the TEMPOL EPR line shape in frozen aqueous solution with EAL: 1% v/v DMSO

Figure 2.1B shows the EPR line shape at different representative temperatures for frozen aqueous solutions of EAL protein with added 1% v/v DMSO. The rigid-limit, powder pattern line shape is observed for $T \leq$210 K. The overall spectral width and widths of the hyperfine features narrow at $T >$215 K, and this trend continues with increasing temperature. At $T \geq$ 250 K, the electron-nuclear dipolar anisotropy is well-averaged by rapid tumbling, and the overall spectral width approaches twice the value of the ^{14}N isotropic hyperfine coupling constant, $2A_{iso}$=3.4 mT=96 MHz. The comparsion of the line shapes in Figure 2.1 shows that tumbling motion of TEMPOL in 1% v/v added DMSO is activated at $\sim$30 K lower in temperature, relative to to the 0% DMSO solution.

2.3.3 Temperature dependence of the TEMPOL rotational correlation times and normalized component weights in frozen aqueous solution with EAL: 0% DMSO

The EPR spectra were simulated to quantify the rotational mobility in terms of the τ_c and normalized W values of TEMPOL mobility components. The temperature dependence of τ_c in the EAL, 0% DMSO condition displays two-component behavior (Figure 2.2A; values, Table D.1 of Appendix 7.2), where the two components are characterized by a relatively short τ_c value (denoted as the "fast"

tumbling component) and a relatively long τ_c value (denoted as "slow" tumbling component). The temperature-dependence is divided into three regions: Region I (T<230 K): The logτ_c values lie above the tumbling detection criterion. Region II (230$\leq T \leq$250 K): A fast-tumbling population is present, with log$\tau_{c,f}$ decreasing with T, along with a rigid population. Region III (250$< T \leq$265 K): Both fast- and slow-tumbling populations are present, with log$\tau_{c,f}$, log$\tau_{c,s}$<–7.0 and decreasing with T. Figure 2.2B shows that there is a shift in the dominant population from fast (weight, W_f) to slow (W_s). The shift reaches completion at $W_s \approx$0.8.

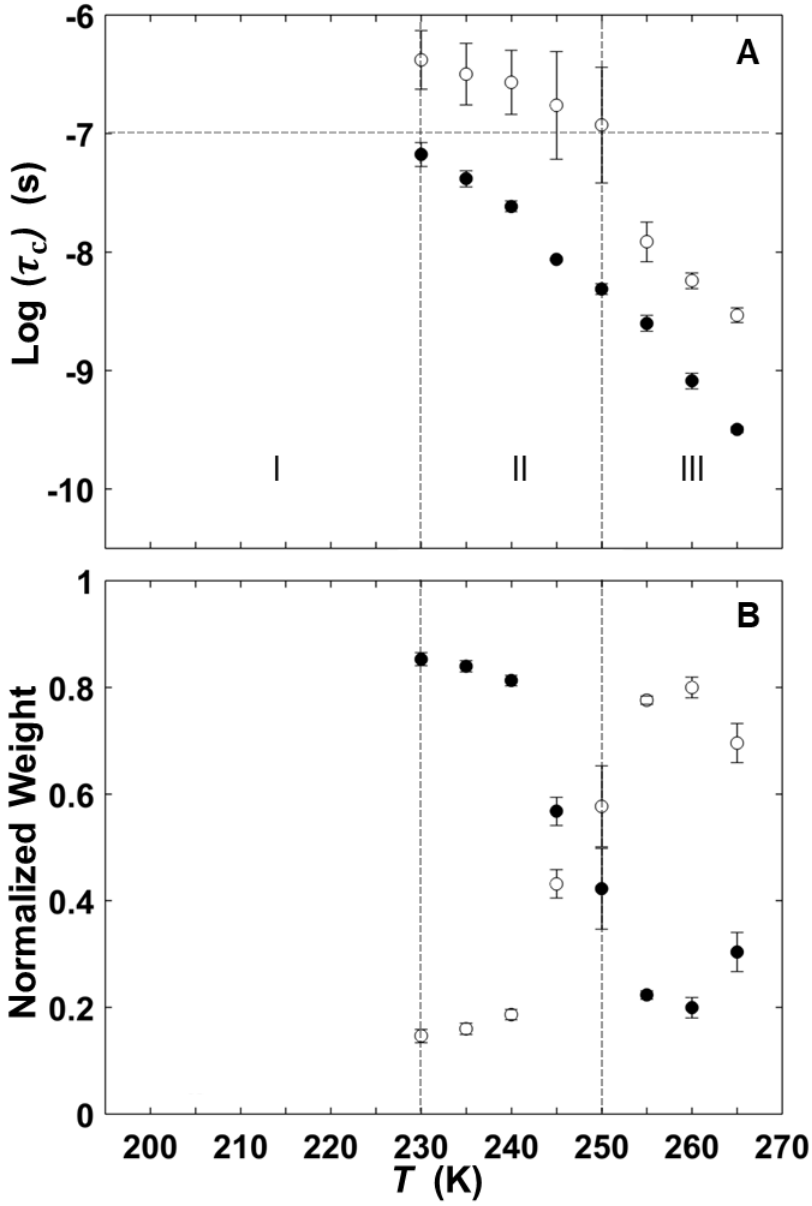

Figure 2.2: Temperature dependence of the rotational correlation time of TEMPOL and normalized mobility component weights, for EAL, 0% DMSO. (A) Rotational correlation time. Horizontal dashed line represents upper limit of τ_c for detection of tumbling motion. (B) Normalized weight. Solid circles: fast component; open circles, slow component. Error bars represent standard deviations for three separate determinations.

2.3.4 Temperature dependence of the TEMPOL rotational correlation times and normalized component weights in frozen aqueous solution with EAL: 1% v/v DMSO

The temperature dependence of τ_c for TEMPOL in the EAL, 1% v/v added DMSO condition displays two-component behavior over 200-265 K (Figure 2.3; values, Table D.2 of Appendix 7.2). Three regions of tumbling behavior are observed, with boundary T values that are lower by 30-40 K, relative to the EAL, 0% DMSO condition: Region I (T<200 K): The logτ_c values lie above the tumbling detection criterion. Region II (200$\leq T$<210 K): A fast-tumbling population is present with decreasing log$\tau_{c,f}$, along with a relatively rigid population. Region III (210$\leq T \leq$265 K): Both fast- and slow-tumbling populations are present, with logτ_c values decreasing with T. Over 215–250 K, the normalized weights of the fast and slow tumbling components remain constant [mean W_f=0.61, W_s=0.39 ($\pm$0.01)]. At T>250 K, W_f increases slightly to a value of 0.7 at 265 K.

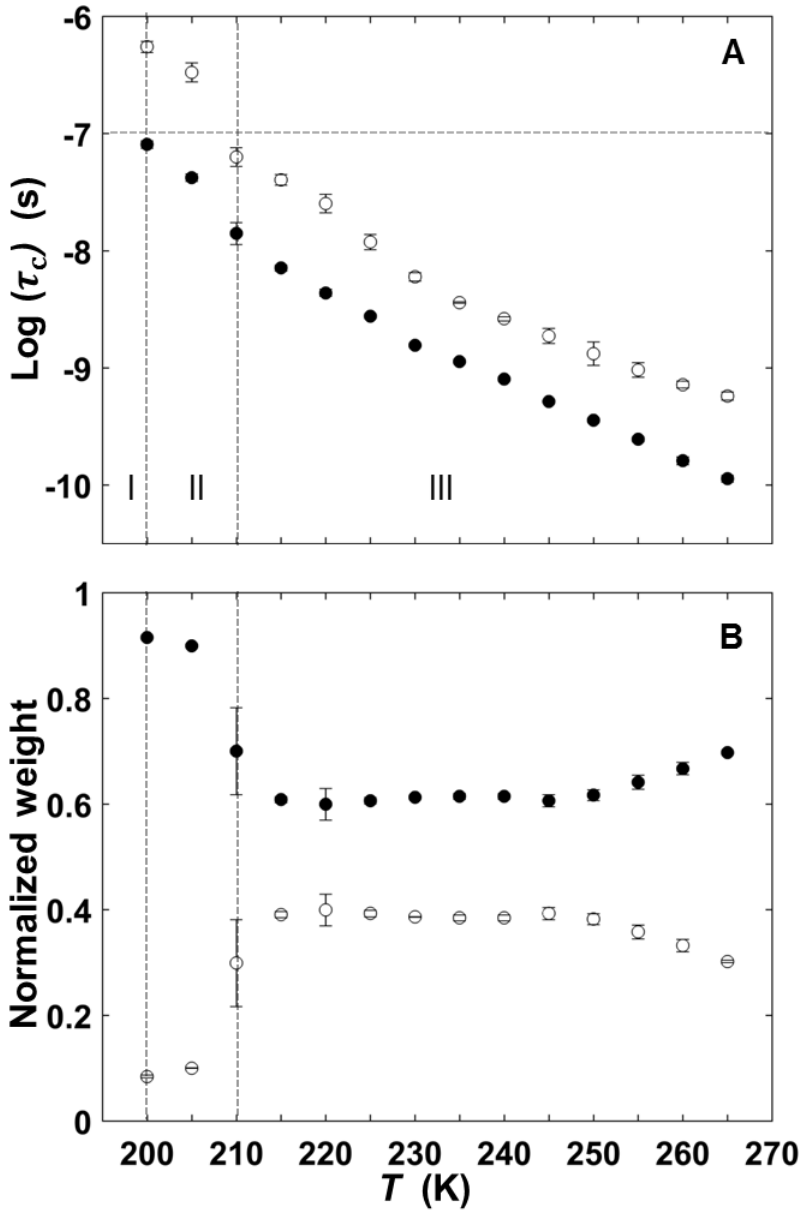

Figure 2.3: Temperature dependence of the rotational correlation time of TEMPOL and normalized mobility component weights, for EAL, 1% DMSO. (A) Rotational correlation time. Horizontal dashed line represents upper limit of τ_c for detection of tumbling motion. (B) Normalized weight. Solid circles: fast component; open circles, slow component. Error bars represent standard deviations for three separate determinations.

2.3.5 Temperature dependence of the TEMPOL rotational correlation times and normalized component weights in the absence of EAL: 0 and 1% v/v DMSO

The origin of the two TEMPOL motional components in the presence of EAL was addressed by examining the motional properties of TEMPOL in solution-only samples. Frozen aqueous solutions at 0% DMSO presented a low-amplitude, single-derivative EPR line shape, with no hyperfine splitting, at all temperatures ($\sim$2 mT, peak-to-trough width), that was centered at g $\approx$2.006 (Figure C.1 of Appendix 7.2). The broad EPR signal is characteristic of multiple, strong electron spin-spin interactions, caused by aggregation of TEMPOL. [122,123] In the frozen pure aqueous solvent system, this is expected to occur at the ice crystallite grain boundaries.

In contrast, frozen 1% v/v DMSO solution yielded characteristic three-line TEMPOL EPR spectra at all temperatures. The spectra were simulated by using a single mobility component (Figure 2.4; values, Table D.3 of Appendix 7.2). This is consistent with the formation of a glassy DMSO-aqueous phase in the frozen 1% v/v DMSO solution, in which the TEMPOL is dispersed. The temperature dependence of the single logτ_c component for TEMPOL in 1% v/v DMSO matches the log$\tau_{c,f}$ component for the $+EAL$ condition (Figure 2.5). The results indicate that the W_f component in the 1% v/v DMSO, EAL condition is associated with a DMSO-aqueous mesodomain phase.

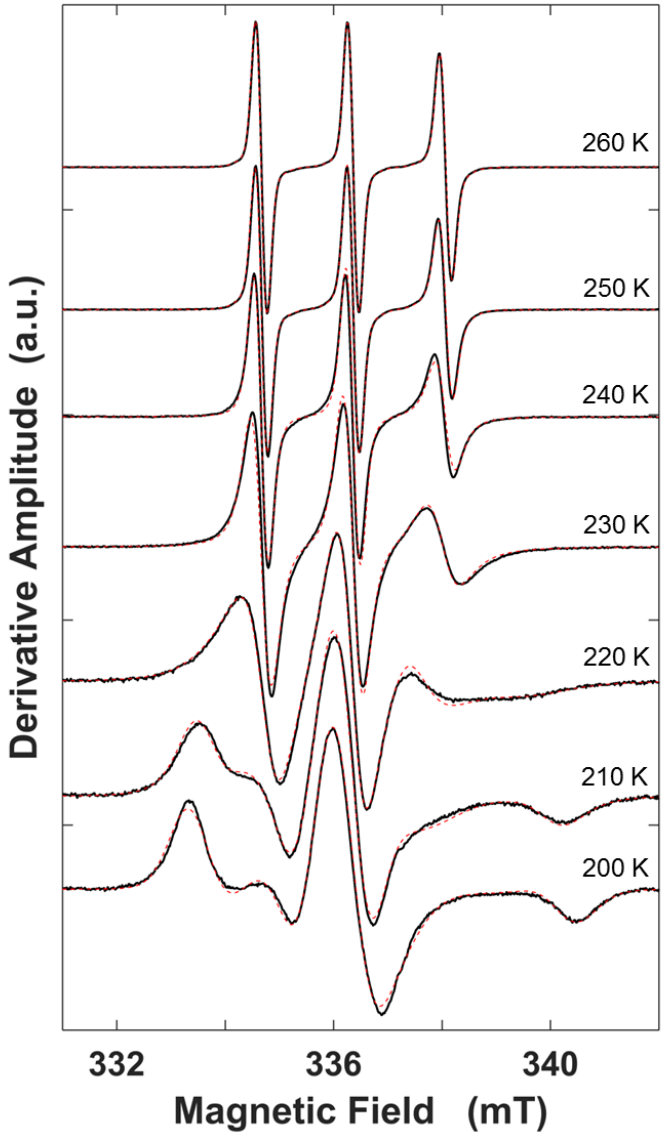

Figure 2.4: Temperature dependence of the TEMPOL EPR spectrum (black) and overlaid single-component EPR simulations (dashed red lines) for 1% v/v DMSO solution in the absence of EAL. The spectra are normalized to the central peak-to-trough amplitude. Alignment along the magnetic field axis corresponds to the microwave frequency at 200 K.

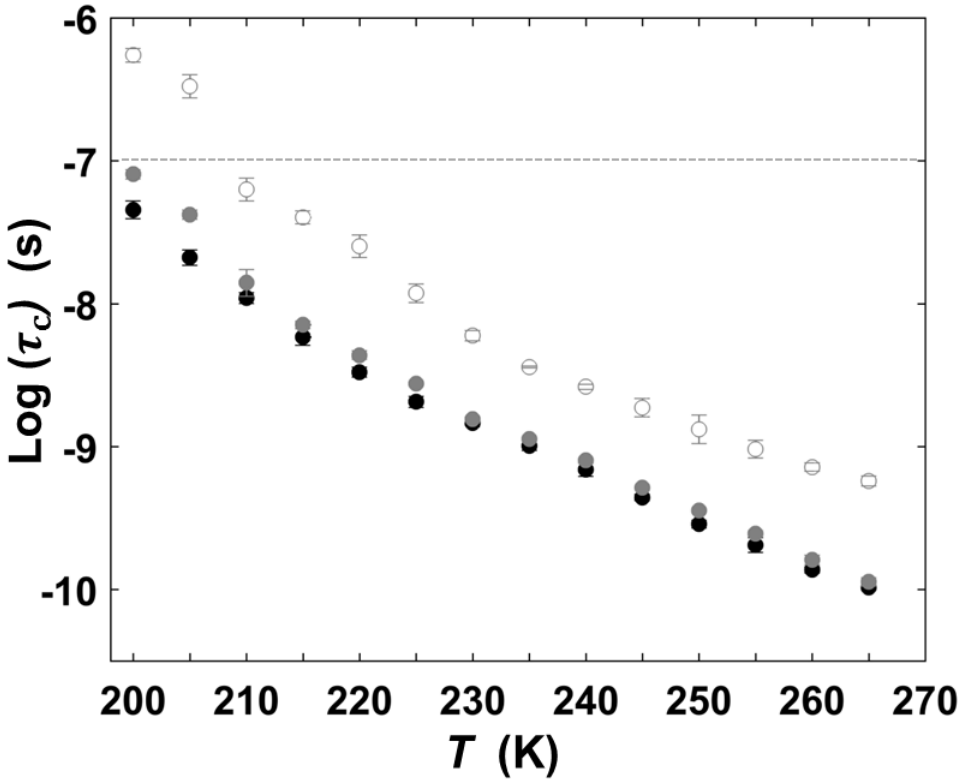

Figure 2.5: Temperature dependence of the rotational correlation time of TEMPOL in 1% v/v DMSO solution in the absence of DMSO (single component, black circles), and comparison with values from 1% v/v DMSO solution in the presence of EAL (filled grey circles, fast component; open grey circles, slow component). Horizontal dashed line represents upper limit of τ_c for detection of tumbling motion. Error bars represent standard deviations for three separate determinations.

2.3.6 EAL protein concentration dependence of the EPR line shape in frozen 1% v/v DMSO solution

To address the possible origin of one of the two TEMPOL motional components from a protein-associated solvent phase, the EAL concentration-dependence of W_f and W_s was determined. Experiments were performed at 1% v/v DMSO, with the concentration of the protein ranging from 2-20 μM. The series of EPR spectra obtained at T=225 K are shown in Figure 2.6. The T-value of 225 K was selected for analysis, because the line shapes of the W_s and W_f components are the most distinct at this temperature, which optimizes the accurate detection of relative changes in weights. EPR absorption mode spectra are presented for best visualization of the full extent of the broad lineshape contributions. Upon the reduction of the protein concentration from 20 to 2 μM, W_s decreases from 0.40 to 0.09, with a compensatory increase in W_f (Table 2.1, Figure 2.7). The observed correlation of lower values of W_s with lower EAL concentrations indicates that the slow mobility component represents a protein-associated phase.

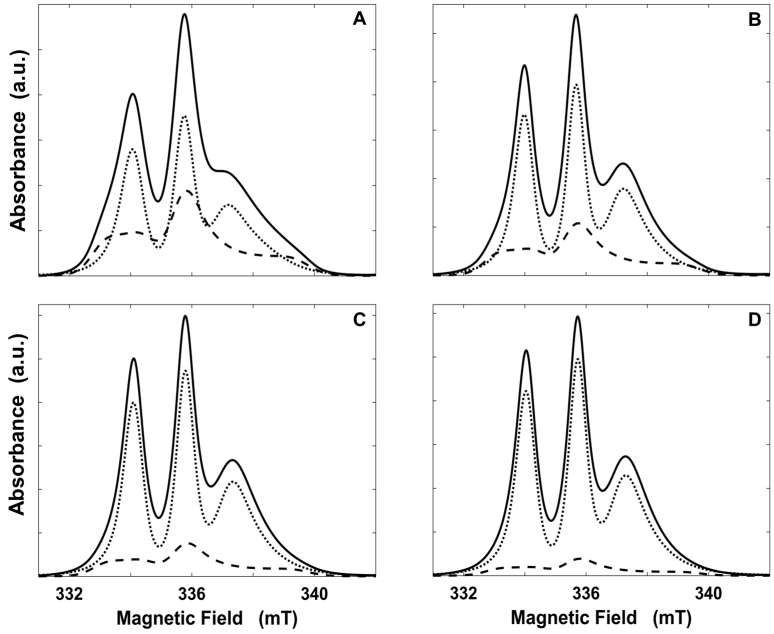

Figure 2.6: Absorption-mode presentation of the EPR spectra for different EAL protein concentrations, and spectral deconvolutions. EAL concentrations: (A) 20 μM, (B) 10 μM, (C) 5 μM, (D) 2 μM. Experimental spectra, black curve; slow tumbling component, grey dashed curve; fast tumbling component, grey dotted curve. Experimental spectra were acquired at 225 K.

Table 2.1: Dependence of the normalized weights for fast and slow tumbling components on EAL protein concentration in 1% v/v DMSO at 225 K.†

[EAL] (μM)	W_f	W_s
2	0.91±0.01	0.09±0.01
5	0.82±0.01	0.18±0.01
10	0.73±0.01	0.27±0.01
20	0.60±0.01	0.40±0.01

† Mean values and standard deviations correspond to three separate experiments

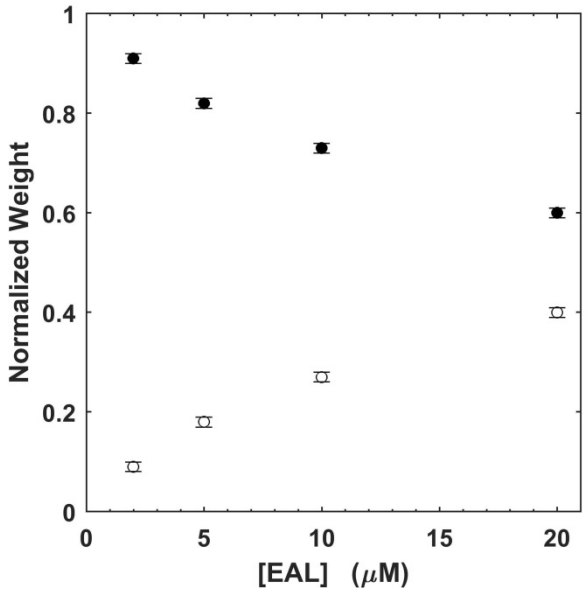

Figure 2.7: Dependence of the normalized weights for fast and slow tumbling components on EAL protein concentration in 1% v/v DMSO at 225 K. Data are from Table 2.1. Fast component, W_f, solid circles; slow component, W_s, open circles.

2.4 DISCUSSION

2.4.1 Origin of the mobility components in the EAL, 0% DMSO condition

Three-line TEMPOL EPR spectra are observed at all T values in 0% DMSO solution in the presence of EAL (Figure 2.1A). In contrast, a weak EPR signal with unresolved hyperfine features is observed in the absence of EAL (Figure C.1 of Appendix 7.2), that indicates TEMPOL aggregation, and consequent paramagnetic broadening and quenching. [122,123] The excellent match of the EPR spectra and two-component EPR simulations at each T value (Figure 2.1, Table D.1 of Appendix 7.2) indicate that population of this aggregate species is not significant in the presence of EAL. Therefore, we propose that the EAL protein creates a region in the immediate vicinity (1-2 solvent diameters) of the protein surface, that forms a glass-like, solid state at low-T, that, along with possible probe-protein interactions, prevents aggregation of the TEMPOL. This model is consistent with the display on the protein surface of amphiphilic, hydrogen-bonding amino acid side chains, [124] which mimic the properties of glass-promoting cosolvents [53–55] in aqueous solution. The activation of detectable TEMPOL tumbling in the presence of EAL at 230 K is also consistent with nuclear magnetic resonance studies, which show that relatively large side chain motions on the ns timescale in hydrated globular proteins become activated over 220-250 K. [125,126]

The origin of the three regions of T-dependence in the EAL, 0% DMSO condi-

tion (Figure 2.2), based on the above model, is described as follows. The protein-vicinal solvent region is rigid at T<230 K (Region 1). At 230 K, detectable TEMPOL mobility signals fluidization of a dominant solvent phase (W_f=0.8), while a smaller TEMPOL component (W_s=0.2) indicates a solvent phase that remains relatively solid. The dominant component is assigned to the protein-vicinal region, in line with the absence of this phase in the water-only (no EAL) system, and because the protein surface residues will disrupt the ice-crystalline hydrogen-bonding network in the vicinity of the protein surface, leading to freezing point depression. The W_s=0.2 component may represent TEMPOL trapped within, or on the border of, the ice crystallite region, or on the protein surface. Over 230-250 K (Region II), the mobility of the protein-vicinal, fast-motional component increases, while the minor slow-motional component remains detectably rigid. Over this same interval, W_f decreases with a compensating increase in W_s. These twin effects, and the maintenance of two-component TEMPOL mobility, suggest that TEMPOL partitions from the protein-vicinal region into a fluidizing, yet relatively viscous, aqueous solvent region, and that the volume of this aqueous region grows with increasing T. Over 255-265 K, W_s achieves a constant value of 0.8. The saturation of W_s at T>255 K (Region III) may correspond to a limit on the spatial range of melting of the ice crystalline region that surrounds the protein.

2.4.2 Origin of the mobility components in the EAL, 1% v/v DMSO condition

The origins of the two mobility components under the EAL, 1% v/v DMSO condition are assigned, as follows: (1) The T-dependence of $\log\tau_{c,f}$ of the W_f component in the presence of EAL matches the T-dependence of the monotonic $\log\tau_c$ for the solution-only (no EAL) condition (Figure 2.5). This indicates that the W_f component for EAL, 1% v/v DMSO corresponds to an aqueous-DMSO solvent mesodomain, with bulk solvent properties. (2) The $\log\tau_{c,s}$ values in Figure 2.5, are distinct from the $\log\tau_{c,f}$ values, indicating that W_s originates from a different phase. The one-decade decrease in EAL oligomer concentration, from 20 to 2 μM, reduces the total protein surface area in the sample, and therefore, reduces the volume of the protein-associated solvent. As shown in Figure 2.6 and Table 2.1, W_s decreases from 0.40 to 0.09 over the same range, with a compensating increase in W_f. Therefore, the W_s component originates from a protein-associated domain, denoted as the PAD.

2.4.3 Mobility transition in the EAL, 1% v/v DMSO system

Three features of Figure 2.5 provide evidence for TEMPOL mobility transitions at the same T value in the mesodomain and PAD, as follows: (1) There is a discontinuity in the $\log\tau_{c,f}$ versus T dependence between 205 and 210 K: Points at T<210 K do not adhere to the extrapolation of the higher-T dependence to lower T values. This discontinuity is caused by the presence of EAL, as shown by the

continuous relation of logτ_c on T for the 1% v/v DMSO solution-only (no EAL) condition over the same T-range. (2) There is an apparent discontinuity in the log$\tau_{c,s}$ versus T dependence between 205 and 210 K. Extrapolation of the T>210 K log$\tau_{c,s}$ dependence to lower T predicts that log$\tau_{c,s}$ $\approx$-7 at 205 K, whereas the data at T $\leq$205 K lie significantly above this value. This suggests that there is a mobility transition in the PAD. (3) Over the same T range of 205-215 K, there is a dramatic change in the fast:slow component ratio of 0.9:0.1 to 0.6:0.4.

Our interpretation of the TEMPOL mobility transition in the EAL, 1% v/v DMSO system, is that the solvent in the PAD undergoes a rigid-to-mobile transition in the range 205<T<210 K. This transition in the PAD influences the solvent dynamics in the mesodomain, which causes the discontinuity in log$\tau_{c,f}$. The influence of the PAD on mesodomain is consistent with the relatively small and comparable volumes of the two phases, as estimated below, and indicates that the PAD and mesodomain abut – that is, they are not spatially isolated, independent domains in the frozen aqueous solution. A movement of $\sim$30% of the total TEMPOL population from PAD to mesodomain occurs upon T decrease between 215 and 205 K. This suggests partial exclusion of TEMPOL from the PAD upon its solidification, which is facilitated by admittance into the still-fluid mesodomain.

2.4.4 Behavior at T-values above the mobility transition in the EAL, 1% v/v DMSO system

In the region, 210$\leq T \leq$250 K, the constant values of W_f, W_s and decreasing values of log$\tau_{c,f}$ and log$\tau_{c,s}$ indicate that the volumes of the protein hydration layer and mesodomain are constant, while the increased thermal energy promotes increased rates of rotational motion for TEMPOL in each phase. At T>250 K, W_f and W_s diverge, indicating that the proportion of TEMPOL in the mesodomain increases, with a compensating loss in the protein hydration layer. This behavior may be caused by melting of the ice-crystalline region on the periphery of the mesodomain, leading to an increase in mesodomain volume.

2.4.5 Relative volumes of the PAD and mesodomain

The W_s and W_f parameters are related to the relative favorability of occupancy (solvation free energy) of TEMPOL in the PAD and mesodomain, as given by the partition coefficient, P (defined as: $P = \frac{[TEMPOL]_{PAD}}{[TEMPOL]_{meso}}$), and a statistical factor, which accounts for different volumes of the phases, V_{PAD} and V_{meso}. The ratio of $\frac{W_s}{W_f}$ can thus be expressed as:

$$\frac{W_s}{W_f} = P\frac{V_{PAD}}{V_{meso}} \tag{2.4.1}$$

The dependence of V_{PAD} on the amount of EAL can be expressed as a scale-factor for the volume of PAD per concentration of EAL, f_{PAD} (units, μL/μM),

multiplied by the concentration of EAL, [EAL] (units, μM). Eq. 2.4.1 becomes:

$$\frac{W_s}{W_f} = P\frac{f_{PAD}[EAL]}{V_{meso}} \tag{2.4.2}$$

Figure 2.8 shows a linear relation between $\frac{W_s}{W_f}$ and [EAL] with approximately zero intercept, within the uncertainty in the weights, which is consistent with Eq. 2.4.2. The linearity indicates that the protein-solvent interaction is uniform over the one-decade range of EAL concentration.

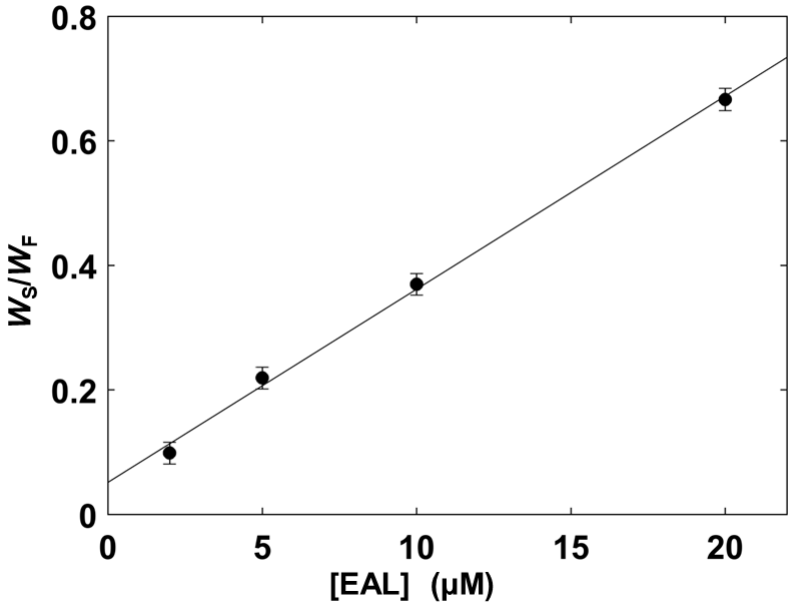

Figure 2.8: Dependence of the ratio of the slow and fast tumbling component weights on the EAL protein concentration, in the 1% v/v DMSO system, at 225 K. Error bars represent standard deviations for three separate determinations (R^2 = 0.9974; R, Pearson's correlation coefficient).

An estimation of the relative dimensions of the PAD and mesodomain is obtained by using Figure 2.8. The slope of the plot, $P\frac{f_{PAD}}{V_{meso}}$ =0.031, allows estimation of V_{meso}, with the assumption of a comparable solvation interaction of TEMPOL with each phase ($P = 1$), and an estimated value of f_{PAD}. An average thickness ($\triangle r$) of the water layer around a protein that displays dynamical properties distinct from bulk water has been identified as $\sim$10 Å, [48, 49] with an upper limit of 20 Å. [47] The accessible surface area of the EAL oligomer is 1.27x10^{5}Å^2, as determined by using ASAView. [127] Thus, values of $f_{PAD}(\triangle r$ = 10 Å) = 2.3x10^{-2} and $f_{PAD}(\triangle r$ = 20 Å) = 4.6x10^{-2} μL/μM are estimated. An alternative estimation is based on a minimum protein hydration level of h=1 gH_2O/g protein for functional dynamics: [44] $f_{PAD}(h = 1)$ = 4.9x10^{-2} μL/μM. These f_{PAD} values give a range of V_{PAD} = 0.46 – 0.98 μL for [EAL]=20 μM. By using the slope relation, $\frac{f_{PAD}}{V_{meso}}$ = 0.031 for assumed $P = 1$, the corresponding range of V_{meso} = 0.74 – 1.58 μL. Therefore, the estimated volumes of the PAD and mesodomain are comparable ($\frac{V_{meso}}{V_{PAD}} \approx 1.6$), for the EAL, 1% v/v DMSO condition. The combined PAD and mesodomain volume is 0.4 – 0.9 % of the total EPR sample volume.

Under standard conditions ([EAL]= 20 μM) for the 1% v/v DMSO system, the total volume of EAL oligomers, estimated by using a mean protein density of 1.35 g/cm^3, [128] is 2.2 μL. Therefore, the estimated relative volumes of the phases, normalized to the volume of a single EAL oligomer, are $V_{meso} : V_{PAD} : V_{EAL} = 0.34 - 0.72 : 0.21 - 0.45 : 1$.

2.4.6 Origin of the temperature-dependence of TEMPOL tumbling mobility

The T-dependence of τ_c over the T-range of fluidity is interpreted in terms of solution-hydrodynamic models [128, 129] to substantiate the phase assignments, and to provide quantification of the composition and uniformity properties of the PAD and mesodomain components. The lifetime of the rotational diffusion of TEMPOL is governed by the solution viscosity, η, and the thermal energy, k_BT, in acccord with the Stokes-Einstein expression,

$$\tau_c = \frac{4\pi\eta a^3}{3K_BT} \tag{2.4.3}$$

where a is the effective hydrodynamic radius of TEMPOL, $\frac{4}{3}\pi a^3$ is the effective TEMPOL volume in the spherical particle limit, and k_B is Boltzmann's constant. The solution viscosity introduces the dominant T-dependence of the tumbling, and can be expressed for glass-forming solutions, in the Vogel-Tammann-Fulcher (VTF) form, [129] as:

$$\eta = \eta_0 \frac{B}{T - T_0} \tag{2.4.4}$$

where the prefactor, η_0, is the reference viscosity (high-T limit, T»T_0), B is a parameter characteristic of the solvent, and T_0 is related to the glass transition T-value. [129] As T exceeds T_0, the argument of the exponential approximates the

Arrhenius form, and $B \rightarrow \frac{E_a}{k_B}$, leading to the following approximate expression:

$$\tau_c \approx \frac{1}{A} exp[\frac{E_a}{k_B T}] \tag{2.4.5}$$

where $\frac{1}{A} = \frac{4\pi a^3 \eta}{3 k_B T}$ incorporates the probe size dependence, and E_a represents a mean barrier to rotational motion of the solvent.

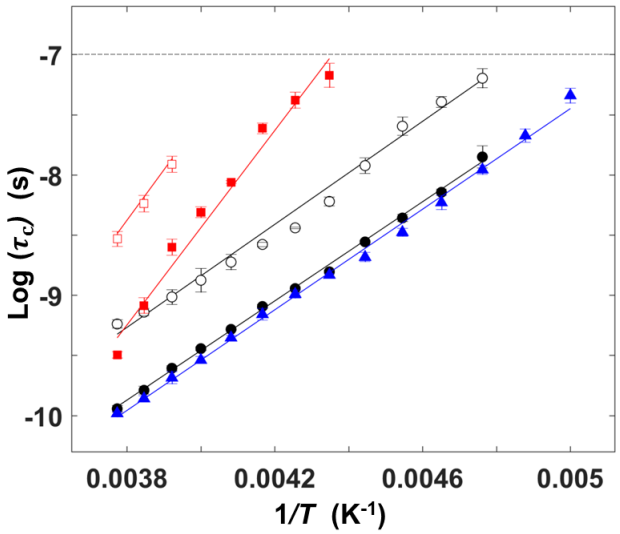

Figure 2.9: Arrhenius plot of rotational correlation times obtained for the different conditions, and overlaid best-fit linear relations. EAL, 0% DMSO (red): fast tumbling component, filled squares; slow tumbling component, open squares. EAL, 1% v/v DMSO (black): fast tumbling component, filled circles; slow tumbling component, open circles. Solution, 1% v/v DMSO (blue): monotonic tumbling component, triangles. Error bars correspond to standard deviations for three separate experiments.

Figure 2.9 shows that Arrhenius plots of $\log\tau_c$ versus $\frac{1}{T}$ for all conditions where $\log\tau_c \leq -7$ (tumbling detection criterion) are linear, and therefore consistent with Eq. 2.4.5 (A, E_a values, Table E.1 of Appendix 7.2). The Arrhenius plots provide further, quantitative support for the models of EAL-associated solvent components by providing the following five insights: (1) The linear dependences indicate that the properties of the solutions are constant over the respective T-ranges, for each solvent component. Thus, the compositions of the protein-associated and mesodomain phases are uniform for $\log\tau_c \leq -7$ over the T-ranges shown in Figure 2.9. (2) The lower E_a values for the EAL, 1% v/v DMSO condition, relative to the EAL, 0% condition, are consistent with the fluidizing effect of DMSO cosolvent on aqueous solutions. [116, 117] (3) The near congruence of the EAL and solution-only 1% v/v DMSO relations in Figure 2.9 provides quantitative evidence that the mesodomain in the presence of EAL represents an aqueous-DMSO phase. (4) The comparable slopes for the EAL, 1% v/v DMSO slow and fast relations suggest that DMSO is present in both the PAD and mesodomain, when $\log\tau_c \leq -7$. (5) The higher $\frac{1}{A}$ value for the slow component suggests that the reference viscosity, η_0, for the PAD is larger than for the mesodomain (assuming the same effective volume of TEMPOL in each phase).

2.5 CONCLUSIONS

The mobility parameters (correlation times, component weights) obtained from EPR spectroscopy and simulations of the TEMPOL spin probe spectra resolve

solvent phases that surround the EAL protein at low-T in frozen, globally polycrystalline aqueous solution, and report on the T-dependence of their rigid and fluid states. In the qualitative model for the EAL, 0% DMSO condition, a protein-vicinal solvent component detectably fluidizes at 230 K, and melts the surrounding ice-crystalline region with increasing T, creating a bounded aqueous solvent domain with relatively high viscosity, up to 265 K. In the quantitative model for the EAL, 1% v/v DMSO condition, two distinct concentric solvent phases are resolved around EAL: PAD and mesodomain. The DMSO-enriched aqueous mesodomain phase fluidizes at low T (200 K), followed at higher T (210 K) by fluidization of the PAD. Our model for the T-dependence of mobilities in the two phases is depicted in Figur 2.10.

The solvent rigid-to-mobile transition in the PAD at 200 K elicits a mobility change in the mesodomain, which demonstrates coupling between the solvent motions in the two phases. The interphase dynamical coupling is consistent with the spatial arrangement of the system, and significant contact area, as inferred from the estimated mean volume ratio of the concentric solvent components and EAL protein molecule, $V_{meso} : V_{PAD} : V_{EAL} = 0.5 : 0.3 : 1.0$. The results provide a rationale, and foundation for interpretation, of the reactions of EAL in frozen aqueous solutions at T<250 K, [92, 96] and represent an advance toward the precise control of solvent dynamics as a tunable parameter in quantifying the coupling between solvent and protein fluctuations, and chemical reaction steps in EAL and other enzymes.

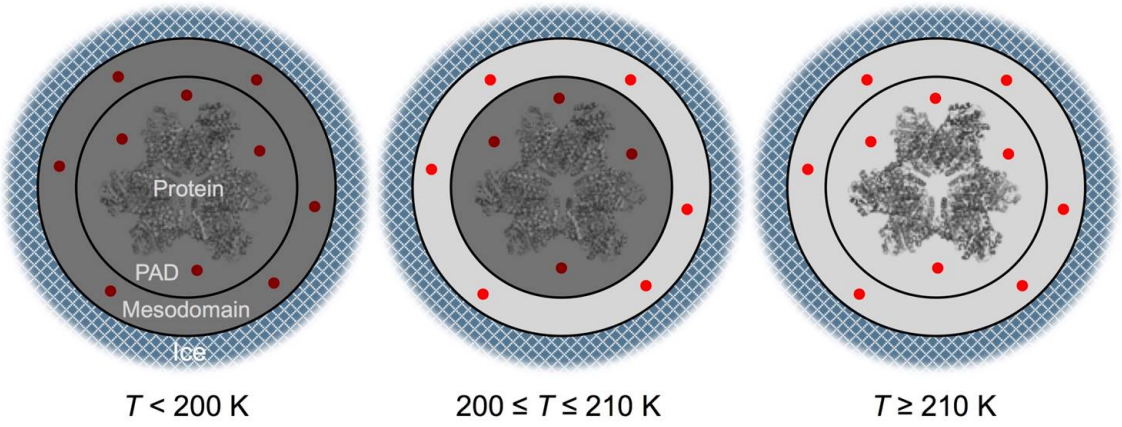

Figure 2.10: Model for the solvent phases that surround the EAL oligomer in frozen, 1% v/v DMSO-water solution and depiction of the temperature-dependence of the solvent mobilities. Detectably rigid (dark gray) or fluid (light grey) mesodomain and protein-associated domain (PAD) phases are reported by TEMPOL (small circles; stoichiometry, 10 per EAL oligomer), where TEMPOL is rigid ($\tau_C > 10^{-7}$ s; dark red) or tumbling ($\tau_C \leq 10^{-7}$; red). The depicted mesodomain, PAD, and protein sizes correspond to the experiment-based, estimated volumes of each phase, and the calculated volume of EAL.

Chapter 3

Ice Boundary and Protein Suface Confinement Effects Govern Protein-associated and Mesodomain Solvent Dynamics Around the B_{12}-Dependent Ethanolamine Ammonia-Lyase Protein in Frozen Aqueous-Dimethylsulfoxide Solutions

---

3.1 INTRODUCTION

The rich, hierarchical repertoire of configurational states characteristic of a native, folded protein at room temperature (T) are bridged by fluctuations among the positions of individual atoms, amino acid side chains, polypeptide backbone, and conformational domains. [44, 45, 126] Water is essential for protein configurational fluctuations. In the dehydrated state, amplitudes of protein motions are severely suppressed. Study of partially hydrated protein powder samples avoids interference of bulk solvent water in scattering and spectroscopic studies, which indicate that graded addition of water up to a hydration level (h, g water/g protein) of $\sim$ 0.5 increases the amplitudes of a broad spectrum of local and collective motions. [50, 51] At h = 1-2, an approximately two water molecule thick ($\sim$ 6 Å) layer of water surrounds the protein [44] and is sufficient to support basic native protein functions, such as small molecule (CO) migration through the interior of heme proteins. [44] In solution systems, bulk phase water, that surrounds the hydration layer, enables larger scale, conformational fluctuations, such as CO entry/exit in myoglobin. [44] Unique structural and dynamical characteristics of the protein hydration water, distinguished by experiment [47] and calculation, [48] extend 10 - 20 Å from the protein surface into the bulk phase. Understanding the interplay of protein, hydration layer and bulk solvent dynamics is essential for molecular-mechanistic description of protein function. Two views of protein-water dynamical coupling, that frame further mechanistic inquiries, have emerged: (1) The protein is a passive material, whose local/incremental

and larger-scale/collective atom motions are driven by solvent fluctuations in the hydration layer and bulk solvent, respectively ("unified model"). [44] (2) The protein has its own integral dynamics, which are promoted, or "plasticised", and augmented by interactions with water. [130] Measurements of fast (> ns) [131] and slow (< μs) [132] dynamics at multiple, specific amino acid sites on proteins suggest a hybrid view.

We address the dynamics of surrounding solvent phases and their coupling to protein by using electron paramagnetic resonance (EPR) spectroscopy of the paramagnetic nitroxide (aminoxyl) spin probe, TEMPOL [90, 110, 133] in a fully-hydrated system including bulk-like solvent, over a wide temperature (T) range, 195–265 K: EAL enzyme from Salmonella typhimurium in frozen polycrystalline aqueous solutions containing dimethylsulfoxide (DMSO) as cosolvent (added prior to freezing at 0.5 – 4.0% v/v). TEMPOL tumbling leads to rotational averaging of the unpaired electron (S = 1/2) g-anisotropy and the electron-^{14}N (I = 1) dipolar hyperfine interaction, and a consequent narrowing of the EPR lineshape, [90] which is quantified by the rotational correlation time (τ_c) obtained from spectral simulations. X-band, continuous wave-EPR is sensitive to TEMPOL tumbling motion in the τ_c range of $\sim 10^{-11}$ (rapid limit) to $\geq 10^{-7}$ s (defined as the rigid limit) as described in Chapter 2. The X-band EPR spin probe approach has been used to characterize the mesodomain in frozen, bulk-polycrystalline aqueous–sucrose, [115] and aqueous-glycerol, [110] in the absence of protein.

During freezing of the low-concentration DMSO solution from ambient T, an interstitial mesodomain is created by the exclusion of DMSO from the grow-

ing ice crystallite domains. This is a general property of cosolvents that form glasses when mixed with water, including cryoprotectants. [53–55, 114] TEMPOL is also excluded from the ice domains. [115, 133] The cosolvent concentration in the mesodomain is elevated to the maximum freeze-concentration (MFC, 64% v/v), which corresponds to the eutectic point in the T-composition dependence. [114, 117] The aqueous-DMSO in the mesodomain forms a viscous fluid with a glass transition temperature, T_g, that corresponds to the calorimetrically-determined pure solution value, $\sim$ 145 K. [117] Previous measurements of the T-dependence of TEMPOL spin probe mobility in frozen solutions $\pm$EAL and added 1% v/v DMSO, resolved two solvent phases that surround EAL as described in Chapter 2: (1) a relatively low-mobility, protein-associated domain (PAD; proposed to correspond to the protein hydration layer), with a resolved fluid–solid transition at T=210 K, and (2) a relatively high-mobility, surrounding fluid aqueous-DMSO mesodomain phase. The assignment of the PAD solvent phase was based on the direct dependence of its total volume (V_{PAD}) on varied EAL concentration.

Here, we use different added DMSO concentrations of 0.5, 2.0 and 4.0% v/v to vary the volume of the mesodomain (V_{meso}), relative to the fixed V_{PAD}. Variation of V_{meso} alters the T-dependence of the solvent dynamics represented by the respective τ_c values in the fluid PAD and mesodomain, and the T-value of the resolved order-disorder transition in the PAD. The results are interpreted in terms of surface confinement effects [134–136] of the protein and ice boundary that surrounds the mesodomain. In particular, the ice boundary confinement

effect is attenuated by the controlled increase of V_{meso}. The results reveal fundamental mechanistic features of solvent-protein dynamical coupling, and provide a framework for understanding the contributions of solvent-coupled protein dynamics to the catalytic mechanism of EAL, [92,93,95,96] toward molecular-level understanding of the roles of EAL in gut microbiome homeostasis [4] and disease conditions. [7,8]

3.2 EXPERIMENTAL METHODS

3.2.1 Sample preparation

All chemicals were purchased from commercial sources, including DMSO (purity, $\geq$99.9%; EMD Chemical), and deionized water was used (resistivity, 18.2 MΩ.cm; Nanopure system, Siemens). The EAL protein from $S.\ typhimurium$ was overexpressed in $E.\ coli$ and purified as described in Chapter 2. Protein samples included 10 mM potassium phosphate buffer (pH 7.5), 20 μM EAL protein, and 0.2 mM TEMPOL spin probe (4-hydroxy-TEMPO, Sigma-Aldrich) in a final volume of 0.3 ml. When present, DMSO was added to 0.5, 2.0, and 4.0% v/v, respectively in the final volume of 0.3 ml. The frozen, polycrystalline EPR samples were prepared as described in Chapter 2 and samples without protein containing 0.5, 2.0, and 4.0% v/v DMSO, respectively were placed in 2 mm outer diameter EPR tubes.

3.2.2 Continuous wave EPR spectroscopy and EPR Simulations

Continuous wave EPR measurements were performed by using a Bruker E500 ElexSys EPR spectrometer and ER4123SHQE X-band cavity resonator as describedn in Chapter 2. EPR acquisition parameters: Microwave frequency, 9.45 GHz; microwave power, 0.2 mW; magnetic field modulation, 0.2 mT; modulation frequency, 100 kHz; acquisition number, 4-8 spectra were averaged at each T value.

Simulations of the cw-EPR spectra were performed by using the Chili algorithm in the program, EasySpin [121] as described in Chapter 2.

3.3 RESULTS

3.3.1 Temperature dependence of the TEMPOL EPR line shape in frozen aqueous solution with EAL: 0.5, 2.0 and 4.0% v/v DMSO

The effect of T on the EPR line shape of the TEMPOL spin probe at different representative T values from the complete addressed range of 200-265 K is shown in Figure 3.1 for the EAL, 0.5, 2.0 and 4.0% v/v DMSO samples. For all DMSO concentrations, the rigid-limit, powder pattern line shape is observed at the lowest T value, and at the highest T values, the widths of the m_I lines narrow, and the overall spectral width approaches twice the value of the ^{14}N isotropic hyperfine coupling constant ($2A_{iso}$=3.4 mT=96 MHz). The transition from the rigid-limit, powder pattern line shape to initial motional-narrowed spectra, that represent

averaging of the electron-nuclear dipolar anisotropy by tumbling of the TEMPOL, occurs at different T values, that decrease with added DMSO concentration: T>210 K for 0.5, $T \geq 210$ K for 2.0, and T>200 K for 4.0% v/v. Continuing this trend, the T values at which significant line-narrowing occurs, owing to rapid tumbling, also decrease with added DMSO concentration: $T \geq 250$ K for 0.5, $T \geq 240$ K for 2.0 and T>230 K for 4.0% v/v. Therefore, the line shapes in Figure 3.1 qualitatively show that tumbling motion of TEMPOL in 4.0% v/v added DMSO is detectably activated at ≈15 K and ≈5 K lower in T, relative to the 0.5 and 2.0% v/v DMSO solution, respectively, and that the transition to rapid tumbling motion in 4.0% v/v added DMSO is detectably activated at ≈15 K and ≈5 K lower in T, relative to the 0.5 and 2.0% v/v DMSO solution, respectively.

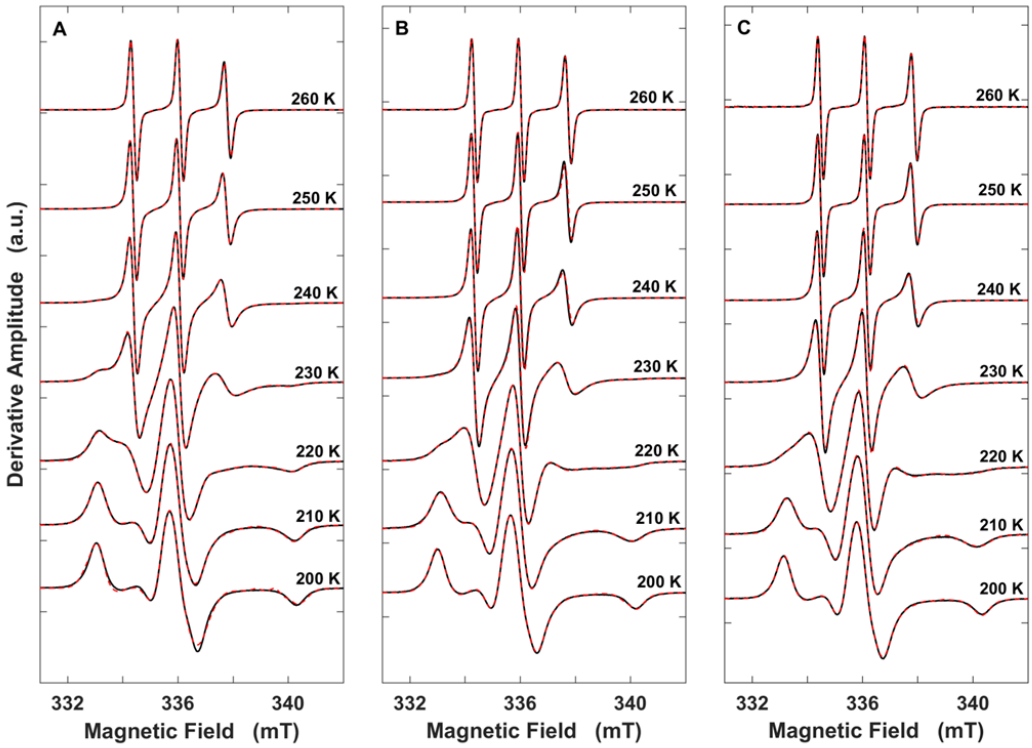

Figure 3.1: Temperature dependence of the TEMPOL EPR spectrum (black), in the presence of EAL, at different added % v/v DMSO, and overlaid two-component EPR simulations (dashed red lines). (A) 0.5%. (B) 2%. (C) 4%. The spectra are normalized to the central peak-to-trough amplitude. Alignment along the magnetic field axis corresponds to the microwave frequency at 200 K.

3.3.2 Temperature dependence of the TEMPOL rotational correlation times and normalized component weights in frozen aqueous solution with EAL: 0.5, 2.0 and 4.0% v/v DMSO

The EPR spectra were simulated to quantify the rotational mobility in terms of the τ_c and normalized W values of TEMPOL mobility components (values, Table K.1, K.2, and K.3 of Appendix 7.2). The temperature dependence of τ_c in the presence of EAL at 0.5, 2.0, and 4.0% v/v DMSO displays two-component behavior, where the two components are characterized by a relatively short τ_c value (denoted as the "fast" tumbling component, $\tau_{c,f}$) and a relatively long τ_c value (denoted as "slow" tumbling component, $\tau_{c,s}$). The dependence of logτ_c on T in Figure 3.2 (A, B, C) is divided into four regions, as follows: Region I: Both logτ_c values lie above the tumbling detection criterion of logτ_c>-7.0. Region II: A fast-tumbling population is present, with log$\tau_{c,f} \leq -7.0$ and decreasing with T, along with a rigid population (simulated logτ_c>7.0). The T value, at which the log$\tau_{c,f}$ and log$\tau_{c.s}$ values meet the criterion for detectable tumbling of ≤ -7.0, $T_{III,II}$, marks the boundary of Region II and Region III. The $T_{III/II}$ value decreases with increasing % v/v DMSO, as previously reported for 1 versus 0% v/v DMSO in Chapter 2. Region III: Both fast- and slow-tumbling populations are present, with log$\tau_{c,f}$ and log$\tau_{c,s}$ continuing to decrease with T. Figure 3.2 (D, E, F) shows that, for all % v/v DMSO conditions, the normalized weights of the slow component (W_s) and fast component (W_f) display a transition, that is centered near the boundary of Region II and Region III (at $T_{III/II}$), at which W_s joins W_f as a de-

tectable tumbling component (Table 3.1). With increasing T across the transition, there is a shift in population from W_f to W_s. Above the transition,W_f and W_s are constant. Region IV: The W_f versus T dependence displays a subtle increase in the proportion of W_f for all DMSO concentrations at $T \geq 250$ K.

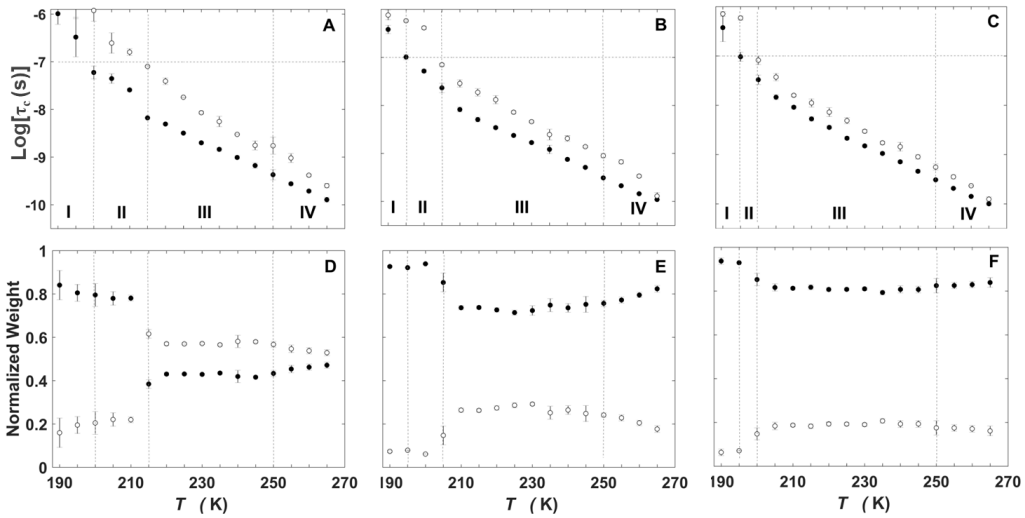

Figure 3.2: Temperature dependence of the rotational correlation time of TEMPOL and normalized mobility component weights, in the presence of EAL, at different added % v/v DMSO. Rotational correlation time. (A) 0.5%. (B) 2%. (C) 4%. Horizontal dashed line represents upper limit of τ_c for detection of tumbling motion. Normalized component weight. (D) 0.5%. (E) 2%. (F) 4%. In each panel, solid circles represent the fast component and open circles represent the slow component. Error bars represent standard deviations for three separate determinations.

3.3.3 Temperature dependence of the TEMPOL spectral line shape in the absence of EAL: 0.5, 2.0 and 4.0% v/v DMSO

Frozen aqueous solutions with 0.5, 2.0 and 4.0% v/v DMSO, in the absence of EAL (–EAL), yielded characteristic three-line TEMPOL EPR spectra at all T values (Figure 3.3). A single component is observed, as reported previously for 1.0% v/v DMSO in the absence of EAL in Chapter 2. For all DMSO concentrations, the general trend of transformation of the rigid-limit, powder pattern line shape to the motionally-averaged spectrum at higher T values, as observed for the +EAL samples, is reproduced.

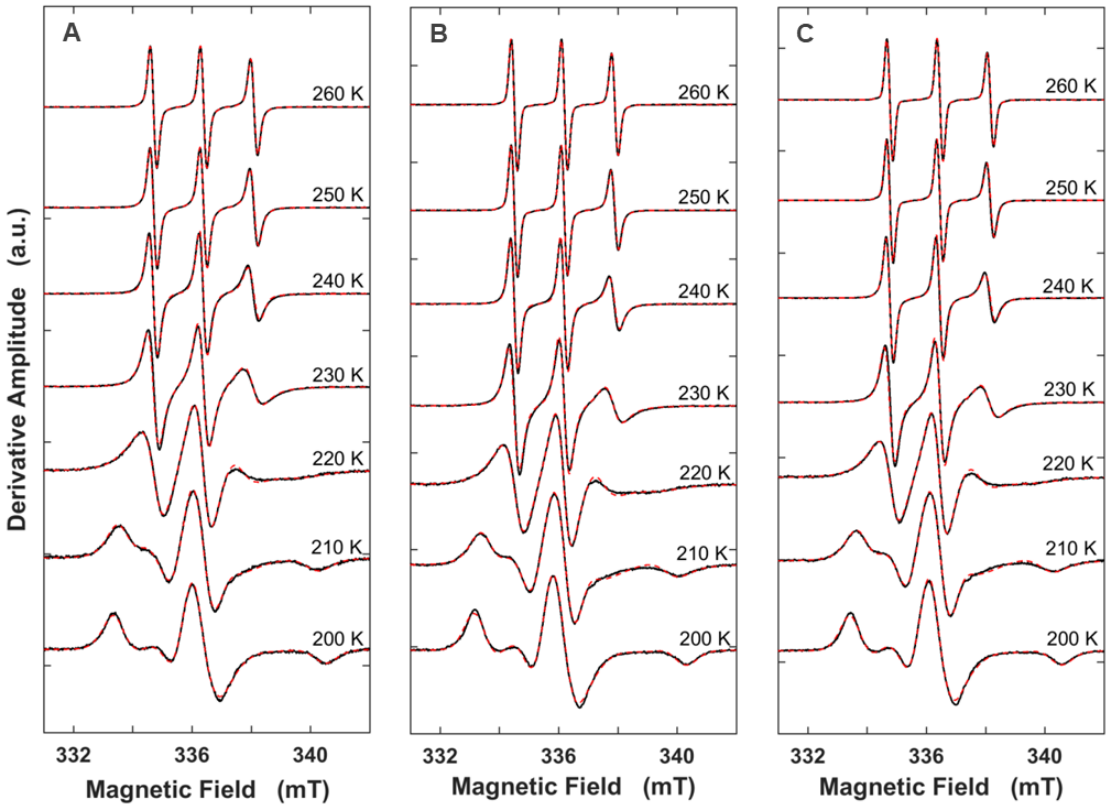

Figure 3.3: Temperature dependence of the TEMPOL EPR spectrum (black), in the absence of EAL, at different added % v/v DMSO, and overlaid two-component EPR simulations (dashed red lines). (A) 0.5%. (B) 2%. (C) 4%. The spectra are normalized to the central peak-to-trough amplitude. Alignment along the magnetic field axis corresponds to the microwave frequency at 200 K.

3.3.4 Temperature dependence of the TEMPOL rotational correlation times and normalized component weights in solution, in the absence of EAL: 0.5, 2.0 and 4.0% v/v DMSO

The EPR spectra for 0.5, 2.0 and 4.0% v/v DMSO in the –EAL condition were simulated (Figure 3.3) by using a single mobility component (single τ_c value, Table K.4, K.5, and K.6 of Appendix 7.2). As shown in Figure 3.4, the T-dependences of $\log\tau_{c,f}$ (+EAL) and $\log\tau_c$ (-EAL) are comparable for each condition. The results indicate that the W_f components in the 0.5, 2.0 and 4.0% v/v DMSO, EAL conditions are associated with a DMSO-aqueous mesodomain phase, as concluded previously for the 1.0% v/v DMSO condition descibed in Chapter 2. The $\log\tau_{c,s}$ values are distinct from the monotonic $\log\tau_c$ values (Figure 3.4), indicating that Ws originates from a different phase. This pattern has been previously reported in 1.0% v/v DMSO solution (Chapter 2) in the presence and absence of EAL, where it was established, from the EAL concentration dependence of W_s, that the W_s component originates from the PAD.

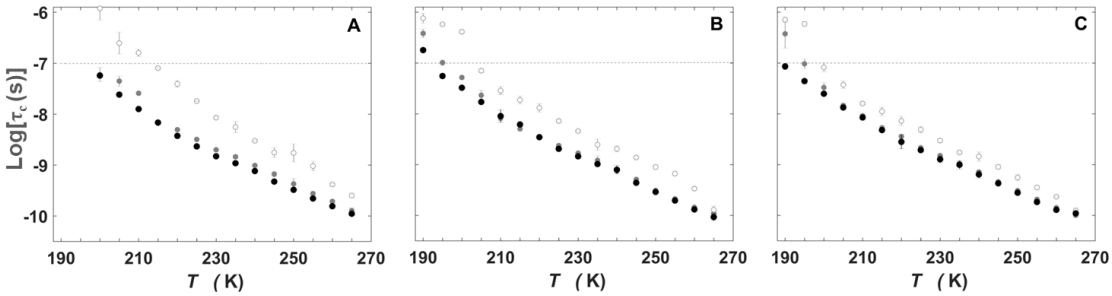

Figure 3.4: Temperature dependence of the rotational correlation time of TEMPOL, in the absence and presence of EAL, at different added % v/v DMSO. (A) 0.5%. (B) 2%. (C) 4%. In each panel, black solid circles represent the single component, –EAL, and grey solid (fast) and open (slow) represent components, +EAL. Horizontal dashed line represents upper limit of τ_c for detection of tumbling motion. Error bars represent standard deviations for three separate determinations.

3.4 DISCUSSION

3.4.1 Added DMSO resides predominantly in the mesodomain

The W_f and W_s values are constant in Region III at each value of added % v/v DMSO, but as the added DMSO increases, the constant value of W_f increases, and W_s correspondingly decreases (Figure 3.2). We propose that the mesodomain increases in volume relative to the PAD, as the added % v/v DMSO is increased, and that the larger reservoir of mesodomain recruits a higher proportion of TEMPOL, by mass-action. This model is quantified by using the following expression, Eq. 2.4.1 described in Chapter 2, that relates the measured W_f and W_s values to

the partition coefficient (P) of TEMPOL between the mesodomain and PAD, and the volumes of the two solvent components (V_{meso}, V_{PAD}):

$$\frac{W_s}{W_f} = P\frac{V_{PAD}}{V_{meso}} \tag{3.4.1}$$

The volume of the mesodomain is dependent on the amount of added DMSO as:

$$V_{meso} = \Gamma_{meso}(\%v/vDMSO) \tag{3.4.2}$$

where Γ_{meso} is a proportionality constant [units, μL/(added % v/v DMSO)]. Combination of Eqs. 3.4.1 and 3.4.2 gives:

$$\frac{W_s}{W_f} = \frac{PV_{PAD}}{\Gamma_{meso}(\%v/vDMSO)} \tag{3.4.3}$$

Figure 3.5 shows the linear relationship predicted by Eq. 3.4.3, which indicates that V_{meso} increases uniformly with increasing added % v/v DMSO. The slope, $\frac{PV_{PAD}}{\Gamma_{meso}}$, is 0.64 (units, added % v/v DMSO), and the ordinate intercept is $\approx$ zero, within the uncertainty.

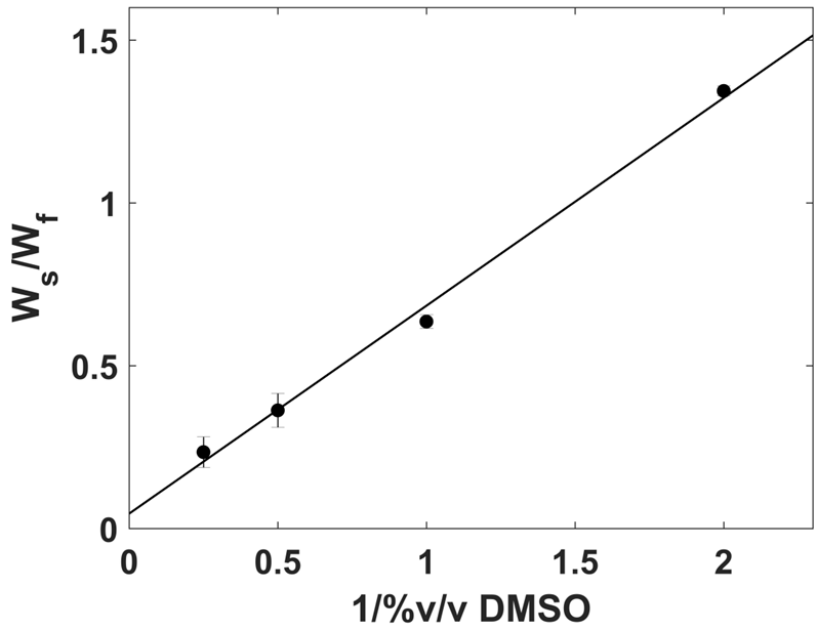

Figure 3.5: Dependence of the ratio of the slow- and fast-tumbling component weights on the inverse concentration of added DMSO in Region III (dual fluid phases), and overlaid best-fit linear relation (R^2=0.9950). Error bars represent standard deviations for three data sets. Slope= 0.64 $\pm$ 0.07 intercept= 0.05 $\pm$ 0.02.

In Chapter 2, V_{PAD} was shown to be linearly dependent on EAL concentration, and thus, independent of V_{meso}. The DMSO concentration in the mesodomain is assumed to be the MFC, 65% v/v. Any DMSO present at equilibrium in the PAD will therefore remain at the same concentration, over the range of added DMSO. DMSO has been shown to be excluded from the protein hydration layer (promoting the "preferential hydration" condition), thus promoting the native state of folded proteins. [137] A folded state of EAL in the DMSO-mesodomain

system is supported by native function at low T values in fluid, bulk aqueous-DMSO (41% v/v) solution, [94,96,119] as well as in polycrystalline solution with aminoalcohols as cosolvents. [92, 96] Together, these results suggest that a negligible proportion of the added DMSO resides in the PAD. Therefore, the linear relation in Figure 3.5 arises solely from the increase of mesodomain volume with increased added DMSO.

3.4.2 Relative dimensions of mesodomain, PAD and EAL

A simple model for the structure and dimensions of the EAL/PAD/mesodomain system is based on considering the EAL protein as surrounded by continuous, uniform layers of PAD and mesodomain. [133] An upper limit on mesodomain volume is estimated by using Eq. 3.4.1 and the measured W_s, W_f values, with the following assumptions: (1) All added DMSO resides in the mesodomain, at the MFC value of 65% v/v. (2) The solvation interaction of TEMPOL with each fluid phase is comparable ($P = 1$, Eq. 3.4.1). Thus, for the representative condition of added 2.0% v/v DMSO, V_{meso} is 9.2 μL. V_{PAD} for 20 μM EAL is 3.0 μL. The corresponding volumes of mesodomain and PAD associated with each EAL oligomer (3.0 mg, 4.0x10^{15} EAL per sample, based on a molecular mass, 4.88x10^5 g/mol [12]) are 2.6x10^6 Å^3 and 8.0x10^5 Å^3, respectively. The accesssible surface area (ASA) of EAL, calculated [127] for the X-ray crystallographic structure [1]-based model for the $S.\ typhimurium$ oligomer, [12] is 1.3x10^5 Å^2. Therefore, the heights of PAD and mesodomain layers for a planar equivalent of the ASA are h_{PAD}=6 Å and h_{meso}=20 Å, for 2.0% v/v added DMSO. The h_{PAD}=6 Å value is

consistent with the 10 – 20 Å thickness of the layer of protein-associated water that is distinguished from bulk water by using experimental [47] and computational [54] techniques. Therefore, the model identifies the PAD as corresponding to the "protein hydration layer". The sequence of calculated h_{meso} values for added 0.5, 1.0 (Chapter 2), 2.0, and 4.0% v/v DMSO is approximately 5, 10, 20 and 40 Å, thus covering a range from h_{meso}<h_{PAD} to h_{meso}>h_{PAD}. The relative dimensions of EAL and solvent phases are depicted in Figure 3.6. The simple planar-layer model captures global features of the solvent environment of EAL, but ignores the topography and heterogeneous chemical nature of the EAL protein surface, [1,12] which might lead to solvent clustering and regions of varying layer thickness, especially at the lowest added DMSO concentration of 0.5% v/v.

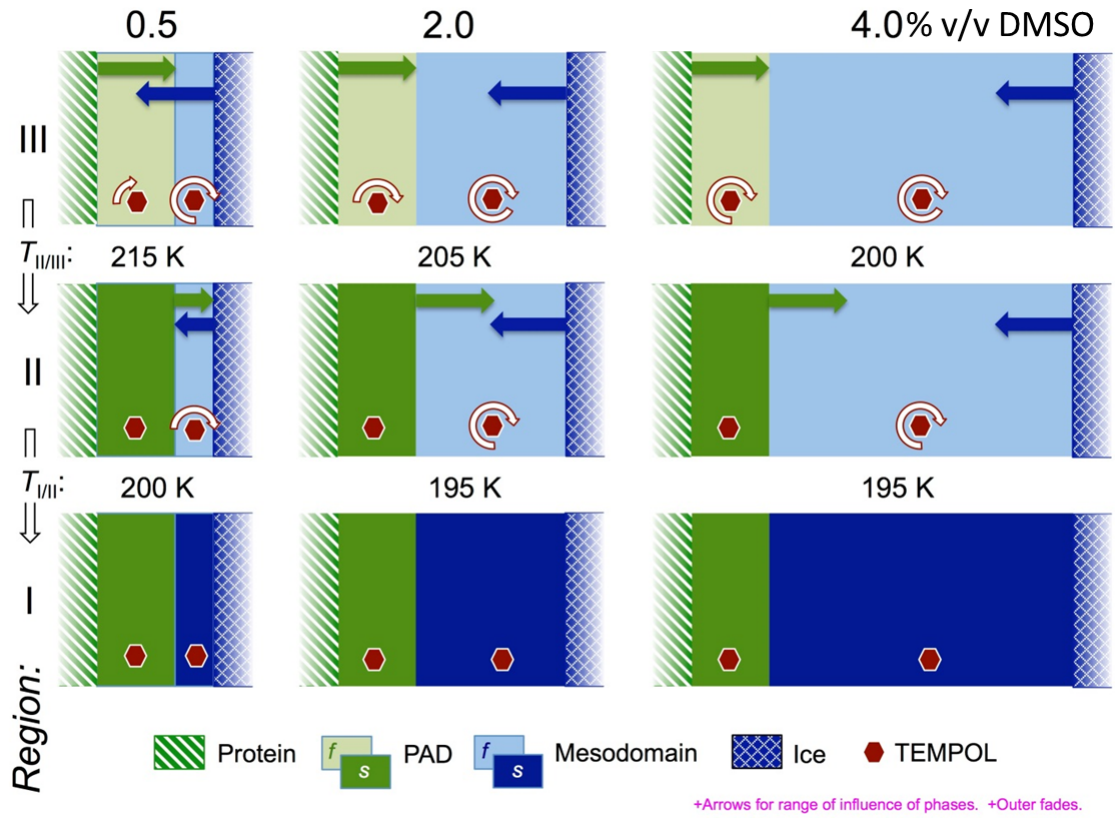

Figure 3.6: Model of the solvent phases that surround the EAL oligomer in frozen, 0.5, 2 and 4% v/v DMSO-water solutions and depiction of Regions I, II and III of Figure 3.2.

3.4.3 Resolution of an order-disorder transition in the protein-associated domain

The abrupt transition in TEMPOL mobility from fast→slow, marked by a compensating decrease in W_s and increase in W_f, in the direction of decreasing T at

the Region III/II boundary (at $T_{III/II}$), indicates transition from a disordered to ordered phase in the PAD (order-disorder transition). This change in W values occurs over a T-range for which both PAD and mesodomain are fluid (log$\tau_{c,s}$, log$\tau_{c,f}$ < -7.0), and therefore, is not an artifact of exceeding the bandwidth of the spin-probe EPR technique at X-band. The transition is identified with the PAD, because the mesodomain maintains the fluid state across $T_{III/II}$. We propose that the origin of the change in weights, quantified as $\triangle W_s$=$W_{s,II}$ – $W_{s,III}$, where $W_{s,II}$ and $W_{s,III}$ are the slow component weights in Regions II (rigid PAD) and III (fluid PAD), arises from a partial exclusion [138] of TEMPOL from the PAD, upon increased solvent order in the PAD. The change in weight can be expressed as:

$$\epsilon = \frac{\triangle W_s}{W_{s,III}} \tag{3.4.4}$$

Where the exclusion coefficient, ϵ, represents the normalized weight component of TEMPOL that is excluded from the PAD and transferred into the mesodomain. The mean value of ϵ for the different % v/v DMSO conditions is 0.70 $\pm$ 0.07 (Table 3.1). Thus, 70% of the TEMPOL in the fluid PAD is excluded, upon the disorder-to-order transition. The value of ϵ is independent of DMSO concentration, and therefore, independent of the volume of the mesodomain, which provides additional evidence for a constant PAD volume at the different % v/v DMSO. Overall, the analysis supports the model of a fluid/solid phase transition in the PAD, at $T_{III/II}$.

Table 3.1: Fluid-solid boundary temperatures among Regions I, II, and III, and slow and fast mobility component weights and relations for TEMPOL in Regions II and III, in the presence of EAL, at different added concentrations of DMSO.

%v/v DMSO	$T_{III/II}$ **(K)**	$T_{II/I}$ **(K)**	$W_{f,II}$‡	$W_{s,II}$‡	$W_{f,III}$‡	$W_{s,III}$‡	$\triangle W$‡,†	$\triangle W$†/$W_{s,III}$
0.5	215	200	0.79	0.21	0.43	0.57	0.36	0.63±0.04
1*	210	200	0.91	0.09	0.6	0.39	0.30	0.77±0.06
2	205	195	0.93	0.07	0.73	0.27	0.20	0.74±0.10
4	200	195	0.94	0.06	0.81	0.1	0.13	0.66±0.10

*previously reported value in Chapter 2.

†defined as $\triangle W$=$W_{s,III}$-$W_{s,II}$= $W_{f,II}$-$W_{f,III}$

‡= value ± 0.01-0.02

3.4.4 Composition and fluidity of the mesodomain

The comparable temperatures of 195-200 K for the Region II/I boundary, denoted as $T_{II/I}$, are consistent with a constant composition of the mesodomains for 0.5 to 4.0% v/v added DMSO (Figure 3.2). $T_{II/I}$ is specified by the bandwidth limitation of the spin-probe EPR technique (logτ_c=-7.0). An order-disorder transition of the mesodomain is not detected, and therefore lies below 195 K. This is consistent with $T_g \approx$ 145 K for homogeneous aqueous-DMSO solution at the MFC. [117]

3.4.5 Temperature-dependence of spin probe mobility in mesodomain and PAD in Region III

The tumbling motion of the TEMPOL probe can be related to the solvent dynamics in the PAD and mesodomain by solution hydrodynamic models as described in Chapter 2. The lifetime of the rotational diffusion of TEMPOL is related to the continuum solvent property, viscosity, η, and the thermal energy, k_BT, by the Stokes-Einstein expression (2.4.3):

$$\tau_c = \frac{4\pi\eta a^3}{3K_BT} \tag{3.4.5}$$

where a is the effective hydrodynamic radius and $\frac{4}{3}\pi a^3$ is the effective volume of TEMPOL in the spherical particle limit (V_s), and k_B is Boltzmann's constant. The η parameter introduces the dominant, exponential T-dependence of the tumbling. [129] For glass-forming phases, such as the aqueous-DMSO mesodomain, a Vogel-Tammen-Fulcher expression is commonly used to characterize the T-dependence: [129]

$$\eta = \eta_0[\frac{DT_0}{T - T_0}] \tag{3.4.6}$$

where η_0 is the reference viscosity high-T limit, and D and T_0 are the empirical fragility constant, D, and divergence temperature, T_0, respectively. The form of Eq. 3.4.6 accounts for the T-dependence of the energy landscape, [139] which is manifested as curvature in the logη versus $1/T$ relation that is observed for

moderately strong to fragile glass-forming solutions when η is measured over a suitable T-range. The corresponding T-dependence of τ_c is given by:

$$\tau_c = \frac{\eta_0 V_s}{k_B T} exp[\frac{B}{T - T_0}] \tag{3.4.7}$$

Figure 3.7 shows plots of $\log\tau_c$ versus $\frac{1}{T}$ for the –EAL and the +EAL conditions in the measured T range, at T » T_g of the mesodomain, are, however, nominally linear, in contrast to the form of Eq. 3.4.7. Therefore, toward quantification of the differences in T-dependences under the different conditions, and for comparison with results of others, we use the following empirical relation to fit the data:

$$\tau_c = \tau_{c,0} exp[\frac{E^*}{RT}] \tag{3.4.8}$$

where the mean time-prefactor,$\tau_{c,0}$, incorporates η_0 and the probe size dependence, R is the gas constant, and E^* represents a mean energy barrier to solvent motion that facilitates probe rotation. The $\log\tau_{c,0}$ and E^* values are provided in Table 3.2.

3.4.6 Combination of protein and ice boundary confinement effects lead to DMSO-concentration–dependence of solvent mobility and the order-disorder transition in the PAD

Figure 3.7A shows a subtle trend of decreasing slope and increasing y-intercept (decreasing E^* and increasing $\tau_{c,0}$) with increased % v/v DMSO for the –EAL system (values, Table 3.2). We interpret this as a confinement effect, [134–136] of the rigid ice matrix, that forms the boundary around the mesodomain, as depicted in Figure 3.6. Microscopically, this arises from hydrogen-bond and polar interactions between the mesodomain solvent and ice, that restrict solvent motion in the vicinity of the ice boundary. The decrease in this confinement effect at higher added DMSO concentrations is consistent with an increased volume of the mesodomain, and therefore, mean TEMPOL distance from the ice boundary. The comparable relations for 2.0 and 4.0 in Figure 3.7A suggests that bulk-like behavior of the dominant volume of mesodomain is reached at 4.0% v/v DMSO.

Figure 3.7A also shows that the relations for $\log\tau_{c,f}$ for the +EAL condition, and $\log\tau_c$ for –EAL, are overlapping for 2.0 and 4.0% v/v DMSO. This implies that the dynamical properties of the mesodomains $\pm$EAL are comparable, at 2 and 4% v/v DMSO (Figure 3.6).

Figure 3.7B shows the $\log\tau_{c,s}$ and $\log\tau_{c,f}$ versus $1/T$ relations for the PAD and mesodomain under the +EAL conditions. The relations for $\log\tau_{c,s}$ display a dramatic decrease in slope and increase in y-intercept from 0.5 to 2.0% v/v DMSO, followed by a smaller change at 4.0% v/v DMSO. This trend indicates

dual, mobility-suppressing confining effects of the ice boundary and the protein surface, as illustrated for Region III in Figure 3.6. At 0.5% v/v DMSO, the relatively small volume of the mesodomain transmits the influence of the ice boundary confinement to the PAD. As the volume of the mesodomain grows with increased added DMSO, the diminishing influence of the ice boundary on PAD dynamics is replaced by the influence of the unrestricted mesodomain, which exerts a fluidizing effect on the PAD (Figure 3.6), and the $\log\tau_c$ versus $1/T$ relation for the PAD more closely approaches the mesodomain relations (Figure 3.7). The positive offset of the PAD curve from the mesodomain relation at 4% v/v DMSO represents the mean restrictive confinement effect of the protein surface on the vicinal solvent region, in the presence of effectively "bulk" fluid solvent (Figure 3.6, Region III).

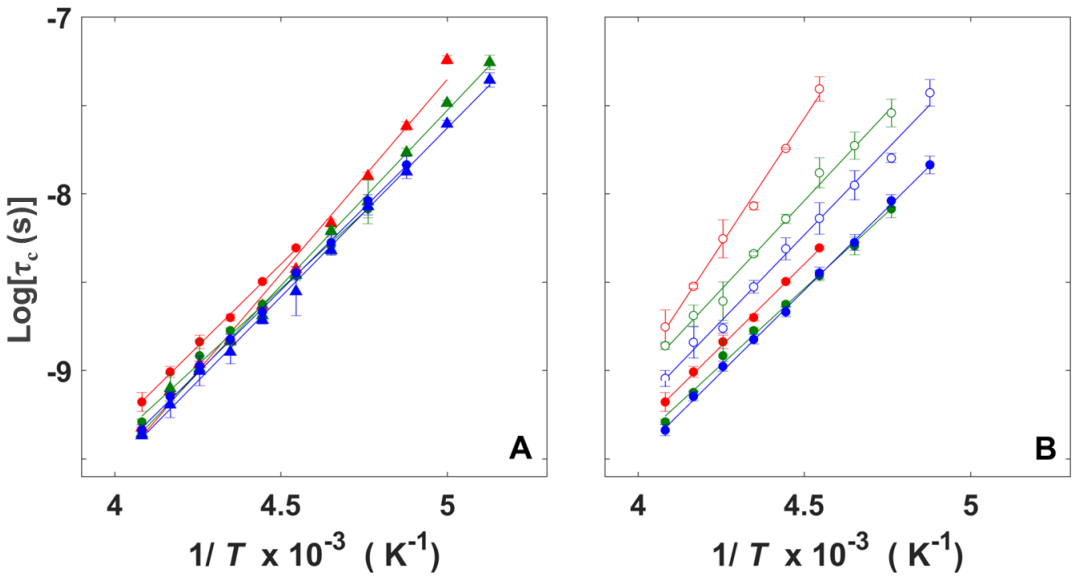

Figure 3.7: Arrhenius plots of rotational correlation times and overlaid best-fit linear relations. (A) Fast component, +EAL (circles), and single component, –EAL (triangles), at added DMSO concentrations: 0.5 (red), 2 (green), and 4 (blue) % v/v. (B) Slow (open circles) and fast (solid circles) components, +EAL, at added DMSO concentrations: 0.5 (red), 2 (green), and 4 (blue) % v/v. Arrhenius parameters from the linear fits are given in Table 3.2. Error bars correspond to standard deviations for three separate experiments at each temperature.

Table 3.2: Arrhenius parameters obtained from the temperature-dependence of the rotational correlation time for TEMPOL tumbling motion in the absence and presence of EAL, for different added concentrations of DMSO.[a]

Condition: ±EAL,% v/v DMSO	$\log \tau_{c,0}$ **(s^{-1})**	E^* **(kcal mol^{-1})**	R^2 [b]
-EAL, 0.5	-18.35 ± 0.36	10.10 ± 0.36	0.9921
+EAL, 0.5, fast	-16.76 ± 0.21	8.50 ± 0.22	0.9986
+EAL, 0.5, slow	-20.43 ± 0.58	13.10 ± 0.62	0.9954
-EAL, 2	-17.44 ± 0.20	9.06 ± 0.20	0.9967
+EAL, 2, fast	-16.30 ± 0.23	7.89 ± 0.23	0.9966
+EAL, 2, slow	-17.09 ± 0.39	9.20 ± 0.40	0.9925
-EAL, 4	-17.17 ± 0.16	8.73 ± 0.15	0.9978
+EAL, 4, fast	-16.93 ± 0.11	8.52 ± 0.12	0.999
+EAL, 4, slow	-17.00 ± 0.33	8.91 ± 0.33	0.9931

[a] Values correspond to linear fits of results in Arrhenius plot of data over the range of temperatures for which $\log\tau_c \leq 7.0$.

[b] R is Pearson's correlation coefficient.

The effect of the ice boundary and the mesodomain on PAD dynamics is also manifested in the lowering of $T_{II/III}$ with increased % v/v DMSO. The PAD undergoes an order-disorder transition at a higher T value than the mesodomain (none observed) under all conditions, which is attributed to its protein-organized, quasi-structured hydration water layer, and exclusion of the fluidizing DMSO cosolvent. [138] At 0.5% v/v DMSO, the propagation of the ice boundary confinement effect through the relatively thin mesodomain leads to the higher $T_{II/III}$

value of 215 K (Table 3.1; Region II/III transition, Figure 3.6). As V_{meso} increases, the replacement of the ice boundary restrictive confinement effect by the fluidizing effect of the mesodomain lowers $T_{II/III}$ to 200 K, at 4.0% v/v DMSO.

3.4.7 Dependence of mesodomain solvent dynamics on PAD solidification

Solvent dynamics in the fluid mesodomain respond to PAD solidification. The $\log\tau_{c,f}$ versus $1/T$ dependences show a kink at $T_{II/III}$ for 0.5, 2.0 and 4.0% v/v DMSO (Figure 3.2, D-F), that is followed by a concave-up deviation of the T-dependence of $\log\tau_{c,f}$ at $T < T_{II/III}$, relative to the dependence extrapolated from Region III. Similarly, the T-dependence of $\log\tau_{c,f}$ for +EAL displays a concave-up deviation from $\log\tau_c$ for the –EAL condition, at $T \leq T_{II/III}$ (Figure 3.4). These effects indicate that the arrest of PAD solvent dynamics at $T_{II/III}$ influences the mesodomain dynamics (Figure 3.6). The acuteness of the kinks, and degrees of deviation from the Region III T-dependence, are diminished as % v/v DMSO increases. This is caused, at least in part, by the increase in mean displacement of TEMPOL from the protein and ice boundaries, as the mesodomain volume increases (Figure 3.6). The influence of PAD solidification on the mesodomain thus decreases with increasing distance from the PAD-mesodomain interface.

3.5 CONCLUSIONS

The model for the structure and dynamical properties of the protein-PAD-mesodomain-ice system as a function of added DMSO and T is presented in Figure 3.6. The following sections describe the overall conclusions from the study of a fully-hydrated protein (EAL) in solution, under conditions where an outer-boundary (ice) confinement effect is tuned from strong to negligible by increasing volume of a mesodomain (aqueous-DMSO), in the context of findings from other protein-solvent coupling systems.

Role of confinement effects in determining measured solvent dynamics around proteins

The role of confinement by the ice boundary in dictating the PAD dynamics at low % v/v DMSO, and the decay of the ice-confinement to a free-fluid effect, are dramatic and highlight the strong interplay of dynamical effects among the ice, bulk, PAD and protein. Spectroscopic and scattering measurements, [44,50,51,140] that have provided key insights into protein dynamics and coupled solvent dynamics, are performed on proteins in a hydrated powder state. At the highest hydration levels, percolation of protein surface-associated water is achieved, [50] but the mean layer widths are < 1 water molecules. Increasing disorder at a surface generally decreases its confinement-ordering effect, with a free surface representing a limit. [134, 141] The variation of the T-value of the "protein dynamical transition" [130] over the observed wide range (e.g., $\sim$ 180-240 K) [142] may originate,

at least in part, from different confinement effects, from different compositions or T-dependent fluidities of the outer-boundary phase apposed to the hydration layer-protein system.

Energetics and transmission of bulk solvent collective fluctuations through the PAD

It has been proposed that collective motions of protein groups (multiple atoms, non-local) are driven by translational diffusion of bulk-solvent domains associated with the class of α-fluctuations. [44] Thus, solvent-driving of protein collective motions requires transmission through the PAD or hydration layer, and therefore, a responsivity of the PAD. Our results show a hallmark of this model, [44] for the general case of coupling between distinguishable phases: the slopes of plots of $\log\tau_{c,s}$ (PAD) and $\log\tau_{c,f}$ (mesodomain) versus $1/T$ are comparable for the 4% v/v condition. Microscopically, the comparable mean energy barriers (E^*) of the detected configuration changes in PAD and mesodomain suggest that the solvent in the thin PAD is structured by the mesodomain solvent distribution, effectively extending the mesodomain structure into the PAD (along a subset of coordinates, as described below). Hence, the energetics associated with collective solvent configurational changes are comparable for PAD and mesodomain, and the fluid PAD is capable of transmitting bulk solvent collective motions to the protein with fidelity, along a subset of the collective configuration coordinates.

Protein dynamics are distinct from solvent dynamics

In TEMPOL spin probe measurements, protein structure and dynamical properties must be detected, indirectly, as an influence of the protein surface on the PAD. The statistically-significant, uniform vertical shift of the $\log\tau_{c,s}$ and $\log\tau_{c,f}$ versus $1/T$ relations for 4% v/v DMSO over the measurement range of 205-245 K (Figure 3.7) represents a difference in time-prefactor, $\tau_{c,0}$ (Eq. 3.4.8). The value of $\tau_{c,0}$ scales with the inverse of the activation entropy, and therefore, with the inverse of the number of configurations accessible for configurational change. [44] The lower position of the $\log\tau_{c,s}$ relation in Figure 3.7, indicates fewer accessbile configurations for configurational change, and therefore, more solvent order, in the PAD relative to the mesodomain.

The dominant detected impact of the protein on the solvent dynamics in the PAD is on $\tau_{c,0}$, because the energy barrier heights (E^*) for solvent configuration change in PAD and mesodomain are the same, to within one standard deviation. The shift from $\log\tau_{c,s}$ to $\log\tau_{c,f}$ relations in the T-range of Figure 3.7 is equivalent to a factor of 2.0 $\pm$ 0.3. Therefore, under control of the protein, the PAD "filters" the collective fluctuation input of the bulk solvent. Prohibitive barriers (>1.4 kcal/mol, relative to the measured mean barrier) to collective motion of solvent in the PAD exist along a subset of the PAD configuration coordinates. These coordinates are therefore not detected. In a simple, geometric interpretation, the high-barrier channels for collective solvent rearrangement in the PAD might be oriented transverse to the protein surface. Such a PAD filtering would polarize the directionality of the bulk-solvent, α-fluctuation that drive protein collec-

tive motions. Overall, the reduction in dimension of configurational coordinates caused by the protein surface confinement effect on the PAD solvent indicates that the protein is a dynamically unique medium.

Dynamical transition in the PAD, and temperature-dependence arising from outer boundary confinement effects

TEMPOL exclusion from the PAD at $T_{II/III}$ in the direction of decreasing T suggests that the PAD undergoes a significant change in structure, which can be described most generally as a disorder-to-order (order-disorder) transition. The exterior confinement effect on the PAD dynamics from the ice boundary, acting through the fluid mesodomain, increases the value of $T_{II/III}$. The specification of the transition is independent of a technique bandwidth limitation. [143] Therefore, our results indicate a well-defined, short T-range transition in the configurational dynamics of the hydration water (PAD), that occurs in the range of 200 to 215 K, depending upon the confinement effects of the surround. The order-disorder transition in the PAD of EAL at $T_{II/III}$ lies in the T-region associated with the "protein dynamical transition", or "protein glass transition", in other protein systems. [130,142] The contributions of EAL protein-PAD coupling to the $T_{II/III}$ transition will be addressed by monitoring the dynamics of protein-bound EPR spin labels as described in Chapter 4 [144]

Chapter 4

Electron Spin-Labeling of the EutC Subunit in B_{12}-Dependent Ethanolamine Ammonia-Lyase Reveals Dynamics and a Two-State Conformational Equilibrium in the N-terminal, Signal-Sequence-Associated Domain

---

The work presented in this chapter is available at

B. Nforneh, Bovell, A. and Warncke, K., Free Radic. Res, 2018, 52, 3, 307–318.

4.1 INTRODUCTION

The B_{12} (adenosylcobalamin) -dependent ethanolamine ammonia-lyase (EAL; EC 4.3.1.7), [3] is a bacterial enzyme that is involved in gut microbiome homeostasis, [4–6] and in disease conditions caused by pathogenic strains of $Salmonella$ and $E.\ coli$, in humans. [7,8] The EAL oligomer is composed of the EutB (49.4 kDa, $S.\ typhimurium$; β-subunit) and EutC (32.0 kDa, $S.\ typhimurium$; α-subunit) proteins (one active site per EutBEutC) in a $[(EutBEutC)_2]_3$ stoichiometry. [1, 9, 12] EAL catalyzes the conversion of ethanolamine to acetaldehyde and ammonia, and is thought to function under pathogenic conditions with other proteins of the ethanolamine utilization pathway (products of the eut operon), in the Eut bacterial microcompartment (BMC), a sub-cellular organelle. [24,25] Elucidation of the molecular basis of EAL catalysis, and the intracellular trafficking and targeting of EAL to the biomicrocompartment, is a direction for development of therapeutics. Toward this, we have used low-temperature (T=193-250 K), full-spectrum, time-resolved EPR spectroscopy [90] in frozen, globally-polycrystalline aqueous solutions to characterize kinetics and mechanism of individual steps in the EAL catalytic cycle. [83, 93, 96] The native reactivity at cryogenic temperature (T) values is remarkable, because protein functions that require atomic displacements of approximately >1 Å require a fluid state of the surrounding solvent. [44, 46, 52] The origin of the low-T reactivity of EAL is therefore hypothesized to originate from a solvent "mesodomain" in the microscopic region that surrounds the EAL protein. In cryopreservation processes, the protective "mesodomain" is created

by the exclusion of cosolvents from the growing ice crystallite regions during sample freezing. [53–55] For the cosolvent, dimethylsulfoxide (DMSO), [116] this condition is met for proportions of <30% v/v. [117,118] The increased concentration of cosolvent at the interstitial, ice crystallite grain boundaries in the relatively low-volume mesodomain, leads to depression of the liquid/solid transition T, and formation of supercooled fluid and eventual glassy solid phases with decreasing T, in the mesodomain. [53–55] Here, we address the T-dependence of the solvent liquid-solid state around EAL from $S.\ typimurium$ over 200-265 K, from the vantage of an electron spin label on the protein surface, by using spin label EPR spectroscopy in frozen, polycrystalline aqueous water-only and 1% v/v DMSO solutions.

The technique of site-directed spin-labeling (SDSL) of proteins involves replacement of a selected amino acid with cysteine (Cys, C) by using protein mutagenesis techniques, followed by covalent modification of the substituted Cys side chain by a sulfhydryl-specific molecule that carries an electron spin (S= $\frac{1}{2}$), the spin label. [104, 106, 145] Development and classical applications of SDSL were performed in proteins with native Cys-devoid or Cys-sparse backgrounds. [99,146] In contrast, spin labelling studies of wild-type (wt) proteins (WTSL) are typically fraught with multiple Cys labeling sites, which give a heterogeneous distribution of label, and consequent poor spectral resolution of individual sites. In order to achieve site-specificity in WTSL, one Cys site must be exceptionally accessible to reaction with the spin label, relative to other, partially-accessible and buried Cys sites. The subsequent identification of the spin-labeled site by incre-

mental mutagenesis to replace the Cys sites with an unreactive amino acid, must incur minimal perturbations of the protein fold, that might alter the accessibility of sites, relative to the native state.

Here, we describe the application of WTSL to wt EAL from $S.\ typhimurium$, by using the sulfhydryl-specific, 4-maleimido-TEMPO (4MT) spin label, at a stoichiometry of 1 spin label per active site. EAL presents a challenge to EPR spin-labeling approaches, because there are 16 Cys residues in each EutBEutC unit (16 per active site; $S.\ typhimurium$). [12] As required for successful application of WTSL, we find that one cysteine residue per EutBEutC displays exceptional reactivity with the 4MT spin label, while other cysteines are effectively buried and inaccessible. EAL structure-based Cys solvent accessiblity predictions [127, 147] guide site- directed Cys to alanine (Ala, A) mutations, and room-T EPR studies, that locate the labeled residue in the N-terminal segment of the EutC subunit ($\beta C37$). The N-terminal region of EutC includes a signal sequence, that is involved in intracellular targeting of EAL to the Eut BMC. [148, 149] The T-dependence of the spin label motion in wt EAL over 200-265 K in frozen, polycrystalline water-only and 1% v/v DMSO solvents reveals two mobility components at the labeled site (quantified by τ_c and normalized weight, W, values). The results are interpreted in terms of a two-state model for bound and free association of the EutC N-terminal domain with EAL, and indicate that the persistence of catalysis reactions of EAL [92, 93, 96] and the two-state equilibrium deep into the cryogenic-T regime, are promoted by low-T fluidization of the local solvent region around the EAL protein.

4.2 MATERIAL AND METHODS

4.2.1 Protein preparation

All chemicals were purchased from commercial sources, including DMSO (purity, $\geq$ 99.9%; EMD Chemical), 4-maleimido-TEMPO (4MT, Sigma-Aldrich). Deionized water was used to prepare aqueous solutions (specific conductance, 18.2 M$\Omega.cm$; Nanopure system, Siemens). The wt EAL protein was overexpressed in $E.\ coli$ and purified as described, [9,10] with modifications. [96] Enzyme activity of purified EAL with aminoethanol as substrate was determined at T=298 K and P=1 atm by using the coupled assay with alcohol dehydrogenase and NADH. [18]

4.2.2 EPR sample preparation

Frozen, polycrystalline EPR samples for low-T studies were prepared under aerobic conditions, on ice. A proportion of 1:1 4MT/active sites was added to 20 μM EAL (active site concentration; 120 μM) in 10 mM potassium phosphate buffer (pH 7.5). At 1:1 4MT/active sites, all added 4MT reacts with protein Cys sites (there is no free-solution 4MT EPR spectrum in the samples). Therefore, a procedure to separate unreacted 4MT from the reaction mixture was not necessary. The buffered sample pH is approximately 1.5 units lower than the pK_a of primary amines, and therefore, reaction of 4MT with the free base forms of the N-terminal amino and lysine ε-amino groups was considered negligible. This assumption is

supported by the results of the Cys-to-Ala mutagenesis studies, described below. The reaction of 4MT with EAL Cys sites was rapid (<60 s), on the time scale of the addition of 4MT to the EAL protein samples, mixing, and loading into EPR tubes. EAL was allowed to react with 4MT for 5 min, prior to cryotrapping. The final volume of each sample was 0.3 ml. When present, DMSO was added to 1% v/v in a final volume of 0.3 ml. Samples were loaded into 4 mm outer diameter EPR tubes (Wilmad-LabGlass) and frozen by plunging into T=140 K isopentane solution. This method has a characteristic cooling rate of 10 K/s. [96] Samples were transferred to liquid nitrogen for storage. Room temperature, bulk liquid EPR samples were prepared in 2 mm outer diameter EPR tubes (Wilmad-LabGlass).

4.2.3 Site-directed mutagenesis

Ala was selected for replacement of Cys residues in EAL, following the Ala scanning approach, because Ala displays side-chain space-filling and maintenance protein secondary structure, which minimizes alteration of the native protein fold. [150] The $pBR322$ plasmid including the EutB and EutC genes of wt EAL from $S.\ typhimurium$ (created by L. P. Faust and B. M. Babior [10]; gift of C. B. Grissom, University of Utah) was isolated from single colony growth of wt EAL by using the Plasmid Mini kit (QIAGEN, Hilden, DE). Primers containing the desired mutations (Table F.1 of Appendix 7.2) were used for mutational polymerase chain reaction (PCR) with the QuikChange II XL Site-Directed Mutagenesis Kit, according to the manufacturer's instructions (Strategene, La Jolla, CA, US). The parental EAL plasmid was digested with $DpnI$, and the mutant plas-

mid was transformed into $XL10$ Gold competent cells (Agilent Genomics, Santa Clara, CA, US). Single colonies of the mutant bacteria were grown, and the plasmid extracted for sequencing (Cogenics, UK). Mutation was considered successful when 100% of the desired sequence identity within the EAL reading frame was obtained. Absence of significant protein structural rearrangements was evidenced by successful purification, according to the protocol for wt EAL, without insolubility (improper folding), and by enzyme activity equivalent to wt EAL (Table 4.1).

Table 4.1: Relative solvent accessibility (RSA) of cysteine residues in wt EAL.

Residue	**RSA** [a]
$\alpha C71$	0.140
$\alpha C129$	0.031
$\alpha C159$	0
$\alpha C223$	0.007
$\alpha C249$	0
$\alpha C283$	0.130
$\alpha C361$	0
$\alpha C363$	0
$\alpha C364$	0
$\alpha C388$	0.007
$\beta C37$ [b]	-
$\beta C46$ [b]	-
$\beta C81$	0
$\beta C158$	0.100
$\beta C242$	0
$\beta C260$	0.440

[a] Solvent accessibility calculated by DSSP. [147]

[b] These residues are absent in the X-ray crystallographic structure of $E.\ coli$ EAL, [1] and in the $S.\ typhimurium$ EAL model. [12]

4.2.4 Continuous wave EPR spectroscopy

Continuous wave EPR experiments were performed by using a Bruker E500 ElexSys EPR spectrometer and ER4123SHQE X-band cavity resonator. A Bruker ER4131VT temperature controller and cooling system, based on nitrogen gas flow through a coil immersed in liquid nitrogen, was used to establish T values of 200-265 K. The Bruker ER4131VT temperature readout was calibrated by using a 19180 4-wire RTD probe and Oxford Instruments ITC503 unit, as described. [96] The uncertainty in T values was $\pm$0.5 K. [96] For the low-T measurement protocol, the first EPR spectrum was obtained at T=200 K. The controller was then set to the next higher T-value, and the system was allowed to equilibrate for 5 min at the new T-value. At the end of the 5 min period, the cavity was retuned, and the spectrum was acquired at the new T-value. This procedure was repeated for the entire T range. A baseline sample (all components, but without 4MT) was subjected to the same measurement protocol. Accessory, control experiments were carried out in the direction of decreasing T, starting from 265 K. No hysteresis in correlation times or component amplitudes was observed. No hysteresis was also not observed for samples subjected to an additional cycle of storage and measurement. Therefore, equilibrium conditions are established at each T value. EPR acquisition parameters, 200-265 K: Microwave frequency, 9.45 GHz; microwave power, 0.2 mW; magnetic field modulation, 0.2 mT; modulation frequency, 100 kHz; acquisition number, 4-16 spectra at each T value. EPR acquisition parameters, 295 K: Same as for 200-265 K, except microwave frequency, 9.36 GHz; acquisition number, 64 or 100 spectra.

4.2.5 Continuous wave EPR simulations

Simulations of the cw-EPR spectra were performed by using the program, EasySpin. [121] Convergence of simulations was defined by the default, least-squares fitting criteria. The following established [115] set of parameters was used: principal values of the g tensor, g_x = 2.0120, g_y= 2.0130, g_z = 2.0073; principal values of the ^{14}N hyperfine tensor, A_x = 20.9, A_y = 19.82, A_z = 103.2 MHz. A simple model of random rotational motion about the three Cartesian axes was assumed. Spectra were corrected by subtraction of a baseline sample spectrum (EAL, no 4MT), collected at the same temperature, prior to simulation. Simulations of the experimental spectra required two components, and were performed by variation of the correlation times and normalized weights for the slow-motional ($\tau_{c,s}$, W_s) and fast-motional ($\tau_{c,f}$, W_f) components, and the corresponding intrinsic line widths (Gaussian line width, $\geq$0.02 mT full width at half maximum). The two-component simulation procedure was initiated by using the best-fit parameters from an preliminary one-component simulation as input values for the fast-motional component. This was followed by three iterations of fixing τ_c, W, and intrinsic line width of one component, while the other component's parameters were varied, and a fifth iteration with simultaneous variation of τ_c, W, and intrinsic line width of both components. This derivative-mode spectrum simulation procedure provides rapid convergence to the correct region of the parameter space. The following final steps in the two-component simulations were performed to assure that the slow-motional, broader-line component was correctly represented, particularly for spectra in which the slow component was present in

small proportion. The best-fit parameters from the two-component, derivative-mode simulations were used as starting parameters for an absorption-mode EPR simulation of the integrated experimental derivative EPR spectrum. In the first iteration, the slow component correlation time, $\tau_{c,s}$, was fixed, and all other adjustable parameters were varied. A scan of $\tau_{c,s}$ about the above fixed value was performed at up to six increments of ± 0.1 of the value of $\log(\tau_{c,s})$, and the $\tau_{c,s}$ value that gave the best match to the slow component was identified. This final $\tau_{c,s}$ value was then fixed, and $\log(\tau_{c,f})$ was varied by ± 0.1, to obtain the final $\tau_{c,f}$ value.

4.2.6 Criteria for detection of spin label motion

The characteristic 4MT spectrum arises from interaction of the unpaired electron spin ($S = \frac{1}{2}$) with the nitroxide ^{14}N nuclear spin ($I = 1$), which produces three dominant spectral features that correspond to electron spin-spin transitions ($\triangle m_s = \pm\frac{1}{2}$) among $m_I = 0, \pm 1$ energy levels created by the electron-nuclear hyperfine interaction. [90] The time-dependent reorientation of the spin label leads to averaging of the unpaired electron-^{14}N dipolar hyperfine interaction in the nitroxide spin label, and a consequent narrowing of the EPR line shape, [90] which is quantified by the τ_c value obtained from spectral simulations. The X-band, cw-EPR spin probe approach is sensitive to 4MT reorientational motion in the τ_c range of $\sim 10^{-11}$ (rapid reorientation limit) to 10^{-7} s (defined as the rigid limit). [109] Thus, the inverse bandwidth of mobility detection is defined as $10^{-11} \leq \tau_c \leq 10^{-7}$ s.

4.3 RESULTS

4.3.1 Accessibility of cysteines in wt EAL

The solvent accessibility of Cys residues in wt EAL was estimated, in order to efficiently identify the most probable sites of 4MT spin label attachment, among the 16 Cys residues per active site (16 per EutBEutC). [12] The accessibility of cysteines in the $S.\ typhimurium\ wt$ EAL structure [12] was assessed by using the Accessible Surface Area web server (ASAview), [127] which uses the algorithm, Define Secondary Structure of Proteins (DSSP), [147] to calculate the the relative surface area (RSA) of the residue (area accessible to solvent in the protein, scaled by the total accessible surface area). The standard criterion of RSA>0.2 [151–154] was applied to identify accessible cysteine sites. The RSA values for each cysteine residue in wt EAL (Table 4.1), predict that 1 site is accessible ($\beta C260$), and 13 are inaccessible (buried). The $\beta C260$ side chain lies within the buried active site region of wt EAL, where it makes van der Waals contact with the AdoCbl cofacter in the holoenzyme. [12] The accessible area calculated for $\beta C260$ corresponds to the active site cavity, which the EAL structure shows is accessible by the water-equivalent sphere used for calculation in DSSP, [147] but not to bulky molecules, such as 4MT. Therefore, we conclude that that $\beta C260$ is not a primary site of 4MT reaction. The two residues without RSA values in Table 4.1, $\beta C37$ and $\beta C46$, are part of the N-terminal sequence of EutC, that is not present in the X-ray crystallographic structure of $E.\ coli$ EAL (deletion up to residue 44 was necessary to achieve conditions conducive to EAL crystallization), [1, 155] or in

the $S.\ typhimurium$ EAL model. [12] We thus provisionally consider $\beta C37$ and $\beta C46$ to be accessible to reaction with 4MT.

4.3.2 Identification of the 4MT labeling site in wt EAL

To experimentally identify the primary labeling site in wt EAL, site-directed mutagenesis was used to substitute Ala for the two candidate accessible Cys residues, $\beta C37$ and $\beta C46$. [150] Steady-state enzyme activity parameters for the $\beta C37A$ and $\beta C46A$ EAL were measured, as an assessment of native protein structure in the mutants. Table 4.2 shows that $\beta C37A$ and $\beta C46A$ EAL have k_{cat} and K_M values that are the same, within uncertainty, as for wt EAL. The absence of an effect on enzyme activity parameters is consistent with an accessible, protein surface location of $\beta C37$ and $\beta C46$, and a significant distance from the active site. The zero enzyme activity of the $\beta C260A$ mutation is consistent with the buried, active site location of $\beta C260$.

The EAL single-site mutants, $\beta C37A$ and $\beta C46A$ were analyzed by using 4MT spin labeling and EPR spectroscopy, performed at 295 K. The product of the reaction of wt EAL with 4MT, added at a stoichiometry of one 4MT per active site, shows a line shape characteristic of a relatively mobile species (Figure 4.1). If a mutated cysteine site corresponds to a 4MT attachment site, then the EPR spectrum of the mutant protein should be altered significantly, and present a broader line shape, characteristic of a low-mobility species. This is because, deprived of the accessible cysteine site by mutation to alanine, 4MT would react with one or more of the less accessible sites, which are more deeply buried. The sterically-

restricted spin label motion at the buried site would display a broadened EPR line shape.

Table 4.2: Steady-state enzyme kinetic and EPR simulation parameters for wild-type and mutant EAL.[a]

EAL	k_{cat} **(s^{-1})**	K_M **(μM)**	**Log[$\tau_{c,s}$] (s)**	**Log[$\tau_{c,f}$] (s)**	W_s	W_f	**RMSD**[b]
WT	21.8±7.1	31.4±5.7	-8.37	-9.18	0.32	0.68	0 .01913
$\beta C37A$	22.1±1.1	33.2	-8.10	-9.01	0.71	0.29	0.3441
$\beta C46A$	21.7±2.9	35.8 ±4.5	-8.25	-9.26	0.59	0.41	0.01956
$\beta C260A$	0	–	–	–	–	–	–

[a]Steady-state enzyme kinetics parameters: catalytic constant, k_{cat}; Michaelis constant, K_M. Simulation parameters: reorientational correlation time, τ_c; normalized component weight, W.
[b]RMSD, root mean square deviation of fit of simulated EPR spectrum to experimental EPR spectrum.

Figure 4.1 shows that the EPR line shape of $\beta C46A$ EAL is comparable to wt EAL, which suggests that $\beta C46A$ is not the site of 4MT reaction. In contrast, the EPR line shape of $\beta C37A$ EAL is significantly altered, relative to wt EAL, suggesting that $\beta C37A$ is the primary site of 4MT reaction. These conclusions are quantified by simulations of the EPR spectra. As shown by the overlaid simulated spectra (Figure 4.1) and parameter values (Table 4.2), the wt EAL spectrum is well-fit by a two-component simulation, with relatively short (fast motion) τ_c values for both components. As demonstrated by the low-T results in following sections, these two mobility components correspond to a single reaction site on

wt EAL. The $\beta C46A$ mutant spectrum is also fit by a two-component simulation, with τ_c and W values comparable to wt EAL. In contrast, the simulation of the spectrum from $\beta C37A$ EAL requires a dominant slow-motional component, consistent with 4MT reaction at one or more lower-accessibility, buried sites. The minor faster-motion component in the $\beta C37A$ EAL spectrum may arise from increased probability of reaction at $\beta C46A$, in the absence of $\beta C37A$, or an enhancement of Cys accessibility in a sub-population of EAL, owing to destabilization of the fold by 4MT reaction at one or more buried sites. In summary, based on predictions of the RSA values, enzyme activity parameters, and EPR line shape analysis of 4MT-labeled wt and mutant proteins, we conclude that $\beta C37A$ is accessible, and that it is the primary site of 4MT reaction in wt EAL.

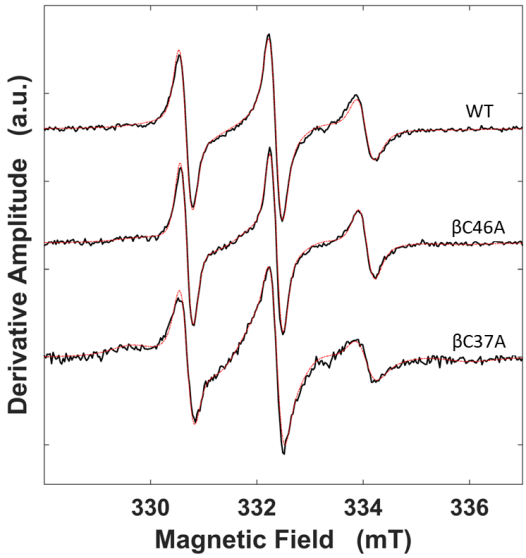

Figure 4.1: EPR spectra of 4MT spin-labeled wild-type and mutant EAL, acquired at 295 K. The spectra are normalized to the central peak-to-trough amplitude, to illustrate the differences in line shape. The normalized spin counts for each spectrum, which represent the double-integral of the presented absorption-derivative spectra, are: 1.0 (WT), 0.9 ($\beta C46A$), 0.6 ($\beta C37A$).

4.3.3 Temperature dependence of the 4MT-labeled EAL EPR line shape in frozen aqueous solution, in the absence of DMSO

The effect of temperature on the EPR line shape of the 4MT spin label in wt EAL at different representative T-values from the complete addressed range of 200-265 K is shown for the 0% DMSO sample in Figure 4.2A. From 200–240 K, the spectra show the rigid-limit, powder pattern line shape. At T>240 K, narrowing of the

overall spectral line width and individual features indicates the commencement of detectable ($\log\tau_c \leq -7.0$) 4MT motion, which results in further line narrowing as T is increased.

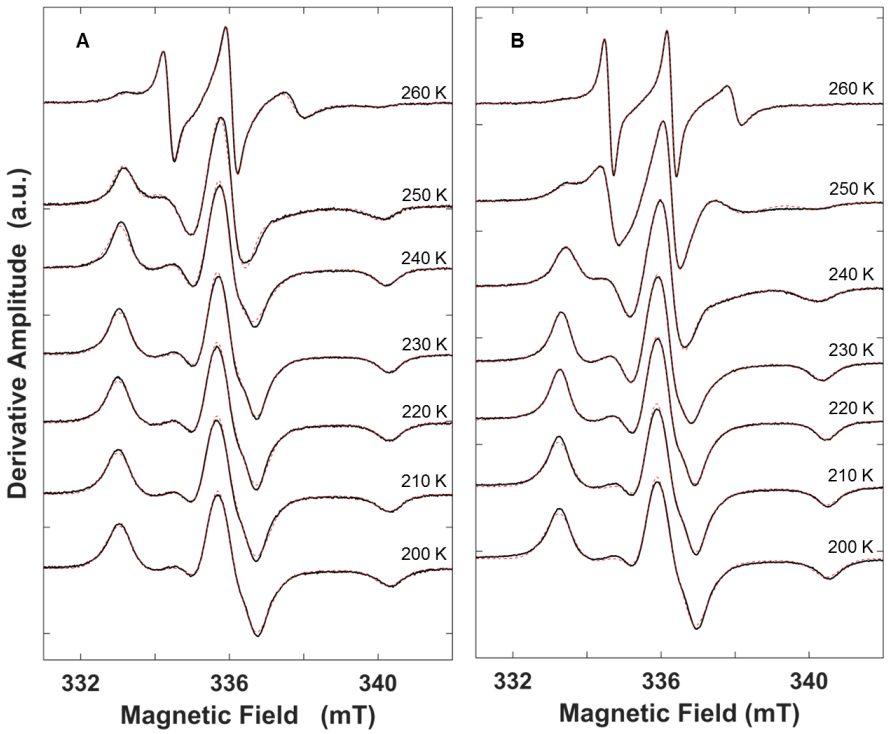

Figure 4.2: Temperature dependence of the 4MT-labeled EAL EPR spectrum (black) and overlaid EPR simulations (dashed red lines). (A) EAL in frozen aqueous solution, 0% DMSO. (B) EAL in frozen aqueous solution containing 1% v/v DMSO. The spectra are normalized to the central peak-to-trough amplitude. Alignment along the magnetic field axis corresponds to the microwave frequency at 200 K.

4.3.4 Temperature dependence of the 4MT-labeled EAL EPR line shape in frozen aqueous solution with 1% v/v DMSO

Figure 4.2B shows the EPR line shape of frozen aqueous solutions of 4MT-labeled wt EAL with added 1% v/v DMSO at representative T-values. The rigid-limit, powder pattern line shape is observed for $T \leq$230 K. The overall line width and widths of the hyperfine features narrow at T>230 K, and this trend continues with increasing temperature. Comparing the line shapes in Figure 4.2 shows that tumbling motion of 4MT in 1% v/v added DMSO is activated at 20-30 K lower in temperature, relative to the 0% DMSO sample.

4.3.5 Temperature dependence of the 4MT-labeled EAL rotational correlation time and normalized component weights in frozen aqueous solution, in the absence of DMSO

Simulations of the EPR spectra were performed in order to quantify the mobility of 4MT on EAL, in terms of the τ_c and W parameters. The temperature dependence of τ_c in EAL, 0% DMSO displays two-component behavior (Figure 4.3A; values, Table G.1 of Appendix 7.2), and is divided into three regions: Region I (200<T<230 K): The logτ_c values lie above the tumbling detection criterion. Region II (230$\leq$T<240 K): A fast-tumbling population is present, with log$\tau_{c,f}$ decreasing with T, along with a rigid population. Region III (240$\leq T \leq$265 K): Both fast- and slow-tumbling populations are present, with log$\tau_{c,f}$, log$\tau_{c,s}$<–7.0, and

decreasing with T. Figure 4.3B shows that there is trend of decreasing dominant slow population component (W_s) with a compensating increase in fast population component (W_f) in region III.

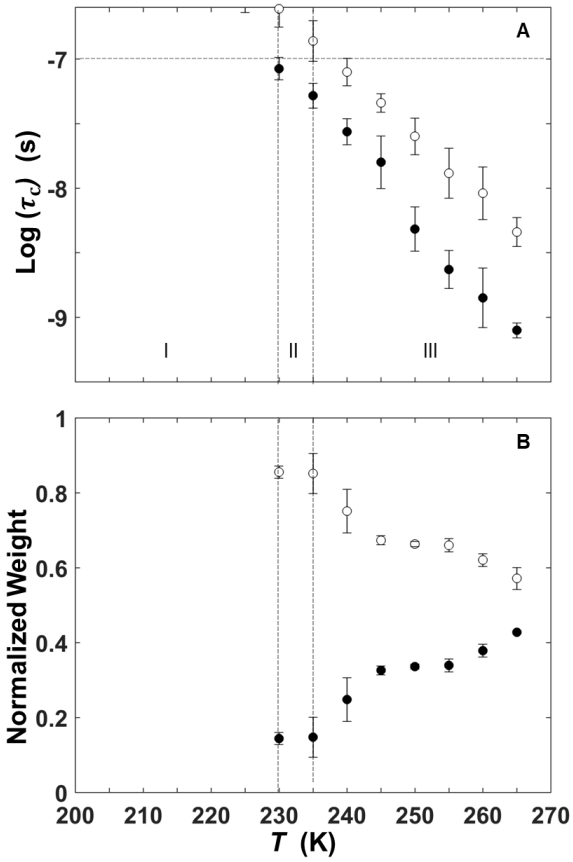

Figure 4.3: Temperature dependence of the rotational correlation time of 4MT-label on wt EAL and normalized mobility component weights, for the water-only, 0% DMSO condition. (A) Rotational correlation time. (B) Normalized weights. Solid circles: fast component; open circles, slow component. Error bars represent standard deviations for three separate determinations.

4.3.6 Temperature dependence of the 4MT-labeled EAL rotational correlation time and normalized component weights in frozen aqueous solution with 1% v/v DMSO

The temperature dependence of τ_c for 4MT in EAL with 1% v/v added DMSO displays two-component behavior over the full T range (Figure 4.4; values, Table G.2 of Appendix 7.2). Three regions of motional behavior are observed, as for the 0% DMSO condition, but the boundary T values are lower by 20-30 K. The dependence of logτ_c on T is divided into three regions (Figure 4.4A): Region I (200<T $\leq$210 K): The logτ_c values lie above the motion detection criterion. Region II (215<T<225 K): A fast-tumbling population is present with decreasing log$\tau_{c,f}$, along with a relatively rigid population. Region III (225$\leq$ T $\leq$265 K): Both fast- and slow-tumbling populations are present, with logτ_c values that decrease with T. In Region III, Figure 4.4B shows that there is a trend of decreasing in Ws with increasing T, with a compensating increase in W_f.

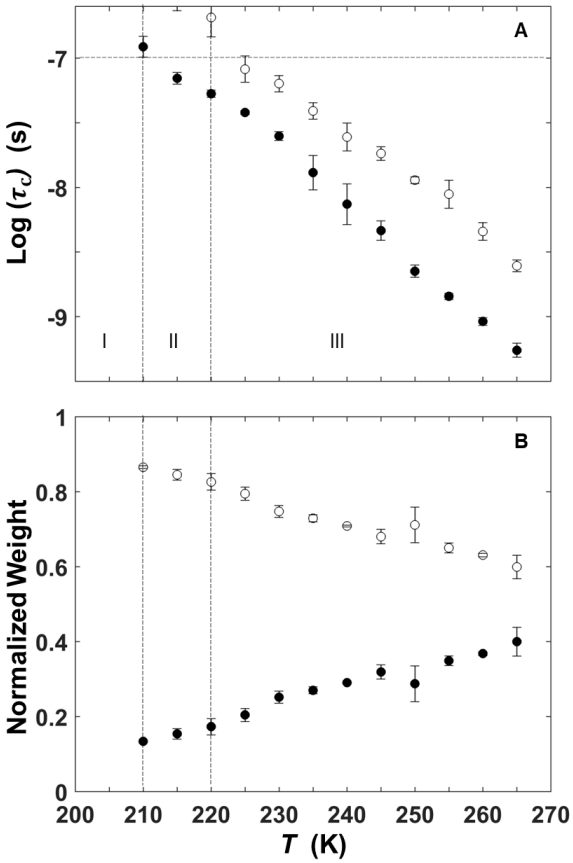

Figure 4.4: Temperature dependence of the rotational correlation time of the 4MT on wt EAL and normalized mobility component weights, for the 1% v/v DMSO condition. (A) Rotational correlation time. (B) Normalized weights. Solid circles: fast component; open circles, slow component. Error bars represent standard deviations for three separate determinations.

4.4 DISCUSSION

4.4.1 Nature of the primary $\beta C37$ spin-labeling site in wt EAL

The study of proteins that contain multiple cysteines by the technique of electron spin-labeling is challenged by the loss of single-site resolution. Buried cysteine residues have small individual probabilities for SL attachment, relative to exposed, surface cysteine sites, but the summed probabilities of multiple buried sites can combine to collectively recruit spin label. Multiple buried sites create a background, lower-mobility spin label line shape in EPR spectra, that can interfere with spectral resolution of the desired spin label site. The challenge is overcome in spin-labeling studies of wt EAL from $S.\ typhimurium$ by the exceptionally high reactivity of a single residue, $\beta C37$. The high reactivity of $\beta C37$ is attributed to its location in the N-terminal polypeptide segment of the EutC subunit. [12] Amino acids 1-19 of the N-terminus of EutC have been identified as a signal sequence for intracellular targeting of EAL to the Eut BMC. [39, 40] Signal sequences require flexible, or disordered regions for protein-target recognition and mooring. A partially unbound or unstructured state of the N-terminus of EutC is consistent with rapid trypsinization of $E.\ coli$ EutC in the EAL oligomer, [155] the requirement for N-terminal deletion up to residue 44 in $E.\ coli$, to eliminate insolubility and achieve crystallization of EAL, [1] and the calculated high protein Instability Index of 51.4 for $S.\ typhimurium$ EutC (Instability Index>40 connotes high instability; the index for EutB is 27.0). [156] The high reactivity of $\beta C37$ with 4MT in wt EAL is consistent with these previous results, and suggests

that $\beta C37$ lies in a dynamic region, which dramatically enhances the accessibility of its side chain –SH function to 4MT.

The $\beta C37$ spin label site provides a probe of equilibrium states and conformational fluctuations of the EutC N-terminus. As described previously, $\beta C37$ is not present in the $S.\ typhimurum$ EAL model. [12] Therefore, preliminary modeling studies were performed to delimit the possible $\beta C37$ backbone C_α position, in the context of the folded $[EutCEutB]_2$ homodimer unit in the EAL oligomer. In the fully-extended conformation of the N-terminal polypeptide, $\beta C37$ is positioned 32 Å from the first modeled residue in the $S.\ typhimurium$ EAL structure, $\beta A47$. Figure 4.5 depicts this upper-limit range of 32 Å for $\beta C37$ displacement from $\beta A47$. The $\beta C37$ residue is associated principally with the surface of the EutB subunit. Electron spin-spin distance measurements, performed by using $\beta C37$-4MT interactions with SDSL-generated sites, as well as interactions of $\beta C37$–4MT with the intrinsic paramagnets in EAL [$S = \frac{1}{2} Co(II)$ in the cobalamin cofactor, substrate radical], [68] in concert with computational approaches, [100, 157, 158] will be used to refine the location of the $\beta C37$ side chain in EAL.

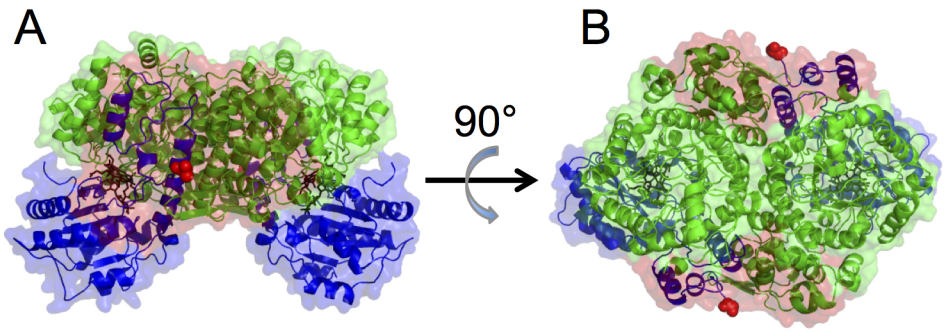

Figure 4.5: Structure showing possible positions of EutC residue, $\beta C37$, in the $S.$ $typhimurium$ EAL model. [2] The cartoon structure of the EutB (green) and EutC (blue), $[EutBEutC]_2$ dimer is shown in two orientations, A and B, related by a $90°$ rotation about the horizontal. The position of the EutC N-terminus at $\beta A47$ is shown as a red sphere in each EutC subunit. The upper-limit range of possible positions of $\beta C37$, assuming a fully-extended (32 Å) polypeptide chain, are shown as a red surface. The protein was modeled by using PyMOL (Schrödinger).

4.4.2 Two-state model for 4MT mobility in EAL in frozen solution in the absence and presence of DMSO (0 and 1% v/v DMSO)

In the frozen aqueous system in the absence of DMSO, 4MT displays two mobility components at all T values (Figure 4.3, Table G.1 of Appendix 7.2). The $\log\tau_c$

values of both the relatively fast-motional and slow-motional components are present in the detection window at 240 K. Both $\log\tau_{c,s}$ and $\log\tau_{c,f}$ subsequently display a continuous, uniformly-decreasing dependence on T, in concert with compensatory changes in W_s and W_f. This suggests that the $\log\tau_{c,s}$ and $\log\tau_{c,f}$ values represent spin label motion within the same microscopic regions, over the full T-range. Figure 4 shows that $\log\tau_{c,s}$, $\log\tau_{c,f}$ and W_s, W_f for the 1% v/v DMSO condition display the same trends as for 0% DMSO: The $\log\tau_{c,f}$ value enters the detection window at 215 K, and $\log\tau_{c,s}$ enters at 225 K, followed by a continuous, uniformly-decreasing dependence of each parameter on increasing T, with compensatory changes in W_s and W_f. Therefore, we propose a two-state model for both the water-only and aqueous-DMSO systems, with states, $S_{s,w}$, $S_{f,w}$ (subscript "w" denotes the water only, 0% DMSO condition), and $S_{s,d}$, $S_{f,d}$ (subscript "d" denotes the 1% v/v DMSO condition), that correspond to the slow- and fast-motional components of the 4MT label at the $\beta C37$ site.

The uniformly lower values of $\log\tau_{c,s}$ and $\log\tau_{c,f}$ for the 1% DMSO condition relative to 0% DMSO, are consistent with lowering of the T-value of the liquid-solid transition, and the lowering of the liquid-state viscosity, in bulk aqueous solutions that contain high proportions (40-50% v/v) of DMSO. [117,118] Therefore, the results indicate the presence of an aqueous-DMSO mesodomain, that surrounds the EAL protein, within the bulk frozen polycrystalline solution.

4.4.3 Solvent- and temperature-dependence of the populations in the two-state system

The normalized weights, W_s, W_f, that correspond to the states, S_s, S_f, show that the fast-motional component is present at low proportion at the lowest T-values for motion detection: W_f=0.14 in 0% DMSO and W_f=0.13 in 1% DMSO (Figures 4.3, 4.4). Over 245-255 K for 0% DMSO, there is an abrupt, partial conversion of $S_{s,w}$ to $S_{f,w}$, leading to W_f=0.33-0.34, followed by a gradual rise to W_f=0.40 at 265 K. In stark contrast, the W_s, W_f versus T relation for 1% v/v DMSO is continuous, with a uniform trend to increasing W_f values at higher T values, ending with W_f =0.40 at 265 K. The abrupt W_s, W_f interconversion in 0% DMSO suggests the effect of a change in solvent phase, that alters the solvent environment around the $\beta 37C$ site. The smooth T-dependence of W_s, W_f in the 1% v/v DMSO system arises because the aqueous-DMSO mesodomain around the protein is in a fluid state over the entire T-range. We attribute the abrupt change in W_s, W_f over 235-245 K in 0% DMSO to melting of an ice-crystalline domain in the vicinity of the protein. This protein-vicinal ice-crystalline domain is not present in the 1% v/v DMSO system.

4.4.4 Equilibrium between the states, S_s and S_f

The smooth T-dependence of the W_s, W_f values for the 1% DMSO condition over a broad T-range affords van't Hoff analysis of the equilibrium between $S_{s,d}$ and $S_{f,d}$, to determine the thermodynamic parameters. [159] The equilibrium constant

(defined for the direction of $S_{s,d} \rightarrow S_{f,d}$) is described as:

$$K = \frac{W_{f,d}}{W_{s,d}} \tag{4.4.1}$$

The Gibbs free energy ($\triangle G$) and corresponding enthalpy ($\triangle H$) and entropy ($\triangle S$) terms are introduced through the equilibrium expressions, $\triangle G$= $-RT \ln K$ and $\triangle G = \triangle H - T\triangle S$, where R is the gas constant, leading to:

$$\ln K = -\frac{\triangle H}{RT} + \frac{\triangle S}{R} \tag{4.4.2}$$

The $\triangle H$ and $\triangle S$ values, obtained from the slope and intercept of the linear fit of data in the van't Hoff plot in Figure 4.6, are 5.6 kcal/mol and 19.2 cal/mol/K, respectively. Therefore, $S_{f,d}$ has both a higher (more positive) enthalpy and higher entropy, relative to $S_{s,d}$. This corresponds qualitatively to the higher relative mobility of the spin label in $S_{f,d}$, which suggests both "looser" interactions with the site region (larger, more positive $\triangle H$) and increased motional freedom (larger, more positive $\triangle S$). The overall free energy difference between $S_{f,d}$ and $S_{s,d}$ is relatively small over the observed T-range, and favors $S_{s,d}$, but trends towards a more favorable $\triangle G$ for formation of $S_{s,d}$: $\triangle G$ varies from 1.6 to 0.5 kcal/mol from 210 to 265 K.

The W_s and W_f values for the 0 and 1% DMSO conditions become coincident at $T \geq$245 K, above the abrupt mobility transition in the 0% DMSO sample (Tables G.1, G.2 of Appendix 7.2). Therefore, DMSO does not influence the equilibrium free energy difference between the states: K_d=K_w, for $T \geq$245 K. In contrast,

the difference in mobility between the two fast-motional states, $S_{f,d}$, $S_{f,w}$, and difference between the two slow-motional states, $S_{s,d}$, $S_{s,w}$, quantified as ($\log\tau_{c,f,d}$ – $\log\tau_{c,f,w}$) and ($\log\tau_{c,s,d}$ – $\log\tau_{c,s,w}$), is approximately maintained, across the full T-range of detectable SL mobility. Therefore, DMSO influences (enhances) the mobility of SL in both S_s and S_f, which is consistent with the effect of DMSO on the dynamical property of solvent viscosity. Solvent viscosity does not influence the thermodynamic relations between states at equilibrium.

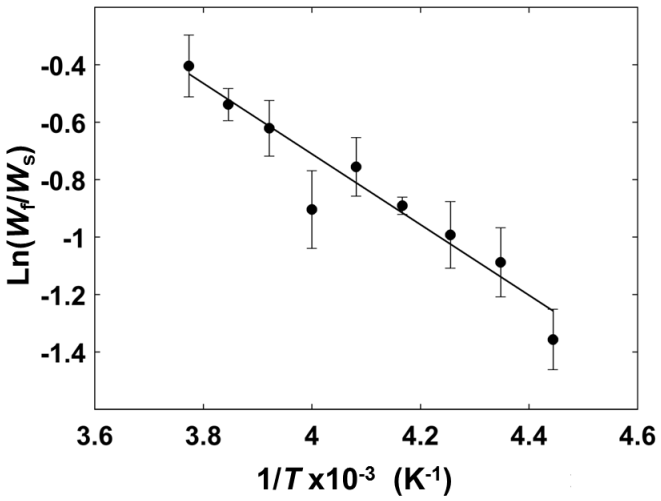

Figure 4.6: Temperature-dependence of the relation of the ratio of fast- and slow-motional component weights in the form of the van't Hoff plot. Solid line is the best-fit linear relatioin (R^2= 0.9113; R is Pearson's correlation coefficient).

4.4.5 Model for the origin and temperature-dependence of the two-state, S_s, S_f system for EAL in 0 and 1% DMSO solution

The model proposed for the origin of the two mobility states at 4MT spin label at the $\beta C37$ site and the T-dependence of the mobilities is presented in Figure 4.7. The model in Figure 4.7 applies to both the 0% and 1% DMSO conditions, but the detailed, microscopic effects of solvent composition on the T-dependence of spin label mobility differ for the two solvent systems. The model incorporates the following prior literature results, that inform on the context of the $\beta C37$ site in the N-terminal domain of the EutC subunit: (1) $\beta C37$ is located in the disordered N-terminal region identified by X-ray crystallographic studies. [1] (2) Rapid trypsinization of the N-terminal domain of EutC indicates a disordered region. [155] (3) The N-terminal region of EutC is part of the signal sequence that targets EAL to the biomicrocompartment [148, 149], which implies a functional requirement for a dissociated state. A dissociated state of the N-terminal region is also suggested by the calculated relatively high Instability Index [156] of the N-terminal region of EutC. The explicit model in Figure 4.7 also incorporates the proposition, that lowered temperature, over the wide range of 265$\rightarrow$200 K sampled here, will reveal the corresponding bound state of the N-terminal domain, because this state is more restricted and, thus, favored by lowered temperature. The explicit model in Figure 4.7 is one of several possible interpretations that could be based on consideration of side chain rotamer states, static pro-

tein environments local to the spin label, possible effects of delocalized protein structure changes, and possible direct effects of protein dynamics. For example, an alternative interpretation is that the two spin label mobility states arise from two different rotamer states, within a static protein environment. The hypothesis that is represented by the explicit model in Figure 4.7, is consistent with the following findings, presented here: (1) the exceptional 4MT-reactivity of the $\beta C37$ site, and (2) the positive sign of the equilibrium entropy change for conversion of S_s to S_f (the sign of $\triangle S$ is not linked to spin label mobility). We will further test the hypothesis and explicit model, by probing for consistent behavior of the temperature-dependent spin label dynamics at genetically-engineered Cys at other sites in the N-terminal domain.

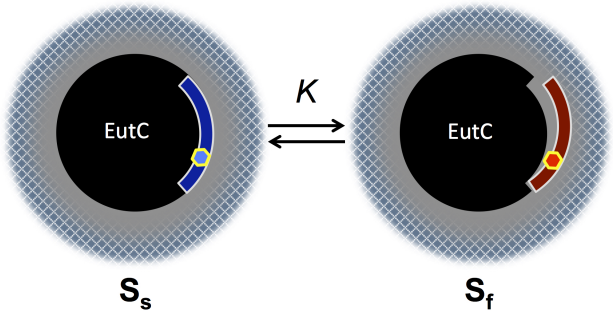

Figure 4.7: Depiction of the two-state model proposed for the origin of the temperature-dependence of the mobility of 4MT spin label in $S.\ typhimurium$ EAL, based on the context of the $\beta C37$ label site in the N-terminal domain of the EutC subunit (black). The 4MT spin label site (hexagon) has two mobility states, W_s (cyan) and W_f (red). The S_s and S_f states correspond to protein-"bound" (left, blue) and relatively loosely-associated, or "free" (right, dark red) conformations of the N-terminal sequence of EutC, respectively. The equilibrium between the two conformations is governed by equilibrium constant, K (K_d, 1% v/v DMSO; K_w, water-only). The grey halo represents the aqueous-DMSO mesodomain around EAL, that maintains the liquid state at cryogenic temperatures, or the side-chain fluidized region vicinal to the protein in the absence of DMSO. Blue hatched regions represent the polycrystalline water-ice domains in the surrounding frozen aqueous solution.

The two spin label mobility states, S_s and S_f, correspond to two conformations of the N-terminal EutC sequence. In S_s, the N-terminal domain is relatively strongly-associated, or "bound," at the protein surface, and in S_f, the domain is

relatively loosely-associated with the protein, or "free." The conformation of the N-terminal domain dictates the motional freedom of the spin label at the $\beta C37$ site. In the bound state, S_s, the spin label experiences a relatively constrained environment, which leads to lower mobility, and in the free state, S_f, the spin label experiences an environment that allows higher mobility. The W_f and W_s spin label mobility populations directly represent the equilibrium thermodynamics of the bound and free N-terminal sequence conformations. The kinetics of S_s – S_f interconversion will be addressed in future work, by monitoring the relaxation of the W_f and W_s populations following T-step perturbation. [96]

The results, interpreted in terms of the model in Figure 4.7, indicate that the EutC N-terminus-bound state is favored over the range of low T values examined. The N-terminus-free state has higher relative entropy, and thus its population grows with increasing T, to a solvent-independent value of 0.4 at 265 K. At 295 K, significant populations of each state are present (Figure 4.1, Table 4.2). This may represent the physiological situation, and a trade-off between EutC and EAL protein stability (N-terminus-bound state), and an efficient stochastic search for the BMC inside the bacterial cell, which requires molecular recognition at the BMC target (N-terminus-free state).

Chapter 5

The Two-State Conformational Equilibrium in the N-terminus of the EutC Subunit of EAL Revealed by using Electron Spin-Labeling is Maintained in Frozen added 0.5, 2 and 4% v/v Dimethylsulfoxide-Water Solution

---

5.1 INTRODUCTION

The EAL together with its cofactor AdoCbl catalyzes the conversion of the substrate ethanolamine to acetaldehyde and ammonia as described in Chapter 4. Both mammalian and bacterial cell walls are rich in phosphatidylethanolamine, which is readily broken down by phosphodiesterases to give ethanolamine. [6,26] Thus, cell wall composition and diet make the intestine an ethanolamine rich environment. The ability to use ethanolamine as the sole source of energy (carbon and nitrogen) confers an advantage for bacterial colonization of the gut. Several pathogenic bacteria, including $Salmonella$, use the ability to metabolize ethanolamine to survive in ethanolamine rich environments such as in foods, and within their hosts. [4–8, 27–31] As a result of this, a strong correlation has been found between food poisoning bacteria and the presence of eut genes. [32] A holistic understanding of the eut pathway and the involvement of EAL in the Eut BMC [24, 25] can lead to drug development that suppress such bacterial proliferation.

As shown in Chapter 2, the remarkable low-temperature, native function of EAL in frozen, polycrystalline aqueous solutions originates from the perpetuation of fluidity of the surrounding medium, [133] which is generally required for native protein function at low temperature. [160] Electron spin label studies on wt EAL further support this, and as reported (Chapter 4), through a combination of solvent accessibility studies of Cys in EAL, site-directed mutagenesis, and SDSL using 4MT, the most probable sites of 4MT spin label attachment, among the 16

Cys residues per active site in wt EAL is $\beta C37$. [144] The high reactivity of $\beta C37$ is attributed to its location in the N-terminal polypeptide segment of the EutC subunit. [12] Amino acids 1-19 of the N-terminus of EutC have been identified as a signal sequence for intracellular targeting of EAL to the Eut BMC. [148,149] Signal sequences require flexible, or disordered regions for protein-target recognition and mooring. The $\beta C37$ spin label site provides a probe of equilibrium states and conformational fluctuations of the EutC N-terminus. This led to the proposed two-state model (Figure 4.7) for the 4MT spin label attachment at the $\beta C37$ residue where the conformation of the N-terminal domain dictates the motional freedom of the spin label at the $\beta C37$ site. As shown in Figure 4.7, a partially unbound, S_f "off" state of the N-terminus of EutC is consistent with $\beta C37$ lying in a dynamic region which increases the motional degree of freedom of the spin label. On the other hand, a bound, S_s "on" state is equally consistent with reduced dynamics of the spin label to ensure protein function and stability.

Here, we extend the two-state model [144] and also expand on the remarkable native reactivity of EAL at cryogenic temperatures by quantitatively describing the T-dependence, over 200-265 K, of the motional freedom of a surface bound spin label on wt EAL from $S.\ typhimurium$ in frozen added 0.5, 2 and 4 % v/v dimethylsulfoxide (DMSO) solution by using cw-EPR. The sulfhydryl-specific, 4-maleimido-TEMPO spin label, at a stoichiometry of 1 spin label per active site is used. Similar to the results in Chapter 4, the T-dependence of the spin label motion in the wt EAL over 200-265 K in frozen added 0.5, 2 and 4% v/v DMSO solvents reveals two mobility components at the labeled site and supports the

previously proposed two-state model for bound and free association of the EutC N-terminal domain with EAL. [144] Furthermore, the results indicate that the dynamics of the two-state, including fluid to solid transitions, can be controlled by T-variation and DMSO addition. This serves as a means to control and isolate individual steps in the catalytic cycle of enzymes such as EAL by using first-order kinetic analysis and other methods [92, 93, 96] in an effort to gain insights into the mechanism of the enzyme action. The results also point to the possible mechanism of the signal sequence function, protein stability and EAL targeting to the Eut BMC.

5.2 MATERIAL AND METHODS

5.2.1 Sample preparation

All chemicals were purchased from commercial sources, including DMSO (purity, $\geq$99.9%; EMD Chemical), 4-maleimido-TEMPO (4MT, Sigma-Aldrich), and deionized water was used (resistivity, 18.2 MΩ.cm; Nanopure system, Siemens). The wt EAL protein from $S.\ typhimurium$ was overexpressed in $E.\ coli$ and purified as described in Chapter 4. Sample for EPR measurements were prepared aerobically as described in Chapter 4. When present, DMSO was added to 0.5, 2, and 4% v/v, respectively in the final volume of 0.3 mL.

5.2.2 Continuous wave EPR spectroscopy

Temperature calibration (T-values from 190-265 K in steps of 5 K) was done by using a Bruker ER4131VT temperature controller and cooling system, based on nitrogen gas flow through a coil immersed in liquid nitrogen and cw-EPR measurements were performed by using a Bruker E500 ElexSys EPR spectrometer and ER4123SHQE X-band cavity resonator as described in Chapter 4. EPR acquisition parameters: Microwave frequency, 9.45 GHz; microwave power, 0.2 mW; magnetic field modulation, 0.2 mT; modulation frequency, 100 kHz; acquisition number, 4-16 spectra were averaged at each T value.

5.2.3 Continuous wave EPR simulations and criteria for detection of spin label motion

Simulations of the cw-EPR spectra were performed by using the Chili algorithm in the program, EasySpin [121] as described in Chapter 4. Briefly, simulations of the experimental spectra required two components, and were performed by variation of the 4MT spin label reorientation correlation times and normalized weights for the slow-motional ($\tau_{c,s}$, W_s) and fast-motional ($\tau_{c,f}$, W_f) components, and the corresponding intrinsic line widths (Gaussian line width, $\geq$0.02 mT full width at half maximum). The convergence of simulations was defined by the default, least-squares fitting criteria. The criteria for detection of spin label motion was similar to that used in Chapter 4: τ_c range of $\approx 10^{-11}$ (rapid reorientation limit) to 10^{-7} s (defined as the rigid limit).

5.3 RESULTS

5.3.1 Temperature dependence of the 4MT-labeled EAL EPR line shape in frozen aqueous solution: 0.5, 2 and 4% v/v DMSO

The effect of temperature on the EPR line shape of the 4MT spin label at different representative temperatures from the complete addressed range of 200-265 K is shown in Figure 5.1 for the 0.5, 2 and 4% v/v DMSO samples. For all % v/v DMSO values, the rigid-limit, powder pattern line shape is observed at the lowest T value, and at the highest T values, narrowing of the electron-nuclear dipolar anisotropy is well-averaged by rapid tumbling, and the overall spectral width approaches twice the value of the ^{14}N isotropic hyperfine coupling constant, $2A_{iso}$=3.4 mT=96 MHz. However, the transition from the powder pattern line shape to a spectrum with narrowing of the spectral width and widths of individual features, which indicates the commencement of detectable ($\log\tau_c \leq$ -7.0) 4MT motion, occurs at different T values that decrease with % v/v DMSO: T>220 K for 0.5, $T \geq$210 K for 2, and T > 205 K for 4 % DMSO. Continuing this trend, the T values at which significant line-narrowing owing to rapid tumbling occur also decrease with % v/v DMSO: $T \geq$260 K for 0.5, $T \geq$250 K for 2 and T>240 K for 4 % v/v DMSO. Therefore, the line shapes in Figure 5.1 qualitatively show that tumbling motion of 4MT in 4% v/v added DMSO is detectably activated at ≈15 K and ≈5 K lower in T, relative to the 0.5 and 2% v/v DMSO solution, respectively, and that the transition to rapid tumbling motion in 4% v/v added DMSO

is detectably activated at ≈20 K and ≈10 K lower in T, relative to the 0.5 and 2% v/v DMSO solution, respectively.

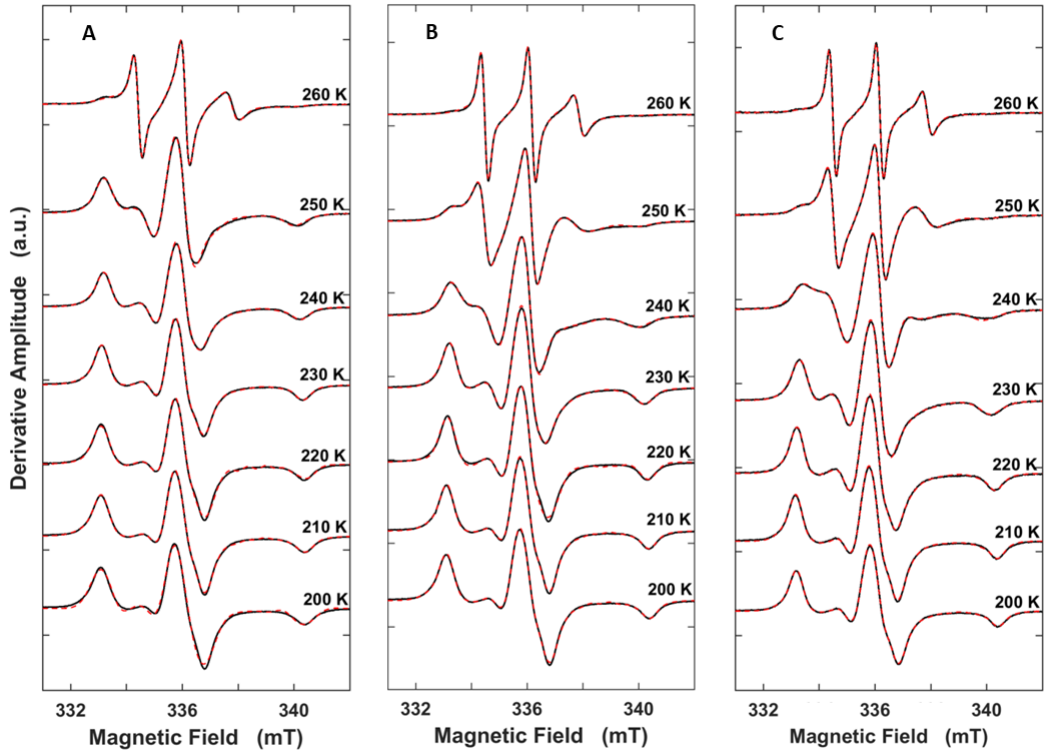

Figure 5.1: Temperature dependence of the 4MT-labeled EAL EPR spectrum (black) and overlaid two-component EPR simulations (dashed red lines). (A) EAL in aqueous solution containing 0.5% v/v DMSO. (B) EAL in in aqueous solution containing 2% v/v DMSO. (C) EAL in in aqueous solution containing 4% v/v DMSO. EAL concentration was 20 μM. The spectra are normalized to the central peak-to-trough amplitude. Alignment along the magnetic field axis corresponds to the microwave frequency at 200 K.

5.3.2 Temperature dependence of the 4MT-labeled EAL rotational correlation times and normalized component weights in frozen aqueous solution with 0.5, 2 and 4% v/v DMSO

The EPR spectra were simulated to quantify the 4MT reorientational motion in terms of the τ_c and normalized W values of the mobility components. The T dependence of τ_c in the 4MT-labeled EAL at 0.5, 2, and 4% v/v DMSO conditions displays two-component behavior, where the two components are characterized by a relatively short τ_c value (denoted as the "fast" tumbling component,$\tau_{c,f}$) and a relatively long τ_c value (denoted as "slow" tumbling component,$\tau_{c,s}$). Figure 5.2 (A, B, C) show a plot of the logτ_c versus T for the three DMSO conditions considered. The values are also given in Table I.1, I.2, and I.3 of Appendix 7.2. The T-dependence is divided into three regions, as follows: Region I: Both logτ_c values lie above the tumbling detection criterion. Region II: A fast-tumbling population is present, with log$\tau_{c,f}$ $\leq$–7.0 and decreasing with T, along with a rigid population (simulated logτ_c>7.0). Region III: Both fast- and slow-tumbling populations are present, with log$\tau_{c,f}$, log$\tau_{c,s}$ continuing to decrease with T. The T value, at which the log$\tau_{c,f}$ and log$\tau_{c,s}$ values meet the criterion for detectable tumbling ($\leq$–7.0), determines the boundary of Region I and II, and decreases with added % v/v DMSO, as shown in Table 5.2.

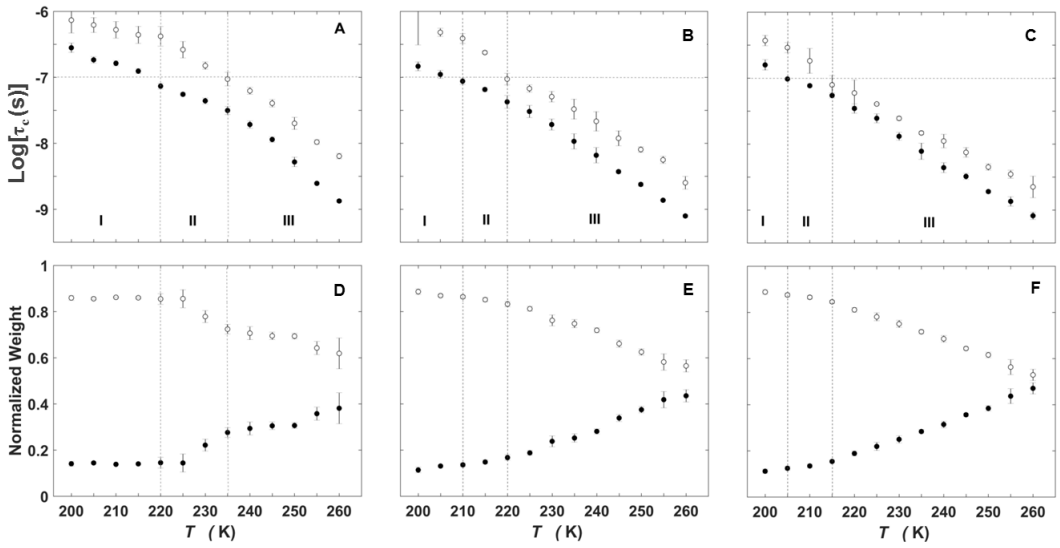

Figure 5.2: Temperature dependence of the rotational correlation time of the 4MT on wt EAL and normalized mobility component weights. Top and bottom panel from left to right: A, D) 0.5% v/v DMSO; B, E) 2% v/v DMSO; C, F) 4% v/v DMSO. Solid circles: fast component; open circles, slow component. Error bars represent standard deviations for three separate determinations.

Figure 5.2 (D, E, F) shows the normalized weight plot versus T for the 0.5, 2 and 4% v/v DMSO condition, respectively. As seen in the figure, for all % v/v DMSO conditions and at all T considered, the normalized weight of the slow component (W_s) has the dominant population when compared to the fast component (W_f). However, in Region III for all the % v/v DMSO conditions, there is trend of decreasing dominant W_s component with a compensating increase in W_f component. The normalized weight values are given in Table I.1, I.2, and I.3 of Appendix 7.2 for the 0.5, 2 and 4% v/v DMSO condition, respectively.

5.4 DISCUSSION

5.4.1 Origin of the 4MT mobility components in the spin-labeled EAL aqueous solution: 0.5, 2 and 4% v/v DMSO systems

As previously reported in Chapter 4, the 16 cysteine residues per active site of EAL pose a huge challenge for specificity of spin label attachment site in the wt EAL. However, we overcome this in 4MT spin-labeling studies of wt EAL from $S.$ $typhimurium$ by identifying residue $\beta C37$ as the primary labeling site due to its location and exceptionally high reactivity. The $\beta C37$ residue is located in the N-terminal polypeptide segment of the EutC subunit, [12] and the amino acids 1-19 of the N-terminus of EutC have been identified as a signal sequence for intracellular targeting of EAL to the Eut BMC. [148,149] The high reactivity of $\beta C37$ with 4MT in wt EAL is thus consistent with the location of the residue and give credence to the reported function of signal sequences for protein-target recognition and mooring.

For the 0.5, 2 and 4% v/v DMSO systems, the previously proposed two-state model, Figure 4.7, is supported as a two-component simulation is used to fit the EPR line shape that is generated from the 4MT spin label bound primarily to the $\beta C37$ residue at all T considered. The two-state conformational model originating from a single spin label anchor position is consistent with: (1) a partially unbound state of the N-terminus of EutC, [1, 155, 156] as a possible mechanism for EAL targeting in to the Eut BMC and (2) a bound state of the N-terminus of

EutC with EAL to ensure protein stability and function.

5.4.2 Confirmation of an existing equilibrium between the states, S_s and S_f in 0.5, 2 and 4% v/v DMSO systems

The smooth T-dependence of the values of W_s (state $\mathbf{S}_s$) and W_f (state $\mathbf{S}_s$) for the 0.5, 2 and 4% v/v DMSO systems in Region III (Figure 5.2) is consistent with the previously reported dependence for the 1% v/v DMSO condition over the same broad T-range (Chapter 4). Application of a van't Hoff type analysis to test the equilibrium between the $\mathbf{S}_s$ and $\mathbf{S}_f$ state, and also to determine the thermodynamic parameters yields more evidence that an equilibrium exists between the two states. Assuming the direction of $\mathbf{S}_s \rightarrow \mathbf{S}_f$, [144] Figure 5.3, shows the van't Hoff plot for all the % DMSO conditions where both $\log\tau_{c,f}$ and $\log\tau_{c,f} \leq$-7 (Region III). The plots are consistent with a van't Hoff type plot and the thermodynamic parameters, $\triangle H$ (enthalpy) and $\triangle S$ (entropy) values, obtained from the slope and intercept of the linear fit of each data is given in Table 5.1. In each condition, the unbound state $\mathbf{S}_f$ has both a more positive enthalpy and higher entropy, relative to bound state $\mathbf{S}_s$. This is consistent with the higher relative mobility of the spin label in the unbound state due to the increased motional degree of freedom as depicted in Figure 4.7.

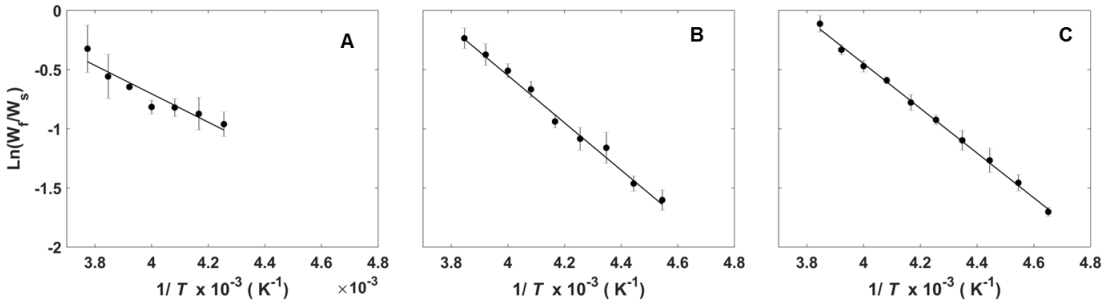

Figure 5.3: Temperature dependence of the relation of the ratio of fast- and slow-motional component weights in the form of the van't Hoff plot. (A). 0.5% v/v DMSO solution. (B). 2% v/v DMSO solution (C). 4% v/v DMSO solution. Error bars represent standard deviations for three separate determinations. Solid line is the best-fit linear relation (R^2= 0.894, 0.9917, 0.9977 for 0.5, 2 and 4% v/v DMSO, respectively; R is Pearson's correlation coefficient).

Table 5.1: Enthalpy and entropy values for the equilibrium between W_s and W_f mobility components.[a]

Sample	**△H (kcal/mol)**	**△H (cal/mol/K)**	$R^{2\ b}$
EAL, 0.5% v/v DMSO	5.5±1.1	18.7±4.4	0.894
EAL, 1% v/v DMSO†	5.6±0.7	19.2±3.0	0.9224
EAL, 2% v/v DMSO	9.4±0.4	34.12±1.4	0.9917
EAL, 4% v/v DMSO	8.6±0.2	32.5±0.7	0.9977

[a]Values correspond to linear fit of van't Hoff plot of data, averaged for each temperature from three separate experiments and derived from W_s, W_f values.

[b] R is Pearson's correlation coefficient.

†previously reported value in Chapter 4

The linear dependences shown in Figure 5.3 indicate that the properties of the system are constant over the respective T-ranges, for each spin label conformation. However, there is a shift in the rigid to mobile transition T towards lower T values, (Table 5.2), with increasing % v/v DMSO. This is consistent with the effect of DMSO on the dynamical property of solvent viscosity.

5.4.3 Temperature dependence of the rigid to mobile dynamic transition and the role of the added DMSO

A common feature of the temperature dependence of the $\log\tau_{c,f}$ and $\log\tau_{c,s}$ values at all % v/v DMSO values in Figure 5.2 is a shift of the curves, including the boundaries of Regions III/II and II/I, to lower T-values, as % v/v DMSO increases. Table 5.2 quantifies the shift by presenting the T-values at the boundary of Region II and III for which the $\log\tau_c$ for each phase is $\leq$-7.0, the window of reliable measurements for the X-band, cw-EPR spectrometer.

The T-dependence of the rigid to mobile dynamic transition has been reported in a similar system (Chapter 6; except that a spin probe was used) and argued to arise from the coupling of the dynamics of the protein associated domain (PAD), and the mesodomain phase. These phases together with the added DMSO, which serves as an antiplasticization agent of the hydration water around the protein at low temperatures, protect the protein conformation and ensures that biological functions are retained subsequent to freezing and thawing. These effects, coupled with: (1) the location of the spin label at the $\beta C37$ residue in the N-terminal

polypeptide segment of the EutC subunit with EAL and (2) the effect of the added DMSO on the dynamical property of solvent viscosity, [117,118] contribute to the observed rigid to mobile dynamic transition as well as to the shift in the T-values to colder temperatures at added % v/v DMSO.

Table 5.2: The temperature value corresponding to the reorientation correlation time for 4MT dynamic motion attached to $\beta C37$ in wt EAL: Case for the onset of log$\tau_c \leq$-7.0.[a]

Sample	S_f**:** T **(K)**	S_s**:** T **(K)**	**Both** S_f **and** S_s **:** T **(K)**
EAL, 0% DMSO[†]	230	240	240
EAL, 0.5% v/v DMSO	220	235	235
EAL, 1% v/v DMSO[†]	215	230	230
EAL, 2% v/v DMSO	210	220	220
EAL, 4% v/v DMSO	205	215	215

[a]The temperature values are from the mean of three separate experiments.

[†]previously reported value in Chapter 4.

The ability to shift the fluid-solid dynamic transition T-values for both phases as shown in Table 5.2 is useful for systems where the control of dynamics is desired. This serves as a means to control and isolate individual steps in the catalytic cycle of enzymes such as EAL [92, 93, 96] by using first-order kinetic analysis. These types of studies provide additional additional insights into the mechanism of enzyme action. This is based on the hypothesis that solvent fluctuations couple with the specific protein fluctuations to drive catalysis in EAL and

other enzymes. The results presented herein are therefore useful in studies that seek to elucidate and couple the effects of the solvent and surface fluctuations to the central reaction kinetics in EAL, and extensible to other enzyme systems. Furthermore, the results give insights to the possible mechanism of the signal sequence function while at the same time shedding light on the interplay between the protein stability and its targeting and trafficking to the Eut BMC. This is a spring box for studies that attempt to understand the possible mechanism of the signal sequence function, protein stability and EAL targeting to the Eut BMC.

Chapter 6

The Effects of added Substrate, Aminoethanol, on the Solvent Dynamics Around the B_{12}-Dependent Ethanolamine Ammonia-Lyase Protein in Frozen Aqueous-Dimethylsulfoxide Solution

6.1 INTRODUCTION AND BACKGROUND

As highlighted in the previous chapters, bulk solvent and surface fluctuations play a crucial role in protein functions. [140, 160–166] The mutual coupling between the PAD and mesodomain fluctuations and their impact on the EAL function is a direction for study. The possible mechanism through which the EAL is able to maintain the central chemical step of radical rearrangement deep into the cryogenic temperature regime ($T \geq$190), in frozen, polycrystalline aqueous solution [92, 93, 95] originates from the mechanism of cryopreservation, where in the presence of cosolvent, a mesodomain phase maintains fluidity and solvent fluctuations sufficient for the observed function of EAL at low temperatures(Chapter 2, 6, and 4). Considering that protein function is influence by the solvent dynamics around the protein [44–49], the modification of the latter gives experimentalists a method to precisely control the solvent dynamics as a tunable parameter in quantifying and investigating the mechanism of coupling between solvent and surface dynamics, and chemical reaction steps in EAL and other enzymes.

The enzyme EAL has one substrate ethanolamine (also called 2-aminoethanol; AmEtOH) and requires the cofactor AdoCbl to catalyze the deamination of ethanolamine into two products; acetaldehyde and ammonia as described in Chapter 1 with Figure 1.3 and Figure 1.4 showing a schematic depiction of the native reaction catalyzed by EAL, and the change in substrate over the steps of the mechanism, respectively. One of the steps in Figure 1.4 involves the formation of the only paramagnetic intermediate species in the cycle; Co(II)-substrate

radical pair. [67–69] This substrate radical intermediate state in the EAL cycle can be trapped (accumulated) in the steady-state at room temperature and then cryotrapped and subsequently allowed to decay by T-steps. [92, 96] The Co(II)-substrate radical pair eventually decays into diamagnetic products in parallel with reformation of the intact cofactor, and the released of the acetaldehyde and ammonia. The decay can be monitored by using time-resolved, full-spectrum EPR spectroscopy. [96] Room T enzyme steady-state kinetic studies have rates that occur on a timescale that far exceeds those of chemical steps. [92] By going down to cryogenic temperatures, the effects of protein fluctuations and the configurational states that they connect on reactions, which are generally difficult to discern at room T, is overcome as these motions can be agitated selectively, so that the reaction rate is impacted. This therefore provides a method to study individual chemical steps in reaction cycles and how perturbations of the environment of the enzyme can affect its reaction chemistry.

Kohne $et\ al$ [92] have isolated and cryotrapped at 140 K the substrate radical intermediate step (Co(II)-substrate radical pair) in the catalytic cycle of EAL and then subsequently triggered T-step (to $T\ \geq$190 K) first-order decay of the substrate radical to the diamagnetic products state. It was found that the low-T kinetics of the Co(II)-substrate radical pair decay process in EAL over 203-230 K are marked by two abrupt changes in Arrhenius dependence with descending T, at 220 K (bifurcation) and 217 K (kinks). The obeservation was attributed to the T-dependence of the free energy landscape which originates from a dependence of the reaction on collective fluctuations in the native reaction regime (220-295 K),

to a dependence on local protein fluctuations in the regime below the transition (203-214 K). To support their argument, it was proposed that the bifurcation and kink transitions represent the effective quenching of two distinct sets of native protein collective configurational fluctuations, that (1) reconfigure the substrate radical pair state and enable it for reaction, and (2) execute the chemical step of rearrangement.

Herein we propose a method, in conjunction with the results from the previous chapters, that can be used to precisely control the solvent and surface dynamics around EAL as a tunable parameter in quantifying and investigating the mechanism of coupling between solvent and surface dynamics, and chemical reaction steps in EAL and other enzymes. Once achieved, the enzyme kinetic measurements that will follow, we hypothesized, will provide unequivocal support to the T-dependent model of the free energy landscape of the substrate radical pair decay. [92] Toward achieving this goal, herein, we quantitatively describe the T-dependence, over 200-265 K, of the mobility of solvent phases that surround EAL in frozen 0 and 2% v/v DMSO solution with the addition of the substrate AmEtOH, albeit without B_{12}, to avoid turnover of enzyme, by using the nitroxide electron spin probe, TEMPOL, and cw-EPR spectroscopy. [90] The results, together with preliminary kinetic measurements with DMSO as a cosolvent, show that the solvent and protein surface dynamics are indeed coupled to the central enzyme reaction. This has open new frontiers to use DMSO as a cosolvent in the kinetic studies of the mechanism of EAL catalysis.

6.2 MATERIAL AND METHODS

6.2.1 Sample preparation

All chemicals were purchased from commercial sources, including DMSO (purity, ≥99.9%; EMD Chemical), and deionized water was used (resistivity, 18.2 MΩ.cm; Nanopure system, Siemens). The EAL protein from $S.\ typhimurium$ overexpressed in $E.\ coli$ overexpression system and purified as described in Chapter 2. In addition to the protein samples having 10 mM potassium phosphate buffer (pH 7.5), 20 μM EAL protein, and 0.2 mM TEMPOL spin probe (4-hydroxy-TEMPO, Sigma-Aldrich), 100 mM AmEtOH was added in a final volume of 0.3 ml. When present, DMSO was added to 2% v/v in the final volume of 0.3 ml.

6.2.2 Continuous wave EPR spectroscopy and EPR Simulations

Continuous wave EPR measurements were performed as describedn in Chapter 2. EPR acquisition parameters: Microwave frequency, 9.45 GHz; microwave power, 0.2 mW; magnetic field modulation, 0.2 mT; modulation frequency, 100 kHz; acquisition number, 4-8 spectra were averaged at each T value.

Simulations of the cw-EPR spectra were performed by using the Chili algorithm in the program, EasySpin [121] as described in Chapter 2. Briefly, simulations of the experimental spectra required two components for all the conditions. The two components simulations were performed by variation of the correlation times and normalized weights for the slow-motional ($\tau_{c,s}, W_s$) and fast-motional

($\tau_{c,f}, W_f$) components, and the corresponding intrinsic line widths.

6.3 RESULTS AND DISCUSSION

6.3.1 Temperature dependence of the TEMPOL EAL EPR line shape in frozen aqueous solution with AmEtOH: 0, and 2% v/v DMSO

The effect of temperature on the EPR line shape of the TEMPOL spin probe at different representative T values from the complete addressed range of 190-265 K is shown in Figure 6.1 for the EAL-AmEtOH, 0 and 2% v/v DMSO samples. The characteristic TEMPOL spectrum arises from interaction of the unpaired electron spin ($S = \frac{1}{2}$) with the nitroxide ^{14}N nuclear spin ($I = 1$), which produces three dominant spectral features that correspond to electron spin-spin transitions ($\triangle m_s = \pm\frac{1}{2}$) among $m_I = 0, \pm 1$ energy levels created by the electron-nuclear hyperfine interaction. [90] The time-dependent reorientation of the spin probe leads to rotational averaging of the unpaired electron g-anisotropy and the electron-^{14}N dipolar hyperfine interaction, and a consequent narrowing of the EPR line shape, [90] which is quantified by the τ_c obtained from spectral simulations. The X-band, cw-EPR spin probe approach is sensitive to TEMPOL reorientational motion in the τ_c range of $\approx 10^{-11}$ (rapid reorientation limit) to 10^{-7} s (rigid limit). [109]

For the 0 and 2% v/v DMSO conditions, the rigid-limit, powder pattern line

shape is observed at the lowest T value, and at the highest T values, the widths of the m_I lines start to narrow, and the overall spectral width approaches twice the value of the ^{14}N isotropic hyperfine coupling constant ($2A_{iso}$=3.4 mT=96 MHz). The transition from the rigid-limit, powder pattern line shape to initial motional-narrowed spectra, that represent averaging of the electron-nuclear dipolar anisotropy by tumbling of the TEMPOL, occurs at different T values for the two conditions: $T \geq$230 K for no DMSO condition and $T \geq$220 K for 2% v/v DMSO. Continuing this trend, the T values at which significant line-narrowing, owing to rapid tumbling, occur also decrease with the added 2% v/v DMSO: $T \geq$240 K for no DMSO condition and $T \geq$230 K for 2% v/v DMSO. Therefore, the line shapes in Figure 6.1 qualitatively show that tumbling motion of TEMPOL in 2% v/v added DMSO is detectably activated at $\approx$10 K lower in T, relative to the no DMSO condition, and that the transition to rapid tumbling motion in 2% v/v added DMSO is detectably activated at $\approx$10 K, relative to the no DMSO condition.

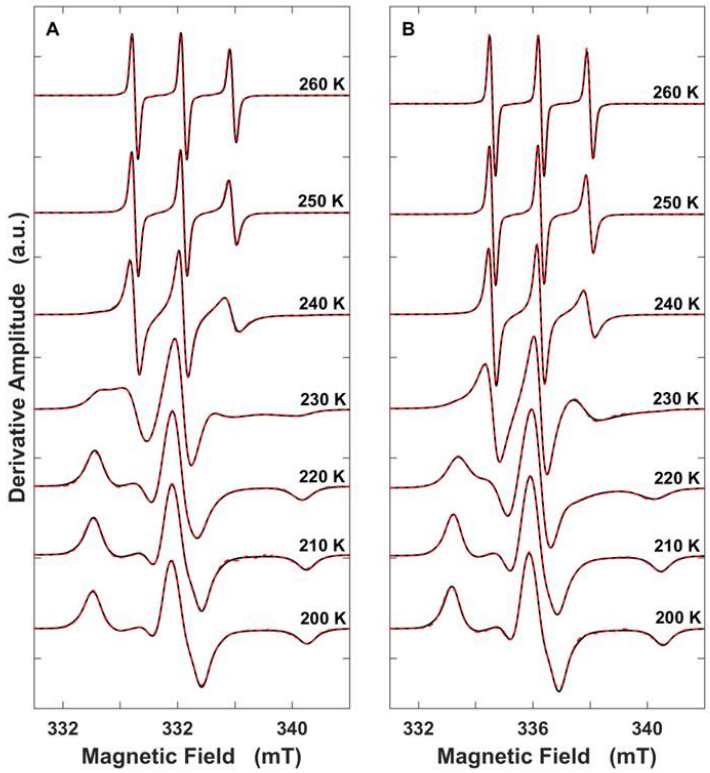

Figure 6.1: Temperature dependence of the TEMPOL EPR spectrum (black) and overlaid two-component EPR simulations (dashed red lines)) in EAL-AmEtOH aqueous solution. (A) 0% DMSO. (B) 2% v/v DMSO. EAL concentration was 20 μM. The spectra are normalized to the central peak-to-trough amplitude. Alignment along the magnetic field axis corresponds to the microwave frequency at 200 K.

6.3.2 Temperature dependence of the TEMPOL EAL rotational correlation times and normalized component weights in frozen aqueous solution with AmEtOH: No DMSO

EPR spectra were simulated to quantify the rotational mobility in terms of the τ_c and normalized W values of TEMPOL mobility components. The temperature dependence of τ_c in the presence of EAL and AmEtOH at no added DMSO displays two-component behavior, where the two components are characterized by a relatively short τ_c value (denoted as the "fast" tumbling component, $\tau_{c,f}$) and a relatively long τ_c value (denoted as "slow" tumbling component, $\tau_{c,s}$). The dependence of logτ_c on T is shown in Figure 6.2A (values: Table J.1 of Appendix 7.2) and is divided into four regions, as follows: $Region\ I$: Both logτ_c values lie above the tumbling detection criterion. $Region\ II$: A fast-tumbling population is present, with log$\tau_{c,f}$ $\leq$–7.0 and decreasing with T, along with a rigid population (simulated logτ_c>7.0). $Region\ III$: Both fast- and slow-tumbling populations are present, with log$\tau_{c,f}$,$\tau_{c,s}$ continuing to decrease with T. $Region\ IV$: Both fast- and slow-tumbling populations are still present and continue to decrease, with log$\tau_{c,s}$ approaching log$\tau_{c,f}$. The T value, $T_{II/III}$, at which the log$\tau_{c,f}$ and log$\tau_{c,s}$ values meet the criterion for detectable tumbling ($\leq$–7.0), determines the boundary of $Region\ II$ and $Region\ III$.

Figures 6.2B shows a plot of the normalized weights' slow component (W_s) and fast component (W_f)) dependence on T. The W_f is dominant in all four regions. However at the boundary of $Region\ II$ and III, there is a rapid drop

in W_f with a compensating increase in W_s. The W_f and W_s values are maintained for ≈15 K in $Region\ III$. In $Region\ IV$, the W_f values increases uniformly to a constant value of ≈80% at 265 K.

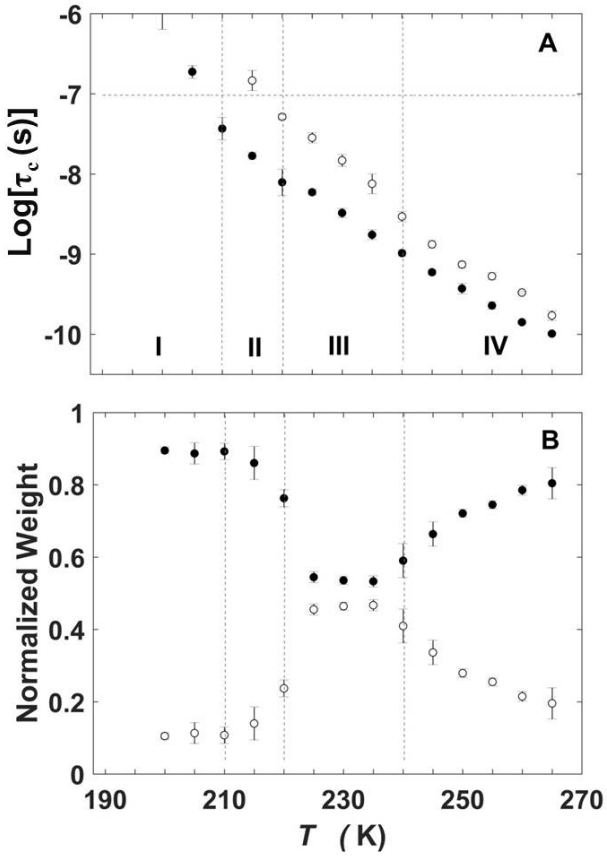

Figure 6.2: Temperature dependence of the rotational correlation time of TEMPOL and normalized mobility component weights, for EAL-AmEtOH, 0% DMSO. (A) Rotational correlation time. Horizontal dashed line represents upper limit of τ_c for detection of tumbling motion. (B) Normalized weight. Solid circles: fast component; open circles, slow component. Error bars represent standard deviations for three separate determinations.

6.3.3 Temperature dependence of the TEMPOL EAL rotational correlation times and normalized component weights in frozen aqueous solution with AmEtOH: 2% v/v DMSO

The dependence of logτ_c on T is shown in Figure 6.3A (values: Table J.2 of Appendix 7.2). Similar to Figure 6.2, it is divided into four regions, as follows: $Region\ I$: Both logτ_c values lie above the tumbling detection criterion. $Region\ II$: A fast-tumbling population is present, with log$\tau_{c,f}$ $\leq$–7.0 and decreasing with T, along with a rigid population (simulated logτ_c>7.0). $Region\ III$: Both fast- and slow-tumbling populations are present, with log$\tau_{c,f}$,$\tau_{c,s}$ continuing to decrease with T. $Region\ IV$: Both fast- and slow-tumbling populations are still present and continue to decrease, with log$\tau_{c,s}$ approaching log$\tau_{c,f}$. The T value, $T_{II/III}$, at which the log$\tau_{c,f}$ and log$\tau_{c,s}$ values meet the criterion for detectable tumbling ($\leq$–7.0), determines the boundary of $Region\ II$ and $Region\ III$.

Figures 6.3B shows a plot of the normalized weights' slow component (W_s) and fast component (W_f)) dependence on T. The W_f is dominant in all four regions. However, with increasing T across the $T_{II/III}$ transition, there is a shift in population from W_f to W_s. The W_f and W_s values are maintained for ≈35 K in $Region\ III$. $Region\ IV$: The W_f versus T dependence displays a subtle increase in the proportion of W_f for for all DMSO concentrations, T $\geq$245 K.

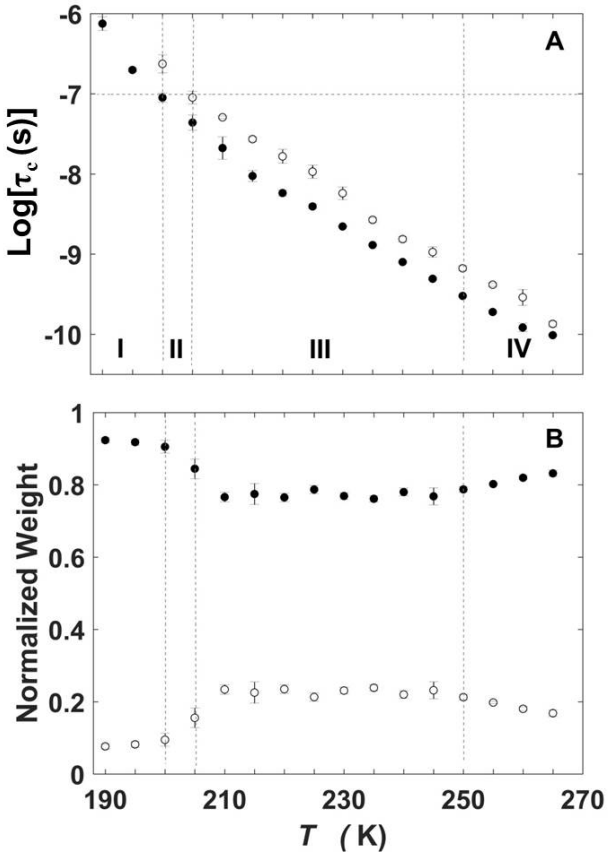

Figure 6.3: Temperature dependence of the rotational correlation time of TEMPOL and normalized mobility component weights, for EAL-AmEtOH, 0% v/v DMSO. (A) Rotational correlation time. Horizontal dashed line represents upper limit of τ_c for detection of tumbling motion. (B) Normalized weight. Solid circles: fast component; open circles, slow component. Error bars represent standard deviations for three separate determinations.

6.3.4 Fluid/solid transition of the protein-associated domain and in the mesodomain

We have characterized the region around the EAL protein in frozen aqueous solutions at cryogenic temperatures as shown in chapter 2. [133] The protein-associated domain (PAD) and the mesodomain were identified. The results presented in this chapter support this. Furthermore, the abrupt transition of the TEMPOL mobility from fast to slow, marked by a compensating decrease in W_s and increase in W_f in the direction of decreasing T at the $Region\ III$ and $Region\ II$ boundary (Figure 6.2B and 6.3B), indicates a fluid to solid transition in the PAD. This transition is not an artifact from the technique bandwidth limitation because the transition in the W values occurs over a T-range for which both PAD and mesodomain are fluid and within the detection window ($\log\tau_{c,f}$,$\log\tau_{c,s}$ <-7.0). It is worth nothing that this same type of transition has been identified in sample without the substrate, AmEtOH. [133] The transition is identified with the PAD, because the mesodomain maintains the fluid state across $Region\ III$ and $Region\ II$. Roos and Potes [160] have shown that such transitions in protein are known as order-disorder transition of the protein hydration layer, identified here as the PAD, and denoted, $T_{II/III}$. The $T_{II/III}$ values for the 0 and 2% v/v DMSO samples are 220 K and 205 K, respectively.

The similarity in behavior of this system, in relation to the system without the substrate (Chapter 2 and 6), is an indication that the properties of the PAD and mesodomain are maintained. This provides an approach to couple the central

reaction kinetics in EAL with the surface and solvent fluctuations around the EAL.

6.3.5 Quantification of the composition and uniformity properties of the PAD and mesodomain components

The rotational diffusion of the TEMPOL spin probe in the PAD and mesodoamain is governed by dynamical properties of each of the phases. As such the T dependence of τ_c over the T range of fluidity can be interpreted to provide quantification of the composition and uniformity properties of the PAD and mesodomain components. This is done by using the Stokes-Einstein expression (equation 2.4.3) described in chapter 2 and 6. Figure 6.4 shows that Arrhenius plots of $\log\tau_c$ versus $1/T$ for $Region\ III$ conditions for both the 0 and 2% v/v DMSO conditions are linear, and therefore consistent with the Arrhenius form. The Table 6.1 gives the values of the Arrhenius parameters; A (frequency factor) and E_a (barrier to rotational motion of the solvent otherwise known as the activation energy) obtained from the intercept and slope, respectively. Figure 6.4 and Table 6.1 shows a subtle trend of decreasing E_a and A with added 2% v/v DMSO. The slightly higher E_a values for the no DMSO condition are consistent with the small volume of the mesodomain when compared with the volume of the PAD. At 0% DMSO, the only contribution to the mesodomain volume comes from the 0.6% v/v AmEtOH in solution.Therefore, at 0% DMSO, the role of confinement, as described in Chapter 6, by the ice boundary in dictating the PAD dynamics is

dramatic. However, for the 2% v/v DMSO condition, the effect is diminished owing to the increased volume of the mesodomain, and increased mean TEMPOL distance from the ice boundary. We argued that this cooperativity in the solvent dynamics in the PAD and mesodomain is bidirectional.

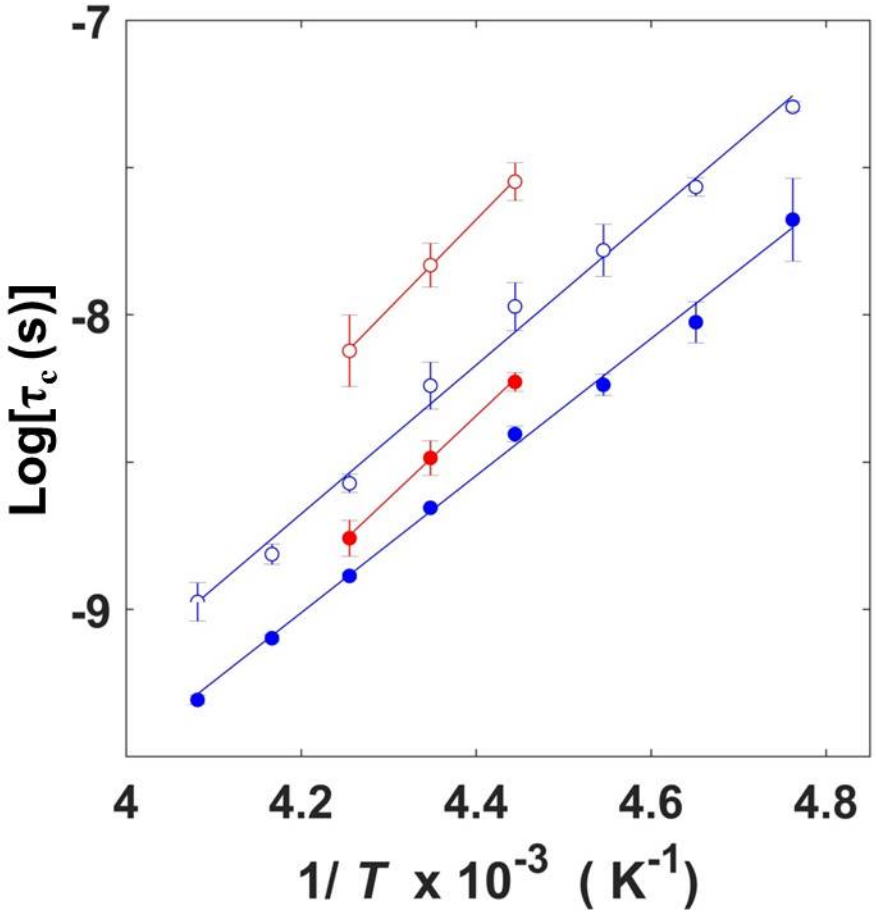

Figure 6.4: Arrhenius plot of rotational correlation times obtained for the different conditions, and overlaid best-fit linear relations. NO DMSO (red): fast tumbling component, filled circles; slow tumbling component, open circles. 2% v/v DMSO (blue): fast tumbling component, filled circles; slow tumbling component, open circles. Error bars correspond to standard deviations for three separate experiments.

Table 6.1: Arrhenius parameters obtained from the temperature-dependence of the rotational correlation time for TEMPOL tumbling motion in the EAL-AmEtOH systems, corresponding to temperatures for which $\log\tau_c \leq -7.0$.[a]

Sample	$\log$**[1/A] (s^{-1})**	E_a **(kcal mol^{-1})**	R^2 [b]
F: No DMSO	-20.69±2.18	12.80±2.29	0.9992
S: No DMSO	-21.04±1.67	13.90±1.76	0.9996
F: 2% v/v DMSO	-18.79±0.30	10.60±0.31	0.9965
S: 2% v/v DMSO	-19.29±0.47	11.60±0.49	0.9929

[a] Values correspond to linear fit of results in the Arrhenius plot, Figure 6.4. F and S correspond to component 1 and 2, respectively.

[b] R is Pearson's correlation coefficient.

6.4 SUMMARY

The results presented in this chapter lay the foundation for kinetic studies on the enzymatic mechanism of EAL with DMSO as a cosolvent, and by extension other enzymes. The fluidizing effect of the added 2% v/v DMSO on the dynamics in the mesodomain, and the coupled increase in PAD dynamics, is manifested in the lowering of the $T_{II/III}$ by ≈15 K ($T_{II/III}$=220 and 205 K for 0 and 2% v/v DMSO, respectively) as shown in Figure 6.2 and 6.3. This is a method to precisely control the solvent and surface dynamics around EAL as a tunable parameter in quantifying and investigating the mechanism of coupling between solvent and surface dynamics, and chemical reaction steps in EAL. The results from this Chapter,

with the addition of AmiEtOH, are in line with conclusions drawn from Chapter 6. This opens new frontiers for the EAL kinetic measurements with DMSO as a cosolvent in an effort to provide unequivocal support to the T-dependent model of the free energy landscape of the substrate radical pair decay. [92]

Chapter 7

Summary and Conclusion

7.1 State of the Art

It has been shown that water is an integral part of protein structure and plays a crucial role in its function. [140, 160–166] As pointed out in Chapter 2, proteins require a minimal level of mobile hydration water, in order to execute native function. [44–46] Experimental studies have also found that the bulk water dynamics around a protein is influenced by the protein fluctuational motions at distances of up to 20 Å from the protein surface, [47] and computational studies suggest mechanistic features of distinct, protein-influenced water dynamics extending to 10 Å. [48, 49] When water is removed by drying and or lowering of T to solidify the solvent, protein fluctuations are lowered in frequency and amplitude and function suppressed. [44, 46, 50–52] The EAL is a bacterial enzyme that is involved in gut microbiome homeostasis, [4–6] and in disease conditions caused by pathogenic strains of $Salmonella$ and $E.\ coli$, in humans. [7,8] The EAL catalyzes the conversion of ethanolamine to acetaldehyde and ammonia, and is thought to function under pathogenic conditions with other proteins of the ethanolamine utilization pathway in the Eut BMC, a sub-cellular organelle. [24,25] The ability to use ethanolamine as the sole source of energy confers an advantage for bacterial colonization of the gut. Several pathogenic bacteria, including $Salmonella$, use the ability to metabolize ethanolamine to survive in ethanolamine rich environments such as in foods, and within their hosts. [4–8, 27–31] As a result of this, a strong correlation has been found between food poisoning bacteria and the presence of eut genes. [32] Studies have been done to elucidate the molecular basis of

EAL catalysis by using low-T (T=193-250 K), full-spectrum, time-resolved EPR spectroscopy in frozen, globally-polycrystalline aqueous solutions to characterize kinetics and mechanism of individual steps in the EAL catalytic cycle. [92, 93, 96]

The native reactivity of EAL at cryogenic T values is remarkable, because protein functions that require atomic displacements of approximately >1 Å require a fluid state of the surrounding solvent. [44, 46, 52] How the enzyme is able to conduct the elaborate rearrangement, and subsequent hydrogen transfer and cobalamin cofactor bond reformation reaction steps, when the bulk aqueous solvent is rigid warrants an explanation. In addition, the elucidation of the molecular basis of EAL catalysis, and the intracellular trafficking and targeting of EAL to the Eut BMC, can lead to drug development that suppress bacteria with the ability to metabolize ethanolamine from proliferation within the gut. Furthermore, we seek to develop a method to control and "tune" the steps involved in EAL catalysis in an effort to understand the mechanism of EAL catalysis. A holistic understanding of the mechanism of EAL catalysis will inform on the effect of solvent and surface fluctuations on EAL catalysis, and other enzyme systems.

7.2 Significance of the work presented in this dissertation

The crucial role of water to protein structure, protein folding, stability and activity both at physiological and non-physiological conditions [140, 160–166] has driven studies' focus on understanding the coupling between protein function and their

hydration water and the general bulk solvent around them. [44–49] Herein, we approach this problem in four ways: (1) In Chapter 2, we characterize the solvent environment around the protein EAL by using the electron spin probe TEMPOL, identifying the PAD and the mesodomain. The dynamics of the PAD and the mesodomain are mutually nonexclusive events. (2) In Chapter 4, we focus on the surface characterization of the EAL protein by using the spin label 4MT which binds to the surface of the protein, at residue C37 of the EutC subunit of EAL, in constrast to the spin probe which does not bind to the protein. From the results, we obtain insights into the protein stability and function based on the spin label position at the $\beta C37$ site of the N-terminal signal sequence associated domain of the EAL. (3) We show in Chapters 6 and 5 that the properties and dynamics of the protein surface and the bulk solvent around the protein can be controlled. This is achieved through systematic "tuning" of solvent dynamics and glass transitions around the enzyme by using dimethylsulfoxide (DMSO) and T variation. In adition, in Chapter 6, we establish the role of confinement effects in determining measured solvent dynamics around proteins. The results are useful in studies where additional insights into the mechanism of the protein (for instance EAL) action through control, or, “tuning” of the steps in the protein reaction cycle is required. [92–96, 167] (4) As a proof of concept, in Chapter 5.4.3, we apply the above methods to the EAL system with the addition of the substrate, AmEtOH. The results support the precise characterization of the solvent phases around the EAL and also the control of solvent and protein surface dynamics as a tunable parameter for quantifying the coupling between solvent and protein fluctuations

and catalysis in EAL. Furthermore, our results in conjunction with preliminary kinetic measurements, with DMSO as a cosolvent, show that the protein surface dynamics are indeed coupled to the central enzyme reaction. This has opened new frontiers to use DMSO as a cosolvent in the kinetic studies of the mechanism of EAL catalysis.

In summary, the work presented herein indicates that it is not just the hydration water controlling the biomolecular dynamics, also biomolecules affect the dynamics of the hydration water leading to a coupled biomolecular-hydration water dynamics. Similar conclusions are drawn from the effect of the mesodomain on the hydration water as well as the mesodomain and the bulk ice-crystalline boundary. In other words, there is a mutual, bidirectional coupling that exists between the PAD/protein, PAD/mesodomain and mesodomain/ice-crystalline boundary dynamics. Our results also show that the variation of the T-value of the protein dynamical transition over the observed wide range (e.e., $\sim$ 180-240 K) [142] may originate, at least in part, from different confinement effects, from different compositions or T-dependent fluidities of the outer-boundary phase apposed to the hydration layer-protein system. We propose that at cryogenic temperatures, the hydration water facilitates the protein dynamics and hence function. Overall, the work presented herein is first of its kind to use a well-defined (composition, geometric dimensions, temperature-dependence of viscosity) cosolvent-tuned mesodomain system toward the precise characterization of the solvent phases around EAL and precise control of solvent and protein surface dynamics as a tunable parameter for quantifying the coupling between solvent

and protein fluctuations and catalysis in EAL, and other enzymes.

Appendix

C EPR spectrum from frozen aqueous solution at 0% DMSO, in the absence of EAL

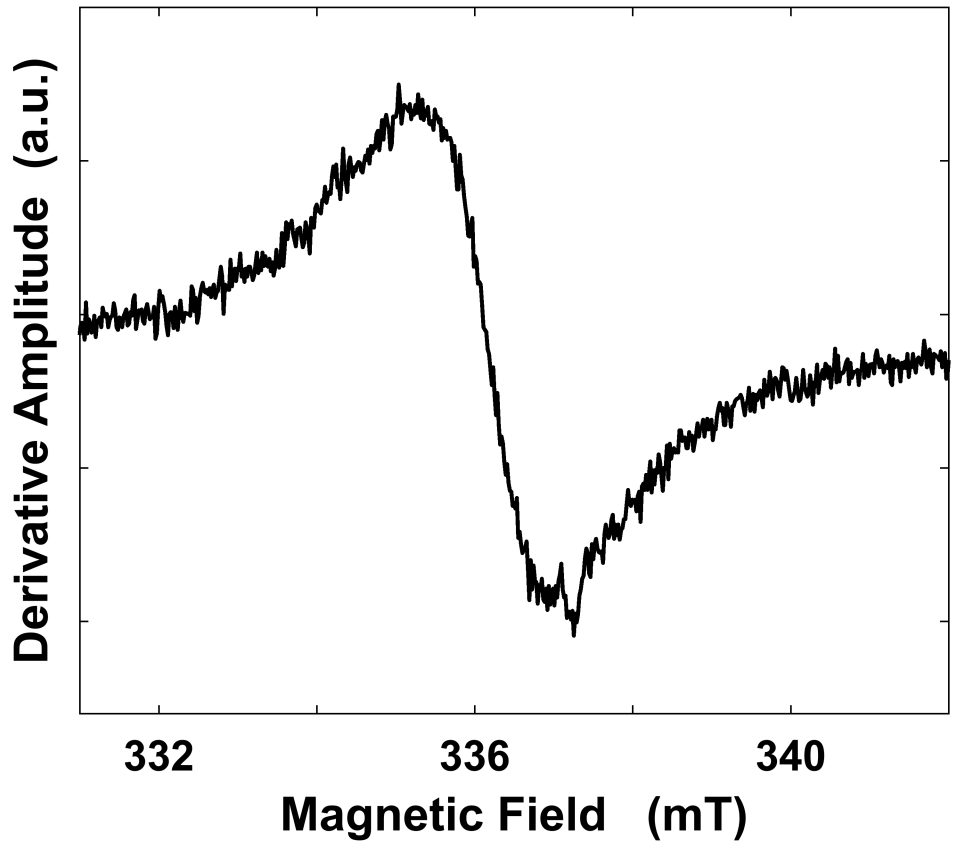

Figure C.1: EPR spectrum of TEMPOL in frozen aqueous solution in the absence of EAL. The broad spectrum, with unresolved ^{14}N hyperfine features, is observed at all temperature values. EPR conditions are identical to those in Figure 2.1, with microwave frequency, 9.443 GHz. Temperature, 230 K.

D The logτ_c and W values at different temperatures for the ±EAL with TEMPOL, 0 and 1% v/v DMSO system

Table D.1: The logτ_c and W values at different temperatures for the EAL-TEMPOL, 0% v/v DMSO system.[a]

T (K)	Log$\tau_{c,f}$ (s)	W_f	Log$\tau_{c,s}$ (s)	W_s
230	-7.17±0.10	0.85±0.01	-6.38±0.25	0.15±0.01
235	-7.38±0.07	0.84±0.01	-6.50±0.26	0.16±0.01
240	-7.61±0.05	0.81±0.01	-6.57±0.27	0.19±0.01
245	-8.06±0.01	0.57±0.03	-6.76±0.45	0.43±0.03
250	-8.31±0.05	0.42±0.08	-6.93±0.49	0.58±0.08
255	-8.60±0.07	0.22±0.01	-7.91±0.17	0.78±0.01
260	-9.09±0.07	0.20±0.02	-8.24±0.07	0.80±0.02
265	-9.50±0.03	0.30±0.04	-8.53±0.06	0.70±0.04

[a] Mean values and standard deviations correspond to three separate experiments

Table D.2: The logτ_c and W values at different temperatures for the EAL-TEMPOL, 1% v/v DMSO system.[a]

T **(K)**	**Log**$\tau_{c,f}$ **(s)**	$\mathbf{W_f}$	**Log**$\tau_{c,s}$ **(s)**	$\mathbf{W_s}$
200	-7.09±0.03	0.92±0.00	-6.26±0.05	0.084 ±0.00
205	-7.38±0.03	0.90±0.00	-6.48±0.08	0.10±0.00
210	-7.85±0.09	0.70±0.08	-7.20 ±0.08	0.30±0.08
215	-8.15±0.03	0.61±0.01	-7.39±0.05	0.39±0.01
220	-8.36±0.03	0.60±0.03	-7.60±0.08	0.40±0.03
225	-8.56±0.01	0.61±0.00	-7.92±0.06	0.39±0.01
230	-8.81±0.01	0.62±0.01	-8.22±0.04	0.39±0.00
235	-8.95±0.01	0.62±0.01	-8.44±0.01	0.39±0.01
240	-9.09±0.02	0.61±0.01	-8.56±0.02	0.39±0.01
245	-9.28±0.01	0.61±0.01	-8.73±0.06	0.39±0.01
250	-9.44±0.02	0.62±0.01	-8.88±0.09	0.38±0.01
255	-9.61±0.02	0.64±0.01	-9.02±0.06	0.36±0.01
260	-9.79±0.03	0.67±0.01	-9.14±0.03	0.33±0.01
265	-9.94±0.03	0.60±0.00	-9.24±0.03	0.30±0.00

[a] Mean values and standard deviations correspond to three separate experiments

Table D.3: The logτ_c values at different temperatures for 1% v/v DMSO with TEMPOL, in the absence of EAL.[a]

T **(K)**	**Logτ_c (s)**
200	-7.34±0.06
205	-7.67±0.05
210	-7.96±0.04
215	-8.23±0.06
220	-8.48±0.03
225	-8.68±0.04
230	-8.83±0.01
235	-8.99±0.03
240	-9.16±0.05
245	-9.35±0.02
250	-9.54±0.03
255	-9.69±0.05
260	-9.86±0.02
265	-9.98±0.02

[a] Mean values and standard deviations correspond to three separate experiments

E Arrhenius parameters obtained from the rotational correlation time for TEMPOL tumbling motion in the absence and presence of EAL, 0% and 1% v/v DMSO systems

Table E.1: Arrhenius parameters obtained from the temperature-dependence of the rotational correlation time for TEMPOL tumbling motion in the absence and presence of EAL, 0% and 1% v/v DMSO systems, corresponding to temperatures for which $\log\tau_c \leq -7.0$.[a]

Condition: ±EAL,% v/v DMSO	$\ln$**[A] (s^{-1})**	E_a **(kcal mol^{-1})**	R^2 [b]
+EAL, 0, fast	-56.64	-18.50	0.9748
+EAL, 0, slow	-55.95	-19.20	0.9990
+EAL, 1, fast	-40.76	-9.42	0.9982
+EAL, 1, slow	-40.06	-9.79	0.9868
-EAL, 1	-41.22	-9.56	0.9963

[a] Values correspond to linear fit of results in the Arrhenius plot, Figure 2.9.

[b] R is Pearson's correlation coefficient.

F Primers used in the development of the EAL mutants

Table F.1: Primers used in the development of the EAL mutants.[a]

Primer Name	5′ to 3′ Primer Sequence
b_C37A_FP	GGC GCA AAG CCG CAG GCG GCC GCG CCG ACG G
b_C37A_BP	CCG TCG GCG CGG CCG CCT GCG GCT TTG CGC C
b_C46A_FP	GAC CGA AAG CGC CGC GCT GGA TTT AGG
b_C46A_BP	CCT AAA TCC AGC GCG GCG CTT TCG GTC
b_C260A_FP	GGC CGA CAG AAC CGC GAT TTC AAA CAT TC
b_C260A_BP	GAA TGT TTG AAA TCG CGG TTC TGT CGG CC

[a]Primers obtained from Integrated DNA Technologies (Coralville, IA, US).

G Reorientational correlation times and normalized weight values at the different temperatures for EAL-4MT, 0 and 1% v/v DMSO

Table G.1: Reorientational correlation times and normalized weight values at the different temperatures for EAL-4MT, 0% DMSO.[a]

T **(K)**	**Log**$\tau_{c,f}$ **(s)**	$\mathbf{W_f}$	**Log**$\tau_{c,s}$ **(s)**	$\mathbf{W_s}$
230	-7.07±0.09	0.14±0.02	-6.61±0.14	0.86±0.02
235	-7.28±0.10	0.15±0.05	-6.86±0.16	0.85±0.05
240	-7.56±0.10	0.25±0.06	-7.10±0.11	0.75±0.06
245	-7.80±0.20	0.33±0.01	-7.34±0.07	0.67±0.01
250	-8.32±0.17	0.34±0.01	-7.60±0.42	0.66±0.01
255	-8.63±0.15	0.34±0.02	-7.88±0.19	0.66±0.02
260	-8.85±0.23	0.38±0.02	-8.04±0.20	0.62±0.02
265	-9.10±0.06	0.43±0.00	-8.34±0.11	0.57±0.03

[a]Mean values and standard deviations correspond to three separate experiments

Table G.2: Reorientational correlation times and normalized weight values at the different temperatures for EAL-4MT, 1% v/v DMSO.[a]

T **(K)**	**Log**$\tau_{c,f}$ **(s)**	$\mathbf{W_f}$	**Log**$\tau_{c,s}$ **(s)**	$\mathbf{W_s}$
210	-6.51±0.08	0.13±0.00	-5.99±0.27	0.87±0.00
215	-6.96±0.04	0.15±0.01	-6.47±0.16	0.85±0.01
220	-7.27±0.03	0.17±0.02	-6.68±0.15	0.83±0.02
225	-7.50±0.02	0.21±0.02	-6.84±0.10	0.80±0.02
230	-7.70±0.03	0.25±0.02	-7.20±0.06	0.75±0.02
235	-7.89±0.13	0.27±0.01	-7.41±0.06	0.73±0.01
240	-8.13±0.16	0.29±0.00	-7.61±0.12	0.71±0.00
245	-8.33±0.08	0.32±0.02	-7.74±0.05	0.68±0.02
250	-8.65±0.05	0.29±0.05	-7.94±0.03	0.71±0.05
255	-8.84±0.02	0.35±0.01	-8.05±0.11	0.65±0.01
260	-9.04±0.03	0.37±0.01	-8.24±0.07	0.63±0.01
265	-9.26±0.06	0.40±0.04	-8.41±0.05	0.60±0.03

[a]Mean values and standard deviations correspond to three separate experiments

H Enthalpy and entropy values for the equilibrium between W_s and W_f mobility components in 1% v/v DMSO

Table H.1: Enthalpy and entropy values for the equilibrium between W_s and W_f mobility components in 1% v/v DMSO.[a]

Sample	**△H (kcal/mol)**	**△H (cal/mol/K)**	R^2 [b]
EAL, 1% v/v DMSO	5.6	19.2	0.9224

[a] Values correspond to linear fit of van't Hoff plot of data, averaged for each temperature from three separate experiments and derived of W_s, W_f values, over 225-265 K.

[b] R is Pearson's correlation coefficient.

I Reorientational correlation times and normalized weight values at the different temperatures for EAL-4MT, 0.5, 2 and 4% v/v DMSO

Table I.1: Reorientational correlation times and normalized weight values at the different temperatures for EAL-4MT, 0.5% DMSO.[a]

T (K)	Log$\tau_{c,f}$ (s)	W_f	Log$\tau_{c,s}$ (s)	W_s
200	-6.55 ± 0.07	0.14 ± 0.01	-6.13 ± 0.19	0.86 ± 0.01
205	-6.74 ± 0.05	0.14 ± 0.01	-6.21 ± 0.11	0.86 ± 0.01
210	-6.79 ± 0.04	0.14 ± 0.00	-6.28 ± 0.13	0.86 ± 0.00
215	-6.91 ± 0.04	0.14 ± 0.02	-6.36 ± 0.13	0.86 ± 0.02
220	-7.13 ± 0.04	0.15 ± 0.02	-6.38 ± 0.15	0.85 ± 0.02
225	-7.26 ± 0.03	0.14 ± 0.04	-6.58 ± 0.12	0.86 ± 0.04
230	-7.36 ± 0.05	0.22 ± 0.03	-6.82 ± 0.06	0.78 ± 0.03
235	-7.50 ± 0.06	0.21 ± 0.01	-7.03 ± 0.10	0.79 ± 0.01
240	-7.72 ± 0.06	0.22 ± 0.01	-7.20 ± 0.05	0.78 ± 0.01
245	-7.94 ± 0.04	0.25 ± 0.02	-7.39 ± 0.06	0.75 ± 0.02
250	-8.28 ± 0.07	0.31 ± 0.01	-7.70 ± 0.09	0.69 ± 0.01
255	-8.61 ± 0.02	0.33 ± 0.06	-7.98 ± 0.04	0.67 ± 0.06
260	-8.88 ± 0.02	0.38 ± 0.07	-8.20 ± 0.04	0.62 ± 0.07
265	-9.18 ± 0.01	0.40 ± 0.05	-8.44 ± 0.05	0.60 ± 0.05

[a]Mean values and standard deviations correspond to three separate experiments

Table I.2: Reorientational correlation times and normalized weight values at the different temperatures for EAL-4MT, 2% DMSO.[a]

T **(K)**	**Log**$\tau_{c,f}$ **(s)**	$\mathbf{W_f}$	**Log**$\tau_{c,s}$ **(s)**	$\mathbf{W_s}$
200	-6.83 $\pm$ 0.07	0.11 $\pm$ 0.01	-5.84 $\pm$ 0.66	0.89 $\pm$ 0.01
205	-6.96 $\pm$ 0.06	0.13 $\pm$ 0.01	-6.32 $\pm$ 0.06	0.87 $\pm$ 0.01
210	-7.06 $\pm$ 0.05	0.14 $\pm$ 0.01	-6.41 $\pm$ 0.08	0.86 $\pm$ 0.01
215	-7.18 $\pm$ 0.03	0.15 $\pm$ 0.01	-6.62 $\pm$ 0.02	0.85 $\pm$ 0.01
220	-7.37 $\pm$ 0.02	0.17 $\pm$ 0.01	-7.03 $\pm$ 0.09	0.83 $\pm$ 0.01
225	-7.52 $\pm$ 0.04	0.19 $\pm$ 0.01	-7.17 $\pm$ 0.06	0.81 $\pm$ 0.01
230	-7.73 $\pm$ 0.06	0.24 $\pm$ 0.02	-7.29 $\pm$ 0.08	0.76 $\pm$ 0.02
235	-7.97 $\pm$ 0.12	0.25 $\pm$ 0.02	-7.48 $\pm$ 0.15	0.75 $\pm$ 0.02
240	-8.18 $\pm$ 0.12	0.28 $\pm$ 0.01	-7.67 $\pm$ 0.15	0.72 $\pm$ 0.01
245	-8.43 $\pm$ 0.03	0.34 $\pm$ 0.02	-7.92 $\pm$ 0.11	0.64 $\pm$ 0.02
250	-8.62 $\pm$ 0.03	0.38 $\pm$ 0.01	-8.10 $\pm$ 0.04	0.62 $\pm$ 0.01
255	-8.86 $\pm$ 0.01	0.42 $\pm$ 0.04	-8.25 $\pm$ 0.05	0.58 $\pm$ 0.04
260	-9.10 $\pm$ 0.02	0.44 $\pm$ 0.03	-8.59 $\pm$ 0.08	0.56 $\pm$ 0.03

[a]Mean values and standard deviations correspond to three separate experiments

Table I.3: Reorientational correlation times and normalized weight values at the different temperatures for EAL-4MT, 4% DMSO.[a]

T **(K)**	**Log**$\tau_{c,f}$ **(s)**	$\mathbf{W_f}$	**Log**$\tau_{c,s}$ **(s)**	$\mathbf{W_s}$
200	-6.80 $\pm$ 0.09	0.11 $\pm$ 0.01	-6.43 $\pm$ 0.18	0.89 $\pm$ 0.01
205	-7.01 $\pm$ 0.01	0.13 $\pm$ 0.01	-6.53 $\pm$ 0.07	0.87 $\pm$ 0.02
210	-7.12 $\pm$ 0.02	0.14 $\pm$ 0.01	-6.74 $\pm$ 0.09	0.86 $\pm$ 0.01
215	-7.26 $\pm$ 0.04	0.15 $\pm$ 0.01	-7.10 $\pm$ 0.14	0.85 $\pm$ 0.01
220	-7.46 $\pm$ 0.07	0.19 $\pm$ 0.01	-7.23 $\pm$ 0.20	0.81 $\pm$ 0.01
225	-7.61 $\pm$ 0.07	0.22 $\pm$ 0.02	-7.32 $\pm$ 0.01	0.78 $\pm$ 0.02
230	-7.88 $\pm$ 0.06	0.25 $\pm$ 0.02	-7.61 $\pm$ 0.03	0.75 $\pm$ 0.02
235	-8.11 $\pm$ 0.13	0.28 $\pm$ 0.01	-7.83 $\pm$ 0.03	0.72 $\pm$ 0.01
240	-8.36 $\pm$ 0.08	0.31 $\pm$ 0.02	-7.95 $\pm$ 0.10	0.69 $\pm$ 0.02
245	-8.49 $\pm$ 0.05	0.36 $\pm$ 0.01	-8.13 $\pm$ 0.07	0.64 $\pm$ 0.01
250	-8.72 $\pm$ 0.02	0.38 $\pm$ 0.01	-8.35 $\pm$ 0.05	0.62 $\pm$ 0.01
255	-8.87 $\pm$ 0.07	0.44 $\pm$ 0.03	-8.46 $\pm$ 0.06	0.56 $\pm$ 0.03
260	-9.09 $\pm$ 0.06	0.47 $\pm$ 0.03	-8.65 $\pm$ 0.06	0.53 $\pm$ 0.03

[a]Mean values and standard deviations correspond to three separate experiments

J The logτ_c values at different temperatures for the EAL-AmEtOH with TEMPOL, 0 and 2% v/v DMSO system

Table J.1: The logτ_C and W values at different temperatures for the EAL-AmEtOH, No DMSO system.[a]

T (K)	Log$\tau_{c,f}$ (s)	W_f	Log$\tau_{c,s}$ (s)	W_s
200	-5.73±0.46	0.90±0.01	-5.08±0.25	0.10±0.01
205	-6.72±0.08	0.89±0.03	-5.17±0.22	0.11±0.03
210	-7.43±0.14	0.89±0.02	-5.78±0.16	0.11±0.02
215	-7.77±0.04	0.86±0.05	-6.83±0.13	0.14±0.05
220	-8.10±0.16	0.76±0.02	-7.29±0.03	0.24±0.02
225	-8.23±0.03	0.54±0.02	-7.55±0.06	0.46±0.02
230	-8.49±0.06	0.54±0.01	-7.83±0.07	0.46±0.01
235	-8.76±0.06	0.53±0.02	-8.12±0.12	0.47±0.02
240	-8.99±0.04	0.59±0.05	-8.53±0.06	0.41±0.05
245	-9.23±0.03	0.66±0.03	-8.88±0.05	0.34±0.03
250	-9.43±0.06	0.72±0.01	-9.13±0.04	0.28±0.01
255	-9.64±0.05	0.67±0.13	-9.24±0.09	0.33±0.13
260	-9.85±0.02	0.79±0.01	-9.50±0.01	0.21±0.01
265	-9.99±0.02	0.80±0.04	-9.77±0.06	0.20±0.04

[a]Mean values and standard deviations correspond to three separate experiments

Table J.2: The logτ_C and W values at different temperatures for the EAL-AmEtOH, 2% v/v DMSO system.[a]

T **(K)**	**Log$\tau_{c,f}$ (s)**	$\mathbf{W_f}$	**Log$\tau_{c,s}$ (s)**	$\mathbf{W_s}$
190	-6.13±0.09	0.92±0.01	-5.50±0.11	0.08±0.01
195	-6.70±0.02	0.92±0.01	-5.65±0.17	0.08±0.01
200	-7.05±0.06	0.91±0.02	-6.63±0.11	0.09±0.01
205	-7.36±0.10	0.84±0.02	-7.05±0.09	0.16±0.02
210	-7.68±0.14	0.77±0.01	-7.29±0.02	0.23±0.01
215	-7.96±0.12	0.77±0.02	-7.57±0.03	0.23±0.01
220	-8.24±0.04	0.77±0.01	-7.78±0.09	0.23±0.01
225	-8.41±0.03	0.79±0.01	-7.97±0.08	0.21±0.01
230	-8.66±0.00	0.77±0.01	-8.24±0.08	0.23±0.01
235	-8.89±0.01	0.76±0.01	-8.57±0.03	0.24±0.01
240	-9.10±0.01	0.78±0.01	-8.81±0.03	0.22±0.01
245	-9.31±0.02	0.77±0.02	-8.98±0.07	0.23±0.02
250	-9.52±0.01	0.79±0.01	-9.18±0.03	0.21±0.01
255	-9.72±0.02	0.80±0.01	-9.38±0.03	0.20 ± 0.01
260	-9.91±0.05	0.82±0.01	-9.54±0.10	0.18±0.01
265	-10.01±0.01	0.83±0.01	-9.87 ±0.03	0.17±0.01

[a]Mean values and standard deviations correspond to three separate experiments

K The logτ_c and W values at different temperatures for the ±EAL with TEMPOL, 0.5, 2, and 4% v/v DMSO system

Table K.1: The logτ_c and W values at different temperatures for the EAL-TEMPOL, 0.5% v/v DMSO system.[a]

T (K)	Log$\tau_{c,f}$ (s)	W_f	Log$\tau_{c,s}$ (s)	W_s
200	-7.23 ± 0.14	0.80 ± 0.05	-5.92 ± 0.22	0.20 ± 0.05
205	-7.35 ± 0.10	0.78 ± 0.03	-6.61 ± 0.21	0.22 ± 0.03
210	-7.59 ± 0.04	0.78 ± 0.01	-6.80 ± 0.07	0.22 ± 0.01
215	-8.18 ± 0.00	0.38 ± 0.02	-7.10 ± 0.01	0.62 ± 0.02
220	-8.31 ± 0.01	0.43 ± 0.01	-7.41 ± 0.07	0.57 ± 0.01
225	-8.50 ± 0.01	0.43 ± 0.01	-7.74 ± 0.01	0.57 ± 0.01
230	-8.70 ± 0.02	0.43 ± 0.01	-8.07 ± 0.02	0.57 ± 0.01
235	-8.84 ± 0.03	0.43 ± 0.00	-8.26 ± 0.11	0.57 ± 0.00
240	-9.01 ± 0.03	0.42 ± 0.03	-8.52 ± 0.01	0.58 ± 0.03
245	-9.18 ± 0.05	0.42 ± 0.01	-8.75 ± 0.10	0.58 ± 0.01
250	-9.37 ± 0.11	0.43 ± 0.01	-8.76 ± 0.18	0.57 ± 0.01
255	-9.56 ± 0.03	0.45 ± 0.02	-9.02 ± 0.09	0.55 ± 0.02
260	-9.71 ± 0.03	0.46 ± 0.01	-9.38 ± 0.02	0.54 ± 0.01
265	-9.89 ± 0.05	0.47 ± 0.01	-9.60 ± 0.05	0.53 ± 0.01

[a] Mean values and standard deviations correspond to three separate experiments

Table K.2: The logτ_c and W values at different temperatures for the EAL-TEMPOL, 2% v/v DMSO system.[a]

T **(K)**	**Log$\tau_{c,f}$ (s)**	$\mathbf{W_f}$	**Log$\tau_{c,s}$ (s)**	$\mathbf{W_s}$
190	-6.42 ± 0.09	0.93 ± 0.01	-6.12 ± 0.10	0.07 ± 0.01
195	-6.99 ± 0.06	0.92 ± 0.00	-6.24 ± 0.02	0.08 ± 0.00
200	-7.29 ± 0.04	0.94 ± 0.00	-6.62 ± 0.03	0.06 ± 0.00
205	-7.64 ± 0.10	0.85 ± 0.04	-7.15 ± 0.03	0.15 ± 0.04
210	-8.09 ± 0.05	0.74 ± 0.01	-7.54 ± 0.08	0.26 ± 0.01
215	-8.30 ± 0.05	0.74 ± 0.01	-7.73 ± 0.08	0.26 ± 0.01
220	-8.46 ± 0.03	0.73 ± 0.01	-7.88 ± 0.09	0.27 ± 0.01
225	-8.63 ± 0.02	0.71 ± 0.01	-8.14 ± 0.03	0.29 ± 0.01
230	-8.77 ± 0.01	0.72 ± 0.02	-8.34 ± 0.01	0.28 ± 0.02
235	-8.92 ± 0.09	0.74 ± 0.03	-8.61 ± 0.11	0.26 ± 0.03
240	-9.12 ± 0.01	0.74 ± 0.02	-8.69 ± 0.06	0.26 ± 0.02
245	-9.29 ± 0.02	0.75 ± 0.04	-8.86 ± 0.02	0.25 ± 0.04
250	-9.51 ± 0.01	0.76 ± 0.01	-9.05 ± 0.04	0.24 ± 0.01
255	-9.67 ± 0.00	0.77 ± 0.01	-9.18 ± 0.04	0.23 ± 0.01
260	-9.84 ± 0.01	0.80 ± 0.01	-9.47 ± 0.03	0.20 ± 0.01
265	-9.96 ± 0.01	0.82 ± 0.02	-9.89 ± 0.08	0.18 ± 0.02

[a] Mean values and standard deviations correspond to three separate experiments

Table K.3: The logτ_c and W values at different temperatures for the EAL-TEMPOL, 4% v/v DMSO system.[a]

T **(K)**	**Log$\tau_{c,f}$ (s)**	$\mathbf{W_f}$	**Log$\tau_{c,s}$ (s)**	$\mathbf{W_s}$
190	-6.43 ± 0.28	0.94 ± 0.02	-6.15 ± 0.05	0.06 ± 0.02
195	-7.02 ± 0.09	0.93 ± 0.00	-6.23 ± 0.05	0.07 ± 0.00
200	-7.48 ± 0.10	0.85 ± 0.03	-7.04 ± 0.10	0.15 ± 0.03
205	-7.84 ± 0.05	0.82 ± 0.02	-7.43 ± 0.07	0.18 ± 0.02
210	-8.04 ± 0.04	0.81 ± 0.01	-7.80 ± 0.03	0.19 ± 0.01
215	-8.28 ± 0.04	0.82 ± 0.01	-7.95 ± 0.08	0.18 ± 0.01
220	-8.45 ± 0.03	0.81 ± 0.01	-8.14 ± 0.09	0.19 ± 0.01
225	-8.67 ± 0.03	0.81 ± 0.01	-8.31 ± 0.06	0.19 ± 0.01
230	-8.82 ± 0.03	0.81 ± 0.01	-8.53 ± 0.04	0.19 ± 0.01
235	-8.98 ± 0.03	0.79 ± 0.01	-8.76 ± 0.03	0.21 ± 0.01
240	-9.15 ± 0.03	0.81 ± 0.02	-8.87 ± 0.09	0.19 ± 0.02
245	-9.34 ± 0.03	0.81 ± 0.02	-9.05 ± 0.05	0.19 ± 0.02
250	-9.51 ± 0.01	0.83 ± 0.03	-9.21 ± 0.06	0.17 ± 0.03
255	-9.68 ± 0.01	0.83 ± 0.02	-9.44 ± 0.04	0.17 ± 0.02
260	-9.85 ± 0.01	0.83 ± 0.02	-9.63 ± 0.01	0.17 ± 0.02
265	-10.00 ± 0.03	0.84 ± 0.02	-9.90 ± 0.05	0.16 ± 0.02

[a] Mean values and standard deviations correspond to three separate experiments

Table K.4: The logτ_c values at different temperatures for 0.5% v/v DMSO with TEMPOL, in the absence of EAL.[a]

T **(K)**	**Logτ_c (s)**
200	-7.24 ± 0.02
205	-7.62 ± 0.02
210	-7.90 ± 0.02
215	-8.17 ± 0.02
220	-8.43 ± 0.02
225	-8.63 ± 0.01
230	-8.83 ± 0.01
235	-8.96 ± 0.01
240	-9.12 ± 0.01
245	-9.33 ± 0.00
250	-9.49 ± 0.01
255	-9.66 ± 0.01
260	-9.80 ± 0.00
265	-9.96 ± 0.03

[a] Mean values and standard deviations correspond to three separate experiments

Table K.5: The logτ_c values at different temperatures for 2% v/v DMSO with TEMPOL, in the absence of EAL.[a]

T **(K)**	**Logτ_c (s)**
190	-6.75 ± 0.04
195	-7.26 ± 0.04
200	-7.34 ± 0.06
205	-7.67 ± 0.05
210	-7.96 ± 0.04
215	-8.21 ± 0.03
220	-8.46 ± 0.00
225	-8.69 ± 0.02
230	-8.84 ± 0.01
235	-8.99 ± 0.02
240	-9.10 ± 0.08
245	-9.36 ± 0.02
250	-9.54 ± 0.01
255	-9.70 ± 0.01
260	-9.88 ± 0.00
265	-10.03 ± 0.07

[a] Mean values and standard deviations correspond to three separate experiments

Table K.6: The logτ_c values at different temperatures for 4% v/v DMSO with TEMPOL, in the absence of EAL.[a]

T **(K)**	**Logτ_c (s)**
190	-7.07 ± 0.06
195	-7.36 ± 0.04
200	-7.60 ± 0.02
205	-7.88 ± 0.04
210	-8.07 ± 0.05
215	-8.32 ± 0.03
220	-8.55 ± 0.14
225	-8.72 ± 0.02
230	-8.89 ± 0.07
235	-9.00 ± 0.03
240	-9.19 ± 0.07
245	-9.37 ± 0.02
250	-9.55 ± 0.03
255	-9.74 ± 0.04
260	-9.89 ± 0.03
265	-9.99 ± 0.00

[a] Mean values and standard deviations correspond to three separate experiments

References

[1] N. Shibata, H. Tamagaki, N. Hieda, K. Akita, H. Komori, Y. Shomura, S. Terawaki, K. Mori, N. Yasuoka, Y. Higuchi, and T. Toraya, "Crystal structures of ethanolamine ammonia-lyase complexed with coenzyme b-12 analogs and substrates," *J. Biol. Chem.*, vol. 285, pp. 26484–26493, 2010.

[2] W. D. Robertson, A. M. Bovell, and K. Warncke, "Development of a protein-integrated, cobalt-corrin catalyst for hydrogen production under green conditions," *J. Biol. Inorg. Chem.*, vol. 18, no. 6, pp. 701–713, 2013.

[3] T. Toraya, "Radical catalysis in coenzyme b12-dependent isomerization (eliminating) reactions," *Chem. Rev.*, vol. 103, pp. 2095–2127, 2003.

[4] D. M. Roof and J. R. Roth, "Ethanolamine utilization in salmonella-typhimurium," *J Bacteriol*, vol. 170, no. 9, pp. 3855–3863, 1988.

[5] D. M. Roof and J. R. Roth, "Functions required for vitamin-b12-dependent ethanolamine utilization in salmonella-typhimurium," *J Bacteriol*, vol. 171, no. 6, pp. 3316–3323, 1989.

[6] D. A. Garsin, "Ethanolamine utilization in bacterial pathogens: roles and regulation," *Nat. Rev. Microbiol.*, vol. 8, no. 4, pp. 290–5, 2010.

[7] P. Thiennimitr, S. E. Winter, M. G. Winter, M. N. Xavier, V. Tolstikov, D. L. Huseby, T. Sterzenbach, R. M. Tsolis, J. R. Roth, and A. J. Bäumler, "Intestinal inflammation allows salmonella to use ethanolamine to compete with the microbiota," *Proc. Natl. Acad. Sci.*, vol. 108, no. 42, pp. 17480–17485, 2011.

[8] L. Staib and T. M. Fuchs, "From food to cell: nutrient exploitation strategies of enterpathogens," *MIcrobiology*, vol. 160, pp. 1020–1039, 2014.

[9] L. P. Faust and B. M. Babior, "Overexpression, purification, and some properties of the adocbl dependent ethanolamine ammonia-lyase from salmonella-typhimurium," *Arch. Biochem. Biophys.*, vol. 294, no. 1, pp. 50–54, 1992.

[10] L. R. P. Faust, J. A. Connor, D. M. Roof, J. A. Hoch, and B. M. Babior, "Cloning, sequencing, and expression of the genes encoding the adenosylcobalamin-dependent ethanolamine ammonia-lyase of salmonella-typhimurium," *J. Biol. Chem.*, vol. 265, no. 21, pp. 12462–12466, 1990.

[11] L. Sun and K. Warncke, "Comparative model of eutb from coenzyme b12-dependent ethanolamine ammonia-lyase reveals a b8a8, tim-barrel fold

and radical catalytic site structural features," *Proteins: Structure, Function, and Bioinformatics*, vol. 64, no. 2, pp. 308–319, 2006.

[12] A. Bovell and K. Warncke, "Structure model of salmonella typhimurium ethanolamine ammonia-lyase directs a rational approach to the assembly of the functional [(eutb-eutc)2]3 oligomer from isolated subunits," *Biochemistry*, vol. 52, no. 8, p. 1419–1428, 2013.

[13] R. G. Finke and B. P. Hay, "Thermolysis of adenosylcobalamin - a product, kinetic, and co-c5' bond-dissociation energy study," *Inorg. Chem.*, vol. 23, no. 20, pp. 3041–3043, 1984.

[14] E. N. G. Marsh and D. P. Ballou, "Coupling of cobalt-carbon bond homolysis and hydrogen atom abstraction in adenosylcobalamin-dependent glutamate mutase," *Biochemistry*, vol. 37, pp. 11864–11872, 1998.

[15] R. Padmakumar, R. Padmakumar, and R. Banerjee, "Evidence that cobalt-carbon bond homolysis is coupled to hydrogen atom abstraction from substrate in methylmalonyl-coa mutase," *Biochemistry*, vol. 36, no. 12, pp. 3713–3718, 1997.

[16] A. R. Jones, S. Hay, J. R. Woodward, and N. S. Scrutton, "Magnetic field effect studies indicate reduced geminate recombination of the radical pair in substratebound adenosylcobalamin-dependent ethanolamine ammonia lyase," *J. Am. Chem. Soc.*, vol. 129, pp. 15718–15727, 2007.

[17] B. P. Hay and R. G. Finke, "Thermolysis of the co-c bond of adenosylcobalamin. 2. products, kinetics, and co-c bond dissociation energy in aqueous solution," *J. Am. Chem. Soc.*, vol. 108, pp. 4820–4829, 1986.

[18] B. H. Kaplan and E. R. Stadtman, "Ethanolamine deaminase a cobamide coenzyme-dependent dnzyme .i. purification assay and properties of enzyme," *J. Biol. Chem. Rev.*, no. 243, pp. 1787–1793, 1968.

[19] B. M. Babior, "Mechanism of action of ethanolamine deaminase .i. studies with isotopic hydrogen and oxygen," *J. Biol. Chem.*, vol. 244, pp. 449–456, 1969.

[20] C. Bradbeer, "Clostridial fermentations of choline and ethanolamine .i. preparation and properties of cell-free extracts," *J. Biol. Chem.*, vol. 240, no. 12, pp. 4669–4674, 1965.

[21] C. Bradbeer, "The clostridial fermentations of choline and ethanolamine. 1 preparation and properties of cell-free extracts," *J. Biol. Chem.*, vol. 240, no. 12, p. 4669–74, 1965.

[22] L. Que and W. B. Tolman, "Biologically inspired oxidation catalysis," *Nature*, vol. 455, pp. 333–340, 2008.

[23] J. A. Wells and D. A. Estell, "Subtilisin - an enzyme designed to be engineered," *Trends Biochem. Sci.*, vol. 13, pp. 291–297, 1988.

[24] S. Tanaka, M. R. Sawaya, and T. O. Yeates, "Structure and mechanisms of a protein-based organelle in escherichia coli," *Science*, vol. 327, pp. 81–84, 2010.

[25] T. A. Bobik, B. P. Lehman, and T. O. Yeates, "Baceterial microcompartments: widespread prokaryotic organelles for isolation and optimization of metabolic pathways," *Molec. MIcrobiol.*, vol. 98, pp. 193–207, 2015.

[26] C. L. Randle, P. W. Albro, and J. C. Dittmer, "Phosphoglyceride composition of gram-negative bacteria and changes in composition during growth," *Biochim. Biophys. Acta*, vol. 187, pp. 214–220, 1969.

[27] S. Srikumar and T. M. Fuchs, "Ethanolamine utilization contributes to proliferation of salmonella enterica serovar typhimurium in food and in nematodes," *Appl. Environ. Microbiol.*, vol. 77, no. 1, pp. 281–90, 2011.

[28] S. E. Winter, P. Thiennimitr, M. G. Winter, B. P. Butler, D. L. Huseby, R. W. Crawford, J. M. Russel, C. L. Bevins, L. G. Adams, R. M. Tsolis, J. R. Roth, and A. J. Bäumler, "Inflammation provides a respiratory electron acceptor for salmonella in the gut," *Nature*, vol. 467, pp. 426–429, 2010.

[29] M. M. Kendall, C. C. Gruber, C. T. Parker, and V. Sperandio, "Ethanolamine controls expression of genes encoding components involved in interkingdom signaling and virulence in enterohemorrhagic escherichia coli o157:h7," *mBio*, vol. 3, no. 3, 2012.

[30] P. S. Mead, L. Slutsker, V. Dietz, L. f. McCaig, J. S. Bresee, C. Shapiro, P. M. Griffin, and R. V. Tauxe, "Food-related illness and death in the united states," *Emerg. Infect. Dis.*, vol. 5, pp. 607–625, 1999.

[31] C. R. Braden, "Salmonella enterica serotype enteritidis and eggs: A national epidemic in the united states," *Clin. Infect. Dis.*, vol. 43, pp. 512–517, 2006.

[32] H. Li, D. M. Kristensen, M. K. Coleman, and A. Mushegian, "Detection of biochemical pathways by probabilistic matching of phyletic vectors," *PLoS One*, vol. 4, no. 4, p. e5326, 2009.

[33] C. B. Anfinsen, "Principles that govern the folding of protein chains," *Science*, vol. 181, pp. 223–230, 1973.

[34] J. Y. Pang, X. Li, K. Morokuma, N. S. Scrutton, and M. J. Sutcliffe, "Large-scale domain conformational change is coupled to the activation of the co-c bond in the b-12-dependent enzyme ornithine 4,5-aminomutase: A computational study," *J. Am. Chem. Soc.*, vol. 134, no. 4, pp. 2367–2377, 2012.

[35] A. R. Jones, S. J. O. Hardman, S. Hay, and N. S. Scrutton, "Is there a dynamic protein contribution to the substrate trigger in coenzyme b-12-dependent ethanolamine ammonia lyase?," *Angew. Chem. Int. Edit.*, vol. 50, no. 46, pp. 10843–10846, 2011.

[36] R. G. Silva, A. S. Murkin, and V. L. Schramm, "Femtosecond dynamics coupled to chemical barrier crossing in a born-oppenheimer enzyme," *P. Natl. Acad. Sci.*, vol. 108, pp. 18661–18665, 2011.

[37] G. Bhabha, J. Lee, D. C. Ekiert, J. Gam, I. A. Wilson, H. J. Dyson, S. J. Benkovic, and P. E. Wright, "A dynamic knockout reveals that conformational fluctuations influence the chemical step of enzyme catalysis," *Science*, vol. 332, pp. 234–238, 2011.

[38] H. J. Russel, A. R. Jones, S. Hay, G. M. Greetham, M. Towrie, and N. S. Scrutton, "Protein motions are coupled to the reaction chemistry in coenzyme b12-dependent ethanolamine ammonia-lyase," *Angew. Chem. Intl. Ed.*, vol. 51, pp. 9306–9310, 2012.

[39] H. J. Dyson and P. E. Wright, "Intrinsically unstructured proteins and their functions," *Nat. Rev. Mol. Cell Bio*, vol. 6, pp. 197–208, 2005.

[40] N. Le Breton, M. Martinho, E. Mileo, E. Etienne, G. Gerbaud, B. Guigliarelli, and V. Belle, "Exploring intrinsically disordered proteins using site-directed spin labeling electron paramagnetic resonance spectroscopy.," *Frontiers in Molecular Biosciences*, vol. 2, no. 21, 2015.

[41] F.-X. Gallat, A. Laganowsky, K. Wood, F. Gabel, L. van Eijck, J. Wuttke, M. Moulin, M. Hartlein, D. Eisenberg, J.-P. Colletier, G. Zaccai, and M. Weik, "Dynamic coupling of intrinsically disordered proteins and their hydration water: Comparison with folded soluble and membrane proteins," *Biophys. J.*, vol. 103, pp. 129–136, 2012.

[42] M. C. Thomas, L. Zhanglong, M. E. Jackie, L. P. Natasha, M. Eugene, and E. G. Fanucci, "Continuous wave w- and d-band epr spectroscopy offer

"sweet-spots" for characterizing conformational changes and dynamics in intrinsically disordered proteins," *Biochem Biophys Res Commun*, vol. 450(1), no. 1, p. 723–728, 2012.

[43] B. Vale´rie, R. Sabrina, C. Ste´phanie, L. Elodie, S. Janez, G. Bruno, F. Andre´, and S. Longhi, "Mapping alpha-helical induced folding within the intrinsically disordered c-terminal domain of the measles virus nucleoprotein by site-directed spin-labeling epr spectroscopy," *PROTEINS STRUCTURE FUNCTION AND BIOINFORMATICS*, vol. 00, no. 000, 2008.

[44] H. Frauenfelder, G. Chen, J. Berendzen, P. W. Fenimore, H. Jansson, B. H. McMahon, I. R. Stroe, J. Swenson, and R. D. Young, "A unified model of protein dynamics," *Proc. Natl. Acad. Sci.*, vol. 106, pp. 5129–5134, 2009.

[45] H. Jansson, R. Bergman, and J. Swenson, "Role of solvent for the dynamics and the glass transition of proteins," *J. Phys. Chem. B*, vol. 115, pp. 4099–4109, 2011.

[46] D. Vitkup, D. Ringe, G. A. Petsko, and M. Karplus, "Solvent mobility and the protein 'glass' transition," *Nat. Struct. Biol.*, vol. 7, pp. 34–38, 2000.

[47] S. Ebbinghaus, S. J. Kim, M. Heyden, X. Yu, U. Heugen, M. Gruebele, D. M. Leitner, and M. Havenith, "An extended dynamical hydration shell around proteins," *Proc. Natl. Acad. Sci.*, vol. 104, pp. 20749–20752, 2007.

[48] M. Heyden and J. Tobias, Douglas, "Spatial dependence of protein-water collective hydrogen-bond dynamics," *Phys. Rev. Lett.*, vol. 111, pp. 2181011–2181015, 2013.

[49] V. C. Nibali, G. D'Angelo, A. Paciaroni, J. Tobias, Douglas, and M. Tarek, "On the coupling between the collective dynamics of proteins and their hydration water," *J. Phys. Chem. Lett.*, vol. 5, pp. 1181–1186, 2014.

[50] A. Panagopoulou, A. Kyritsis, R. Sabater i Serra, J. L. Gomez Ribellez, N. Shinyashiki, and P. Pissis, "Glass transition and dynamics in bsa-water mixtures over wide ranges of composition studied by thermal and dielectric techniques," *Biochim. Biophys. Acta*, vol. 1814, pp. 1984–1996, 2011.

[51] M. Nakanishi and A. P. Sokolov, "Protein dynamics in a broad frequency range: Dielectric spectroscopy studies," *J. Non-Cryst. Solids*, vol. 407, pp. 478–485, 2015.

[52] P. W. Fenimore, H. Frauenfelder, B. H. McMahon, and R. D. Young, "Bulk-solvent and hydration-shell fluctuations, similar to alpha- and beta-fluctuations in glasses, control protein motions and functions," *Proceedings of the National Academy of Sciences of the United States of America*, vol. 101, no. 40, pp. 14408–14413, 2004.

[53] F. Franks, "Freeze-drying of bioproducts: putting principles into practice," *Eur. J. Pharm. Biopharm.*, vol. 45, pp. 221–229, 1998.

[54] F. Franks, "Scientific and technological aspects of aqueous glasses," *Biophys. Chem.*, vol. 106, pp. 251–261, 2003.

[55] H. D. Goff, E. Verespej, and D. Jermann, "Glass transitions in frozen sucrose solutions are influenced by solute inclusions within ice crystals," *Thermochim. Acta*, vol. 399, pp. 43–55, 2003.

[56] E. N. G. Marsh, "Coenzyme b12 (cobalamin)-dependent enzymes," *Essays Biochem.*, vol. 34, pp. 139–154, 1999.

[57] J. Gerald F. Combs and P. M. James, *The Vitamins . Fundamentals Aspects in Nutrition and Health*. Elservier Inc., 2017.

[58] T.-I. Tóshiko, G. Enrique, A.-E. Roberto, and E. F. María, "Role of vitamin b12 on methylmalonyl-coa mutase activity," *Biomed and Biotechnol*, vol. 13, no. 6, pp. 423–437, 2012.

[59] K. Yamada, C. Gherasim, R. Banerjee, and M. Koutmos, "Structure of human b12 trafficking protein cbld reveals molecular mimicry and identifies a new subfamily of nitro-fmn reductases," *J. Biol. Chem.*, vol. 290, no. 49, pp. 29155–29166, 2015.

[60] E. N. G. Marsh, "Coenzyme b12 (cobalamin)-dependent enzymes," *Essays in Biochemistry*, vol. 34, 1999.

[61] S. P. Stabler, *B12 and Nutrition*. New York: John Wiley and Sons, 1999.

[62] A. Battersby, "How nature builds the pigments of life: the conquest of vitamin b12.," *Science*, vol. 264, p. 1551–1557, 1994.

[63] R. Banerjee, "The yin-yang of cobalamin biochemistry.," *Chem. Biol.*, vol. 4, p. 175–186, 1997.

[64] S. W. Graves, J. S. Krouwer, and B. M. Babior, "Deamination of 2-aminopropanol by ethanolamine ammonia-lyase, an adocbl-requiring enzyme. kinetics and isotope effects for the r and s enantiomers of the substrate," *J. Biol. Chem.*, vol. 255, pp. 7444–7448, 1980.

[65] P. W. Jones and J. M. Turner, "Interrelationships between the enzymes of ethanolamine metabolism in escherichia-coli," *J. Gen. Microbiol.*, vol. 130, pp. 299–308, 1984.

[66] I. Stojiljkovic, A. J. Baumler, and F. Heffron, "Ethanolamine utilization in salmonella typhimurium: nucleotide sequence, protein expression, and mutational analysis of the ccha cchb eute eutj eutg euth gene cluster," *J. Bacteriol.*, vol. 177, no. 5, pp. 1357–1366, 1995.

[67] D. Bucher, G. M. Sandala, B. Durbeej, L. Radom, and D. M. Smith, "The elusive 5 ′-deoxyadenosyl radical in coenzyme-b-12-mediated reactions," *J. Am. Chem. Soc. Rev.*, vol. 134, pp. 1591–1599, 2012.

[68] J. M. Canfield and K. Warncke, "Geometry of reactant centers in the co-ii substrate radical pair state of coenzyme b-12-dependent

ethanolamine deaminase determined by using orientation-selection-eseem spectroscopy," *J. Phys. Chem. B*, vol. 106, pp. 8831–8841, 2002.

[69] J. Pilbrow, *EPR of B12-Dependent Enzyme Reactions and Related Systems*, pp. 431–462. New York: Wiley, 1982.

[70] B. M. Babior, T. H. Moss, W. H. Orme-Johnson, and H. Beinert, "Mechanism of action of ethanolamine ammonia-lyase, a b12-dependent enzyme - participation of paramagnetic species in catalytic deamination of 2-aminopropanol," *J. Biol. Chem.*, vol. 249, no. 14, pp. 4537–4544, 1974.

[71] J. Retey, C. J. Suckling, D. Arigoni, and B. M. Babior, "Stereochemistry of reaction catalyzed by ethanolamine ammonia-lyase, an adenosylcobalamin-dependent enzyme - example of racemization accompanying substitution," *J. Biol. Chem.*, vol. 249, pp. 6359–6360, 1974.

[72] T. O. Yeates, M. C. Thompson, and T. A. Bobik, "The protein shells of bacterial microcompartment organelles," *Curr. Op. Struct. Biol.*, vol. 21, pp. 223–231, 2011.

[73] T. O. Yeates, "Bacterial microcompartment organelles: Protein shell structure and evoluation," *Annu. Rev. Biophys*, vol. 39, pp. 185–205, 2010.

[74] T. O. Yeates, "Self-assembly in the carboxysome: a virial capside-like protein shell in bacterial cells," *Biochem. Soc. Trans.*, vol. 35 part 3, 2007.

[75] S. J. Tsai and T. O. Yeates, "Bacterial microcompartments: Insights into the structure, mechanism, and engineering applications," *Prog. Mol. Biol. Transl. Sci.*, vol. 103, pp. 1–20, 2011.

[76] M. Sutter, "Two new high-resolution crystals structures of carboxysome pentamer proteins reveal high structural conservation of the ccml orthologs among distantly related cyanobacterial species," *Photosynth Res*, vol. 118, pp. 9–16, 2013.

[77] J. K. Lassila, "Assembly of robust bacterial microcompartment shells using building blocks from an organelle of unknown function," *J. Mol. Biol*, vol. 426, pp. 2217–2228, 2014.

[78] J. N. Kinney, A. Salmeen, F. Cai, and C. A. Kerfield, "Elucidating essential role of conserved carboxysome protein ccmn reveals common feature of bacterial microcompartment assembly," *J. Biol. Chem.*, vol. 287, pp. 17729–17736, 2012.

[79] C. A. Kerfeld and O. Erbilgin., "Bacterial microcompartments and the modular construction of microbial metabolism.," *Trends Microbiol*, vol. xx, pp. 1–13, 2014.

[80] S. D. Axen, "A taxonomy of bacterial microcompartment loci construction by a novel scoring method," *PLOS computational Biology*, vol. 10, no. 10. E1003898, 2014.

[81] F. Cai, "Engineering bacterial microcompartments shells: Chimeric shell proteins and chimeric carboxysome shells," *ACS Synth Biol*, vol. xxxxxx, 2013.

[82] A. Pang, "Protein structure and folding: Structural insights into higher order assembly and functions of the bacterial microcompartment protein pdua," *J. Biol. Chem*, vol. 389, pp. 22377–22384, 2014.

[83] J. Jorda, "Using comparative genomics to uncover new kinds of proteins-based metabolic organelles in bacteria," *Protein Science*, vol. 22, pp. 179–195, 2013.

[84] N. M. Wheatley, "Bacterial microcompartment shells of diverse functional types possess pentameric vertex proteins," *Protein Science*, vol. 22, pp. 660–665, 2013.

[85] S. Frank, A. D. Lawrence, M. B. Prentice, and M. J. Warren, "Bacterial microcompartments moving into a synthetic biological world," *J. Biotechnol.*, vol. 163, pp. 273–279, 2013.

[86] O. T. Yeates, C. S. Crowley, and S. Tanaka, "Bacterial microcompartment organelles: Protein shell structure and evolution," *Annu. Rev. Biophys.*, vol. 39, p. 185–205, 2010.

[87] M. Held, "Eut bcaterial microcompartments: Insights into their functon, structure and bioengineering applications," *J Mol Microbiol Biotechnol*, vol. 23, pp. 308–320, 2013.

[88] E. Kofoid, C. Rappleye, I. Stojiljkovic, and J. Roth, "The 17-gene ethanolamine (eut) operon of salmonella typhimurium encodes five homologues of carboxysome shell proteins," *J. Bacteriol.*, vol. 181, no. 17, pp. 5317–29, 1999.

[89] S. Tanaka, "Structure and mechanisms of a protein-based organelle in escherichia coli," *Science*, vol. 327, no. 81, 2010.

[90] J. E. Wertz and J. R. Bolton, *Electron Spin Resonance*. New York: Chapman and Hall, 1986.

[91] E. Zavoisky, "Spin-magnetic resonance in paramagnetics.," *Fizicheskiĭ Zhurnal*, vol. 9, p. 211–245, 1945.

[92] M. Kohne, C. Zhu, and K. Warncke, "Two dynamical regimes of the substrate radical rearrangement reaction in b12-dependent ethanolamine ammonia-lyase resolve contributions of native protein configurations and collective configurational fluctuations to catalysis," *Biochemistry*, vol. 56, pp. 3257–3264, 2017.

[93] C. Zhu and K. Warncke, "Reaction of the co-ii-substrate radical pair catalytic intermediate in coenzyme b-12-dependent ethanolamine ammonia-lyase in frozen aqueous solution from 190 to 217 k," *Biophys. J.*, vol. 95, pp. 5890–5900, 2008.

[94] M. Wang and K. Warncke, "Kinetic and thermodynamic characterization of coii-substrate radical pair formation in coenzyme b12-dependent

ethanolamine ammonia-lyase in a cryosolvent system by using time-resolved, full-spectrum continuous-wave electron paramagnetic resonance spectroscopy," *J. Am. Chem. Soc.*, vol. 130, pp. 4846–4858, 2008.

[95] C. Zhu and K. Warncke, "Kinetic isolation and characterization of the radical rearrangement step in coenzyme b12-dependent ethanolamine ammonia-lyase," *J. Am. Chem. Soc.*, vol. 132, pp. 9610–9615, 2010.

[96] M. Wang, C. Zhu, M. Kohne, and K. Warncke, "Resolution and characterization of chemical steps in enzyme catalytic sequences by using low-temperature and time-resolved, full-spectrum epr spectroscopy in fluid cryosolvent and frozen solution systems," *Meth. Enzymol.*, vol. 563, Part A, pp. 59–94, 2015.

[97] G. I. Likhtenshtein, *Spin Labeling Methods in Molecular Biology*. New York: John Wiley and Sons, Inc., 1976.

[98] Z. Yang, Y. Liu, P. Borbat, J. Zweier, J. Freed, and W. Hubbell, "Pulsed esr dipolar spectroscopy for distance measurements in immobilized spin labeled proteins in liquid solution," *J. Am. Chem. Soc.*, no. 134, p. 9950–9952, 2012.

[99] A. P. Todd, J. Cong, F. Levinthal, C. Levinthal, and W. L. Hubbell, "Site-directed mutagenesis of colicin e1 provides specific attachment sites for spin labels whose spectra are sensitive to local conformation," *Proteins*, vol. 6, pp. 294–305, 1989.

[100] Y. Polyhach, E. Bordignon, and G. Jeschke, "Rotamer libraries of spin labelled cysteines for protein studies," *Physical Chemistry Chemical Physics*, vol. 13, pp. 2356–2366, 2011.

[101] N. LeBreton, MarlèneMartinho, ElisabettaMileo, EmilienEtienne, G. Gerbaud, BrunoGuigliarelli, and a. ValérieBelle, "Exploring intrinsically disordered proteins using site-directed spin labeling electron paramagnetic resonance spectroscopy," *Frontiers in Molecular Biosciences*, vol. 2, no. 21, 2015.

[102] D. B. Michael, H. Kálmán, and L. H. Wayne, "Resolving conformational and rotameric exchange in spin-labeled proteins using saturation recovery epr," *Appl Magn Reson*, vol. 37(1-4), no. 363, 2010.

[103] C. S. Klug and J. B. Feix, "Methods and applications of site-directed spin labeling epr spectroscopy," *Methods Cell Biol.*, vol. 84, pp. 617–658, 2008.

[104] G. Jeschke, "Conformational dynamics and distribution of nitroxide spin labels," *Prog. Nucl. Magn. Reson. Spectrosc.*, vol. 72, p. 42–60, 2013.

[105] N. V. Ivanisenko and S. A. Dzuba, "Molecular motion in frozen phospholipid bilayers in the presence of sucrose and sorbitol studied by the spin-echo epr of spin labels," *Appl. Magn. Reson.*, vol. 44, pp. 883–891, 2013.

[106] C. Altenbach, C. J. Lopez, K. Hideg, and W. L. Hubbell, "Exploring structure, dynamics, and topology of nitroxide spin-labeled proteins using continuous wave electron paramagnetic resonance spectroscopy," *Meth. Enzymol.*, vol. 564, pp. 59–100, 2015.

[107] P. Kaur, Y. Li, J. Cai, and L. Song, "Selective membrane disruption mechanism of an antibacterial g-aapeptide defined by epr spectroscopy," *Biophys. J.*, vol. 110, no. 1793, pp. 1789–1799, 2016.

[108] S. N. Bhat, A. Sharma, and S. V. Bhat, "Vitrification and glass transition of water: Insights from spin probe esr," *Phys. Rev. Lett.*, vol. 95, pp. 2357021–2357024, 2005.

[109] D. Banerjee, S. N. Bhat, S. V. Bhat, and D. Leporini, "Esr evidence for 2 coexisting liquid phases in deeply supercooled bulk water," *Proc. Natl. Acad. Sci.*, vol. 106, pp. 11448–11453, 2009.

[110] D. Banerjee and S. V. Bhat, "Vitrification, relaxation and free volume in glycerol-water binary liquid mixture: Spin probe esr studies," *J. Non-Cryst. Solids*, vol. 355, pp. 2433–2438, 2009.

[111] W. Hubbell, C. López, C. Altenbach, and Z. Yang, "Technological advances in site-directed spin labeling of proteins," *Curr. Opin. Struct. Biol.*, no. 23, p. 725–733, 2013.

[112] R. Guzzi, R. Bartucci, and D. Marsh, "Heterogeneity of protein substates visualized by spin-label epr," *Biophys. J.*, vol. 106, p. 716–722, 2014.

[113] J. F. Alistair, G. C. Maria, H. Graham, and A. H. Michael, "New developments in spin labels for pulsed dipolar epr," *Molecules*, no. 19, pp. 16998–17025, 2014.

[114] A. P. Mackenzie, W. Derbyshire, and D. S. Reid, "Nonequilibrium freezing behavior of aqueous systems," *Philos. T. Trans. Roy. Soc. B*, vol. 278, pp. 167–189, 1977.

[115] H. Chen, L. Sun, and K. Warncke, "Heterogeneous ordered-disordered structure of the mesodomain in frozen sucrose-water solutions revealed by multiple electron paramagnetic resonance spectroscopies," *Langmuir*, vol. 29, pp. 4357–4365, 2013.

[116] P. Douzou, *Cryobiochemistry: An Introduction*. New York: Academic Press, 1977.

[117] D. H. Rasmussen and A. P. Mackenzie, "Phase diagram for the system water-dimethylsulphoxide," *Nature*, vol. 220, pp. 1315–1317, 1968.

[118] S. S. N. Murthy, "Phase behavior of the supercooled aqueous solutions of dimethyl sulfoxide, ethylene glycol, and methanol as seen by dielectric spectroscopy," *J. Phys. Chem. B*, vol. 101, pp. 6043–6049, 1997.

[119] M. Wang and K. Warncke, "Entropic origin of cobalt-carbon bond cleavage catalysis in adenosylcobalamin-dependent ethanolamine ammonia-lyase," *J. Am. Chem. Soc.*, vol. 135, pp. 15077–15084, 2013.

[120] L. P. Faust and B. M. Babior, "Overexpression, purification, and some properties of the adocbl-dependent ethanolamine ammonia-lyase from salmonella typhimurium," *Arch. Biochem. Biophys*, vol. 294, no. 1, pp. 50–54, 1992.

[121] S. Stoll and A. Schweiger, "Easyspin, a comprehensive software package for spectral simulation and analysis in epr," *J. Magn. Reson.*, vol. 178, pp. 42–55, 2006.

[122] R. T. Ross, "Dipolar broadening of epr spectra due to solute aggregation in frozen aqueous solution," *J. Chem. Phys.*, vol. 42, pp. 3919–3922, 1965.

[123] J. S. Leigh and G. H. Reed, "Electron paramagnetic resonance studies in frozen aqueous solutions. elimination of freezing artifacts.," *J. Phys. Chem.*, vol. 75, pp. 1202–1204, 1971.

[124] J. W. Bye, L. Platts, and R. J. Falconer, "Biopharmaceutical liquid formulation: a review of the science of protein stability and solubility in aqueous environments," *Biotechnol. Lett.*, vol. 36, pp. 869–875, 2014.

[125] Y. Miao, Z. Yi, D. C. Glass, L. Hong, M. Tyagi, J. Baudry, N. Jain, and J. C. Smith, "Temperature-dependent dynamical transitions of different classes of amino acid residue in a globular protein," *J. Am. Chem. Soc.*, vol. 134, pp. 19576–19579, 2012.

[126] J. R. Lewandowski, M. E. Halse, M. Blackledge, and L. Emsley, "Direct observation of hierarchical protein dynamics," *Science*, vol. 348, pp. 578–581, 2015.

[127] G. Ahmad, M. Gromiha, H. Fawareh, and A. Sarai, "Asa view: Database and tool for solvent accessibility representation in proteins," *BMC Bioinformatics*, vol. 5, pp. 1–5, 2004.

[128] C. R. Cantor and P. R. Schimmel, *Biophysical Chemistry*, vol. 2. San Francisco: W. H. Freeman and Company, 1980.

[129] C. A. Angell, "Formation of glasses from liquids and biopolymers," *Science*, vol. 267, pp. 1924–1935, 1995.

[130] D. Wolfgang, "The protein-solvent glass transition," *Biochim. Biophys. Acta*, vol. 1804, pp. 3–14, 2010.

[131] Y. Qin, L. Wang, and D. Zhong, "Dynamics and mechanism of ultrafast water–protein interactions," *Proc Natl Acad Sci*, vol. 113, no. 30, p. 8424–8429, 2016.

[132] Y.-H. Kuo and Y.-W. Chiang, "Slow dynamics around a protein and its coupling to solvent," *ACS Cent. Sci.*, vol. 4, pp. 645–655, 2018.

[133] B. Nforneh and K. Warncke, "Mesodomain and protein-associated solvent phases with temperature-tunable (200–265 k) dynamics surround ethanolamine ammonia-lyase in globally polycrystalline aqueous solution containing dimethyl sulfoxide," *J. Phys. Chem. B*, vol. 121, pp. 11109–11118, 2017.

[134] P. Rittigstein, R. D. Priestley, L. J. Broadbelt, and J. M. Torkelson, "Model polymer nanocomposites provide an understanding of confinement effects in real nanocomposites," *Nature Materials*, vol. 6, p. 278–282, 2007.

[135] G. Schiro, A. Cupane, E. Vitrano, and F. Bruni, "Dielectric relaxations in confined hydrated myoglobin," *J. Phys. Chem. B*, vol. 113, pp. 9606–9613, 2009.

[136] R. R. Baglay and C. B. Roth, "Local glass transition temperature tg(z) of polystyrene next to different polymers: Hard vs. soft confinement," *J. Chem. Phys.*, vol. 146, p. 203307, 2017.

[137] T. Arakawa, Y. Kita, and S. N. Timasheff, "Protein precipitation and denaturation by dimethyl sulfoxide," *Biophy. Chem.*, vol. 131, pp. 62–70, 2007.

[138] S. N. Timasheff, "Protein-solvent preferential interactions, protein hydration, and the modulation of biochemical reactions by solvent components," *Proc. Natl. Acad. Sci.*, vol. 99, pp. 9721–9726, 2002.

[139] F. H. Stillinger, "A topographic view of supercooled liquids and glass formation," *Science*, vol. 267, pp. 1935–1939, 1995.

[140] S. Khodadadi and A. P. Sokolov, "Atomistic details of protein dynamics and the role of hydration water," *Biochimica et Biophysica Acta*, vol. 1861, p. 3546–3552, 2017.

[141] E. G. Strekalvoa, J. Luo, E. H. Stanley, G. Franzese, and S. V. Buldyrev, "Confinement of anomalous liquids in nanoporous matrices," *Phys. Rev. Lett.*, vol. 109, p. 105701, 2012.

[142] D. Ringe and G. A. Petsko, "The 'glass transition' in protein dynamics: what it is, why it occurs, and how to exploit it," *Biophysical Chemistry*, vol. 105, no. 2-3, pp. 667–680, 2003.

[143] S. Khodadadi, S. Pawles, J. H. Roh, V. G. Sakai, E. Mamontov, and A. P. Sokolov, "The origin of the dynamic transition in proteins," *J. Chem. Phys.*, vol. 128, p. 195106, 2008.

[144] B. Nforneh, A. M. Bovell, and K. Warncke, "Electron spin-labelling of the eutc subunit in b12-dependent ethanolamine ammonia-lyase reveals dynamics and a two-state conformational equilibrium in the n-terminal, signal-sequence-associated domain," *Free Radical Research*, vol. 52, no. 3, pp. 307–318, 2018.

[145] E. Bordignon and H.-J. Steinhoff, *Membrane Protein Structure and Dynamics Studied by Site-Directed Spin-Labeling ESR. In ESR Spectroscopy in Membrane Biophysics; Biological Magnetic Resonance*, vol. 27. New York, NY, USA: Springer, 2007.

[146] H. S. Mchaourab, M. A. Lietzow, K. Hideg, and W. L. Hubbel, "Motion of spin-labeled side chains in t4 lysozyme. correlation with protein structure and dynamics," *Biochemistry*, vol. 35, pp. 7692–7704, 1996.

[147] W. Kabsch and C. Sander, "Dictionary of protein secondary structure: pattern recognition of hydrogen-bonded and geometrical features," *Biopolymers*, vol. 22, pp. 2577–2637, 1983.

[148] C. Fan, S. Cheng, Y. Liu, C. M. Escobar, C. S. Crowley, R. E. Jefferson, T. O. Yeates, and T. A. Bobik, "Short n-terminal sequences package proteins into bacterial microcompartments," *Proc. Natl. Acad. Sci.*, vol. 107, pp. 7509–7514, 2010.

[149] S. Choudhary, M. Quin, M. Sanders, E. T. Johnson, and C. Schmidt-Dannert, "Engineered protein nano-compartments for targeted enzyme localization," *PLoS ONE*, vol. 7, p. e33342, 2012.

[150] K. L. Morrison and G. A. Weiss, "Combinatorial alanine-scanning," *Curr. Opin. Chem. Biol.*, vol. 5, pp. 302–307, 2001.

[151] O. Carugo, "Predicting residue solvent accessibility from protein sequence by considering the sequence environment," *Protein Eng.*, vol. 13, pp. 607–609, 2000.

[152] H. Chen and H.-X. Zhou, "Prediction of solvent accessibility and sites of deleterious mutations from protein sequence," *Nucleic Acids Res.*, vol. 33, pp. 3193–3199, 2005.

[153] H. Zhang, T. Zhang, K. Chen, S. Shen, J. Ruan, and L. Kurgan, "On the relation between residue flexibility and local solvent accessibility in proteins," *Proteins*, vol. 76, pp. 617–636, 2009.

[154] W. Wu, Z. Wang, P. Cong, and T. Li, "Accurate prediction of protein relative solvent accessibility using a balanced model," *BioData Min.*, vol. 10, p. 1, 2017.

[155] K. Akita, N. Hieda, N. Baba, S. Kawaguchi, H. Sakamoto, Y. Nakanishi, M. Yamanishi, K. Mori, and T. Toraya, "Purification and some properties of wild-type and n-terminal-truncated ethanolamine ammonia-lyase of escherichia coli," *J Biochem*, vol. 147, pp. 83–93, 2010.

[156] K. Guraprasad, B. V. B. Reddy, and M. W. Pandit, "Correlation between stability of a protein and its dipeptide composition - a novel approach for predicting in vivo stability of a protein from its primary sequence," *Protein Eng.*, vol. 4, pp. 155–161, 1990.

[157] M. M. Hatmal, Y. Li, B. G. Hegde, P. B. Hegde, C. C. Jao, R. Langen, and I. S. Haworth, "Computer modeling of nitroxide spin labels on proteins," *Biopolymers*, vol. 97, pp. 35–44, 2012.

[158] G. Hagelueken, R. Ward, J. H. Naismith, and O. Schiemann, "Mtsslwizzard: In silico spin-labelling and generation of distance distributions in pymol," *Appl. Magn. Reson.*, vol. 42, pp. 377–391, 2012.

[159] A. Cornish-Bowden, *Fundamentals of Enzyme Kinetics*. Boston: Butterworths and Company, Ltd, 1981.

[160] Y. H. Roos and N. Potes, "Quantification of protein hydration, glass transitions, and structural relaxations of aqueous protein and carbohydrate-protein systems," *J. Phys. Chem. B*, vol. 119, p. 7077-7086, 2015.

[161] S. Cerveny, I. Combarro-Palacios, and J. Swenson, "Evidence of coupling between the motions of water and peptides," *J. Phys. Chem. Lett.*, vol. 7, p. 4093-4098, 2016.

[162] K. Sasaki, A. Panagopoulou, R. Kita, N. Shinyashiki, S. Yagihara, A. Kyritsis, and P. Pissis, "Dynamics of uncrystallized water, ice, and hydrated protein in partially crystallized gelatin-qater mixtures studied by broadband dielectric spectroscopy," *J. Phys. Chem. B*, vol. 121, p. 265-272, 2017.

[163] N. Yamamoto, S. Ito, M. Nakanishi, E. Chatani, K. Inoue, H. Kandori, and K. Tominaga, "Effect of emperature and hydration level on purple membrane dynamics studied using broadband dielectric spectroscopy from subghz to thz regions," *J. Phys. Chem. B*, vol. 122, p. 1367-1377, 2018.

[164] M. Gupta, C. Chakravarty, and S. Bandyopadhyay, "Sensitivity of protein glass transition to the choice of water model," *J. Chem. Theory Comput.*, vol. 12, p. 5643-5655, 2016.

[165] Q. Yangzhong, W. Lijuan, and Z. Dongping, "Dynamics and mechanism of ultrafast water–protein interactions," *Proc Natl Acad Sci*, vol. 113, no. 30, p. 8424–8429, 2016.

[166] B. Biman, "Untangling complexdynamics of biological water at protein–water interface," *Proc Natl Acad Sci*, vol. 113, no. 30, p. 8355–8357, 2016.

[167] N. Ucuncuoglou and K. Warncke, "Radical capture and rearrangement-enabling functions of the substrate radical macrostate are enacted by

two sequential protein configurational microstates in b12-dependent ethanolamine ammonia-lyase," *Biophys. J. (submitted)*, 2017.